POC ALGORITHMS BASED ON SPECTRAL REMOTE SENSING DATA AND ITS TEMPORAL AND SPATIAL VARIABILITY IN THE GULF OF MEXICO

A Dissertation

by

YOUNG BAEK SON

Submitted to the Office of Graduate Studies of
Texas A&M University
in partial fulfillment of the requirements for the degree of

DOCTOR OF PHILOSOPHY

May 2006

Major Subject: Oceanography

POC ALGORITHMS BASED ON SPECTRAL REMOTE SENSING DATA AND ITS TEMPORAL AND SPATIAL VARIABILITY IN THE GULF OF MEXICO

A Dissertation

by

YOUNG BAEK SON

Submitted to the Office of Graduate Studies of
Texas A&M University
in partial fulfillment of the requirements for the degree of

DOCTOR OF PHILOSOPHY

Approved by:

Chair of Committee,	Wilford D. Gardner
Committee Member,	Mary Jo Richardson
	Oleksiy V. Mishonov
	Anthony M. Filippi
Head of Department,	Wilford D. Gardner

May 2006

Major Subject: Oceanography

ABSTRACT

POC Algorithms Based on Spectral Remote Sensing Data and Its Temporal and Spatial Variability in the Gulf of Mexico. (May 2006)

Young Baek Son, B.S.; M.S., Pusan National University, Korea

Chair of Advisory Committee: Dr. Wilford D. Gardner

This dissertation consists of three studies dealing with particulate organic carbon (POC). The first study describes the temporal and spatial variability of particulate matter (PM) and POC, and physical processes that affect the distribution of PM and POC with synchronous remote sensing data. The purpose of the second study is to develop POC algorithms in the Gulf of Mexico based on satellite data using numerical methods and to compare POC estimates with spectral radiance. The purpose of the third study is to investigate climatological variations from the temporal and spatial POC estimates based on SeaWiFS spectral radiance and physical processes, and to determine the physical mechanisms that affect the distribution of POC in the Gulf of Mexico.

For the first and second studies, hydrographic data from the Northeastern Gulf of Mexico (NEGOM) study were collected on each of 9 cruises from November 1997 to August 2000 across 11 lines. Remotely sensed data sets were obtained from NASA and NOAA using algorithms that have been developed for interpretation of ocean color data from various satellite sensors. For the third study, we use the time-series of POC estimates, sea surface temperature (SST), sea surface height anomaly (SSHA), sea

surface wind (SSW), and precipitation rate (PR) that might cause climatological variability and physical processes.

The distribution of surface PM and POC concentrations were affected by one or more factors such as river discharge, wind stress, stratification, and the Loop Current/Eddies. To estimate POC concentration, empirical and model-based approaches were used using regression and principal component analysis (PCA) methods. We tested simulated data for reasonable and suitable algorithms in Case 1 and Case 2 waters.

Monthly mean values of POC concentrations calculated with PCA algorithms. The spatial and temporal variations of POC and physical forcing data were analyzed with the empirical orthogonal function (EOF) method. The results showed variations in the Gulf of Mexico on both annual and inter-annual time scales.

DEDICATION

To my parents and parents-in-law

my wife, Yoon Hyang Kang and two sons, Seok Han and Shang Hwan

ACKNOWLEDGEMENTS

Without the help and assistance of innumerable people, this thesis would not be finished. First of all I would like to give my special thanks to my advisor, Dr. Wilford D. Gardner, for providing scientific insight and knowledge, for how to treat students respectfully, and for financially supporting me for a fairly long time. I appreciate Dr. Mary Jo Richardson for providing abundant knowledge about particle dynamics. I want to express thanks to Dr. Alexey V. Mishonov for advising on ocean-color analysis in doing this study. I am grateful to Dr. Anthony M. Filippi for helping me understand remote sensing study and its application. I appreciate Dr. Tom Whitworth for his valuable questions before my defense.

I appreciate my friends in PNU and O&M alumni for their help in many ways. Some of them provided delicious dinners to my family.

Most importantly, not to be forgotten, are my parents and parents-in-law for their support from my home country Korea. Their deepest love has been instrumental in my study here in the U.S.A. My gratitude is warmest, however, to my wife Yoon Hyang Kang, who followed me without complaint and always encouraged me throughout my study even when neglected for long times. Special thanks also should be given to my lovely babies Seok Han and Shang Hwan.

TABLE OF CONTENTS

Page

CHAPTER Page

LIST OF TABLES

LIST OF FIGURES

FIGURE Page

FIGURE Page

FIGURE Page

FIGURE Page

FIGURE Page

CHAPTER I

INTRODUCTION

The ocean color signal can be affected by scattering and absorption of visible and infrared light by water, as well as by the inorganic, organic, particulate, and dissolved material derived from lithogenic and biogenic particles (IOCCG, 2000; Robinson, 2004). Although algorithms using remote sensing signals reflected from these particulates may under- or over-estimate their concentrations, ocean color data can provide useful information about global/regional conditions at the surface of the ocean. In addition, new ocean color sensors and improved algorithms can provide high-resolution images to obtain a better understanding of conditions in surface waters.

Most variability of optical signals in surface waters of the open ocean results from changes in biogenic particle concentrations, but coastal areas have the added complexity of input of organic/inorganic material from resuspended bottom sediment or light reflectance from the seafloor in optically shallow areas. Therefore, waters based on optical properties are generally classified into two categories. One is the open ocean designated as "Case 1" waters (Morel's seawater classification, Morel and Prieur, 1977; Gordon and Morel, 1983) which are very easily defined with standard algorithms from satellite data. The other is coastal regions designated as "Case 2" waters (Morel's seawater classification, Morel and Prieur, 1977; Gordon and Morel, 1983) which are more complex than Case 1 waters in composition and optical properties. In Case 1

This dissertation follows the style of Deep-Sea Research II.

waters, phytoplankton are the major agent causing variation in optical properties of surface water. Case 2 waters are influenced not only by phytoplankton and related particles, but also by other substances, that may vary independently of phytoplankton, notably lithogenic particles in suspension and colored dissolved organic matter (CDOM).

There are empirical correlations and model-based approaches that can be used to study the marine environment and its temporal and spatial variability using ocean color data and *in situ* measurements. Empirical algorithms are useful to study regional/global or seasonal effects because these approaches are simple and easy to derive even from a limited number of measurements (O'Reilly et al., 1998; Shen et al., 2001). Algebraic methods and non-linear optimization techniques in the model-based algorithms require bio-optical model input (Bukata et al., 1981; Roesler and Perry, 1995; Lee et al., 1996, 1999, 2002; Garver and Siegel, 1997; Carder et al., 1999; Hoge et al., 1999; Maritorena et al., 2002; Roesler and Boss, 2003). Principal component analysis (PCA) and neural network (NN) approaches are used in bio-optical models or representative sets of bio-optical and *in situ* measurements (Mueller, 1976; Gower et al., 1984; Fischer, 1985; Fischer et al., 1986; Sathyendranath et al., 1989, 1994; Atkinson and Tatnall, 1997; Keiner and Yan, 1998; Keiner and Brown, 1999; Krawczyk et al., 1999; Schiller and Doerffer, 1999; Gross et al., 2000; IOCCG, 2000; Kishino et al., 2000; Tanaka et al., 2000).

Satellite data sets using these approaches have provided estimates of spectral light attenuation of water, concentrations of chlorophyll, pigment compositions, suspended sediments, CDOM, physical dynamics, and time series of these data. Many

researchers have focused on studying the concentration of chlorophyll pigment and light attenuation to predict primary production in ocean waters (Sathyendranath et al., 1989, 1994; Gower et al., 1999; IOCCG, 1999; Behrenfeld and Boss, 2003; Behrenfeld et al., 2005). They also have used ocean color products to differentiate among bloom types, including harmful algal blooms (Shen et al., 2001; Hu, 2002). Other studies have investigated temporal and spatial variability of concentrations of suspended sediment or yellow matter (Sathyendranath et al., 1989; Doerffer and Fischer, 1994). Moreover, physical processes, including ocean circulation, river plumes, current meanders, and eddies, influence the distribution of chlorophyll, CDOM and suspended sediment (Vastano et al., 1995; Walker, 1996; Strub and James, 2000; Thomas et al., 2003; Ohlmann and Niiler, 2005).

In order to identify important climatological variability and physical forcing functions in a system, empirical orthogonal function (EOF) analysis has often been used in satellite imagery. Most EOF studies using satellite data try to find signals of seasonal / inter - annual variations and significant relationships among multi-value data sets, such as sea surface temperature (SST) and Chlorophyll, SST and wind data, SST and in situ data, and altimeter/tide gauge/SST/ocean color. These relationships are used to explain physical dynamics based on the signal strength of EOF parameters tested (Kantha and Clayson, 2000; Strub and James, 2000; Thomas et al., 2003; Son, 2005). Temporal and spatial variations are an index of changes of the oceanic environment.

The above cited studies of satellite algorithms and applications focused on parameters, such as chlorophyll, CDOM, and suspended matter, but they had little

information about estimates of particulate organic carbon (POC) based on ocean color data. Although recent studies have started to address POC estimates (Stramski et al., 1999; Loisel et al., 2001; Mishonov et al., 2003; Gardner et al., in press), these approaches using simple empirical methods have not been used to understand POC variability in the non-linear Case II environments.

For this study, various approaches have been used to determine relationships between *in situ* measurements and satellite data and to make good use of this information to understand temporal and spatial variability in the marine environment. Shipboard measurements, such as chlorophyll/pigment concentration, particulate/dissolved organic matter (POM/DOM), particulate matter (PM), temperature, salinity, current, and inherent optical properties (IOP), are frequently collected from ships. From satellites, we can obtain data such as normalized water leaving radiance (Lwn)/remote-sensing reflectance (R_{rs}), diffuse attenuation coefficient, sea surface temperature (SST), sea surface wind (SSW), sea surface height anomaly (SSHA), and precipitation rate (PR). For this study, *in situ* data were collected during the Northeastern Gulf of Mexico (NEGOM) study, sponsored by the Mineral Management Service of the U. S. Department of the Interior, between November 1997 and August 2000. The remotely sensed data are generated and provided by NASA and NOAA using various satellite sensors. These combined data sets provide an excellent opportunity to sea-truth optical signals to improve our understanding of the marine environment in a wide variety of optical provinces.

The purpose of this study is to investigate the relationships between shipboard data and spectral remote sensing data (the visible, near-infrared, thermal-infrared, and microwave wavelength); to develop efficient and suitable POC algorithms to study the global/regional marine environment based on remote sensing data using numerical methods; to relate changes in optical data to different oceanographic forcing functions; to investigate the climatological variability using ocean color data; and eventually to predict the optical properties under given physical conditions.

1.1. Study Area

The Gulf of Mexico is a semi-enclosed basin with passages at the Yucatan Channel and the Florida Straits. The Gulf of Mexico has a broad continental shelf and narrow continental slope, and its maximum water depth is about 3,600 m (Fig. 1.1).

The Northeastern Gulf of Mexico area is located between the Louisiana shelf and Florida straits. This area consists of a broad continental shelf and a narrow continental slope and rise. Several river systems on the surrounding land provide a large mass of fresh water to the shelf along with suspended sediments, organic and inorganic matter, and pollutants.

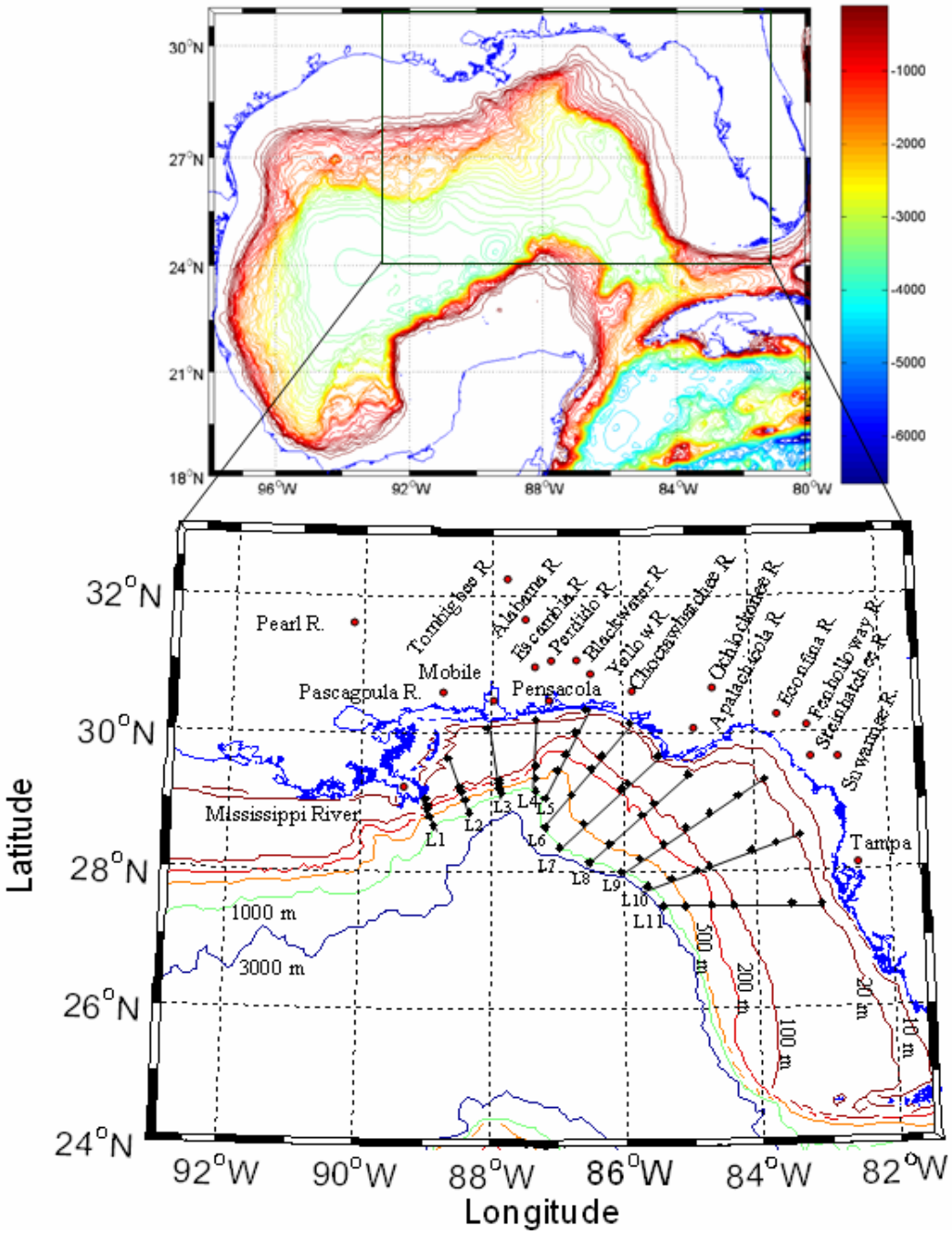

Fig. 1.1. Bathymetry in the Gulf of Mexico and Northeastern Gulf of Mexico (NEGOM) sampling station from November 1997 to August 2000 (11 sampling tracks and 60 sampling stations).

The largest riverine source is the Mississippi-Atchafalaya System (Walker et al., 1994), which drains approximately 40% of the continental United States. Due to the input of organic and inorganic materials, the Mississippi River plume has been identified as a potentially important factor in the high level of primary production found in the northern Gulf of Mexico, and strongly influences seasonal and inter-annual circulation patterns (Lohrenz et al., 1990; Redalje et al., 1994; Rabalais et al., 1996; Walker, 1996). Tidal currents on the Louisiana shelf are weak and regional circulation is predominantly wind-driven (Molinari and Mayer, 1982; Kennicutt et al., 1995; DiMarco and Reid, 1998).

The continental shelf in the northwestern Gulf of Mexico has a broad, nearly uniform bathymetry, and is 200 kilometer in width between Louisiana (92°W) and the Texas-Louisiana border (94°W). The bathymetry generally remains parallel to the shoreline two hundred meters from shore to the shelf.

The Florida platform is a broad and gently sloping region formed by a sequence of deep-water carbonates. The general circulation along the Florida coast is complex because of the combination of tides, winds, and river buoyancy forcing.

A particularly interesting feature of the northeast Gulf seafloor is DeSoto Canyon. It is located close to where the generally north-south trend of the Florida platform joins with the east-west trend of the Mississippi-Alabama shelf. The canyon is curved, almost S-shaped, and has a small downslope gradient.

In the mesoscale circulation system, the Loop Current (LC) or Loop Current Eddies (LCE) significantly affects the circulation of the Gulf of Mexico (Hofmann and

Worley, 1986; Smith, 1986; Schroeder et al., 1987; Hamilton et al., 1999, 2002; Sturges and Leben, 2000; Frolov et al., 2004; Romanou and Chassignet, 2004). As the precursor of the Gulf Stream, the Loop Current enters the Gulf through the Yucatan Channel and flows in a generally clockwise direction before leaving through the Florida Straits. The loop current generates warm core eddies that move to the western Gulf of Mexico and often spin up anti-cyclonic cold core eddies. The frontal area between these eddies can cause an entrainment of coastal waters and transport off the shelf (Merrell and Morrison, 1981; Brooks and Legeckis, 1982). The Loop Current along the west Florida coast exerts alternating strong and weak influences on this circulation system (Molinari and Mayer, 1982).

1.2. Data

1.2.1. Shipboard Data

During the Northeastern Gulf of Mexico project (NEGOM), data from approximately 100 CTD/transmissometer/fluorometer casts were collected on each of nine cruises from November 1997 to August 2000 along the same eleven track lines. Each seasonal cruise was completed along lines normal to the coastline between mid-Florida and the Mississippi River, starting from about 20m water depth on the shelf and moving out to the 1000m isobath. This area spans a wide range of particle concentrations and types, from turbid river runoff to clear and open-ocean waters. Full hydrographic data, including beam attenuation (c_p), were collected at each station. Water samples were filtered to obtain concentrations of PM and POC at about half of the stations.

1.2.2. River Discharge Data for the NEGOM Region

Historical river discharge rates were obtained for the larger rivers between the Mississippi River (Louisiana) and the Suwannee River (central Florida) from USGS (http://waterdata.usgs.gov/nwis/sw) and U.S. Army Corps of Engineers (http://www.mvn.usace.army.mil/eng/edhd/Wcontrol/miss.htm). Long-term means of monthly discharge from September 1997 to December 2004 were compared with discharge rates for each cruise. River discharge regions were classified into six areas, and the values were summed with each river discharge rate: 1) Mississippi River; 2) Mississippi area including the Pearl and Pascagoula River; 3) Alabama Area including Tombigbee and Alabama River; 4) West Florida Area including Escambia, Perdido, Blackwater, and Yellow River; 5) Middle Florida Area including Choctawhatchee, Ochlockonee, and Apalachicola River; 6) East Florida Area including Econfina, Fenholloway, Steinhatchee, and Suwannee River (Fig. 1.1).

1.2.3. Remotely Sensed Data

1) Sea Viewing Wide Field of View Sensor (SeaWiFS) Imagery

The daily, weekly and monthly SeaWiFS satellite images (levels 1 and 3) covering the Gulf of Mexico were obtained from the NASA Goddard Space Flight Center DAAC (http://daac.gsfc.nasa.gov/data/dataset/index.html). SeaWiFS sensor uses the 8 wavelengths. Six bands are visible wavelengths and others near-infrared wavelengths. Each wavelength has the primary application (Table 1.1). Level 1 data were remapped to a standard projection using the SeaDAS program (1 km spatial

resolution). Level 3 data (9 km resolution) were used for the monthly images. All imagery data were reviewed manually, and those with obvious errors in atmospheric correction and cloud flagging (typically these were cloudy images with less than 10 % cloud-free ocean) were deemed invalid (Thomas et al., 2003). All available scenes within the study region were processed into monthly images from September 1997 to December 2004 and used to form a time series.

Table 1.1. Spectral characteristics of SeaWiFS sensor.

Band	Center Wavelength (nm)	Color	Primary Use
1	412	Violet	Dissolved organic matter (include Gelbstoffe)
2	443	Blue	Chlorophyll absorption
3	490	Blue-green	Pigment absorption (Case II), K_{490}
4	510	Blue-green	Chlorophyll absorption
5	555	Green	Pigments, optical properties, sediments
6	670	Red	Atmospheric correction
7	765	Near-IR	Atmospheric correction, aerosol radiance
8	865	Near-IR	Atmospheric correction, aerosol radiance

2) Sea Surface Temperature (SST) Imagery

The daily, weekly and monthly SST composite images (September 1997 to December 2004) from the NOAA Advanced Very High Resolution Radiometer (AVHRR) were obtained from http://podaac.jpl.nasa.gov/index.html. These level 3 data consisted of the standard map projection (4 and 9 km), and they were remapped to the same projection as the SeaWiFS data (9 km resolution) and archived.

3) Sea Surface Height Anomaly (SSHA) Imagery

SSHA data were obtained from grid values and calculated by a combination of TOPEX/POSEIDON and Jason-1 altimeters. The TOPEX/POSEIDON altimeter operates at two frequencies (Ku(13.6 GHz) and C(5.3 GHz) bands). Jason-1 is only a single altimeter (dual-frequency instrument) (Robinson, 2004). A standard correction was applied to the altimeter data set, and they were reconfigured to a regular grid of 9 km resolution like the SeaWiFS data. Partial compensation for the loss of the sea height associated with the mean field height is removed. With a repeated mission every 10-days, SSHA data were collected from September 1997 to December 2004 for the same region (10 day composite, along track, http://podaac.jpl.nasa.gov/index.html).

4) Sea Surface Wind (SSW) Stress and Precipitation Rate (PR) Imagery

SSW and Precipitation Rate data were obtained from the QuikScat and Special Sensor Microwave/Imager (SSM/I). The SSM/I sensor operates at 4 frequency bands (19.35, 22.235, 37.0, and 85.5 GHz). QuikScat is used for the Ku band scatterometer (Robinson, 2004). QuikScat data are available from July 1999 to present (daily, 0.25 degree resolution, http://podaac.jpl.nasa.gov/index.html) and SSM/I data are available from 1987 to the present (daily/weekly/monthly, 0.25 degree resolutions, http://www.remss.com/).

CHAPTER II

DETERMINING SPATIAL AND TEMPORAL VARIATIONS OF PARTICULATE ORGANIC CARBON USING *IN SITU* MEASUREMENTS AND SATELLITE DATA IN THE NORTHEASTERN GULF OF MEXICO

2.1. Introduction

Particulate materials in the ocean are derived from lithogenic and biogenic sources, including river discharges, living phytoplankton and bacteria, atmospheric deposition, and detrital remains of organisms (Depetris, 1996; Prospero, 1996). Lithogenic particles come mainly from land. Some biogenic particles are transported by rivers, but most are created in the oceans through biological processes. These particles move from the ocean's surface to the deep sea and into surface sediments.

Particulate materials have organic as well as inorganic sources and contain living biological organisms resulting in a complex biogeochemical cycle that produces and recycles the biomass. In the open ocean, most particles are biological organisms and associated detritus. In coastal regions, terrestrial inorganic materials transported by rivers and organic matter decayed from land plant can be dominant.

The Gulf of Mexico, a semi-enclosed ocean, is biologically productive in the shelf environments and has a physically complex circulation system (Vastano et al., 1995; Walker, 1996; Ohlmann and Niiler, 2005). High levels of inorganic/organic materials are supplied by the inputs of freshwater, sediment, nutrients, and pollutants (Walker et al., 1994; Oey, 1995; Morey et al., 2003). Those materials are distributed by

the wind and circulation systems and transported from continental shelves into ocean basins. They also have a different spatial and temporal variability influenced by the seasonal and inter-annual variations. These conditions can sometimes cause negative impacts resulting from high particle concentrations and productivity, such as a large "dead zone" of hypoxia along the Gulf Coast. The NEGOM, Louisiana-Texas Shelf Physical Oceanography Program (LATEX), and hypoxia studies have provided useful information for characterizing the oceanic environment of the northern Gulf of Mexico region (Cho et al., 1998; DiMarco and Reid, 1998; Son, 2005). However, these studies do not cover the whole Gulf of Mexico and have the spatial and temporal limitation of *in situ* measurements.

Remote sensing data can provide valuable information on the temporal and spatial variability of particulate materials as well as on the circulation processes affecting the fate of material in the surface ocean (Vastano et al., 1995; Strub and James, 2000; Thomas et al., 2003; Behrenfeld et al., 2005; Ohlmann and Niiler, 2005; Gardner et al., in press). Ocean color sensors can detect water quality parameters from scattering and absorption of visible and infrared wavelengths, such as chlorophyll, CDOM, and suspended matter. Other sensors using the infrared or microwave bands can successfully determine physical factors, such as sea surface temperature, sea surface wind, sea surface height, and finally rainfall. These types of data yield synoptic coverage over regional/global scales, independent of research ship or mooring observations.

Consequently, the purpose of this study is to investigate the temporal and spatial variability of particulate materials, especially POC and PM, and to determine the physical forcing factors that significantly affect the distribution of particulate materials with matching satellite data. Satellite remote sensing and NEGOM data were used to detect changes in the particle status.

2.2. Results and Discussions

2.2.1. Seasonal Pattern of PM and POC

The purpose of the NEGOM study was to investigate the spatial and temporal distribution of hydrographic variables and to define physical processes in the shelf and slope of the northern Gulf of Mexico. During each of nine cruises, 60 stations were sampled along l1 cross-shelf transects between November 1997 and August 2000.

In this study, higher PM and POC concentrations were observed during the summer seasons and lower values during the fall seasons (Figs. 2.1 and 2.2). The variations of surface POC concentrations roughly corresponded with those of surface PM and seasonally varied in a similar fashion, though the variations were slightly greater for PM than for POC (Table 2.1).

During the fall seasons (1997 (N1), 1998 (N4), and 1999 (N7)), higher PM and POC concentrations were generally confined to the inner shelf. These concentrations decreased across the outer shelf and the upper slope. Surface particle distributions and concentrations, however, had similar patterns, but their maxima were different (Figs. 2.1 and 2.2).

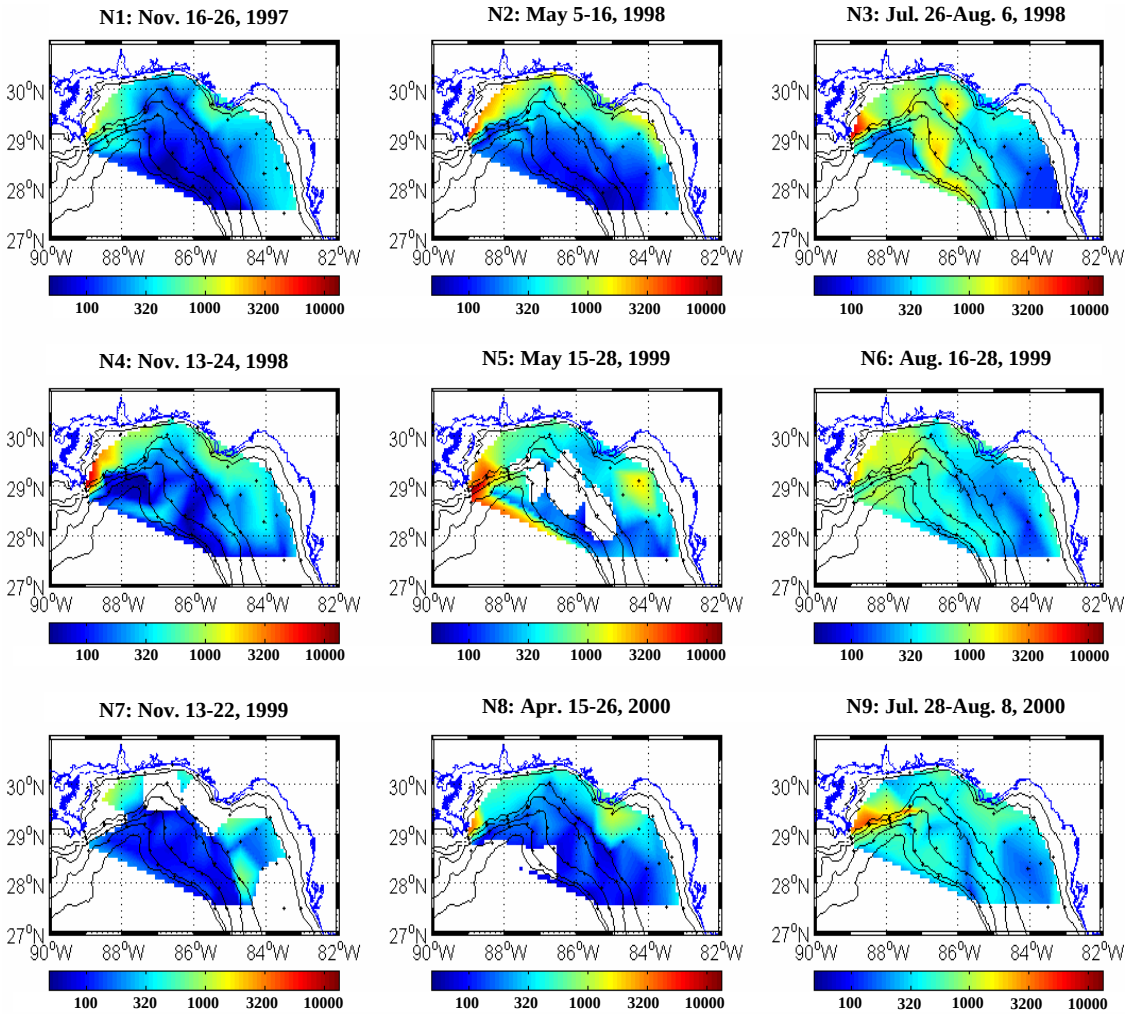

Fig. 2.1. Surface particulate matter concentration (mg/m^3) from bottle data averaged during each NEGOM hydrographic cruise.

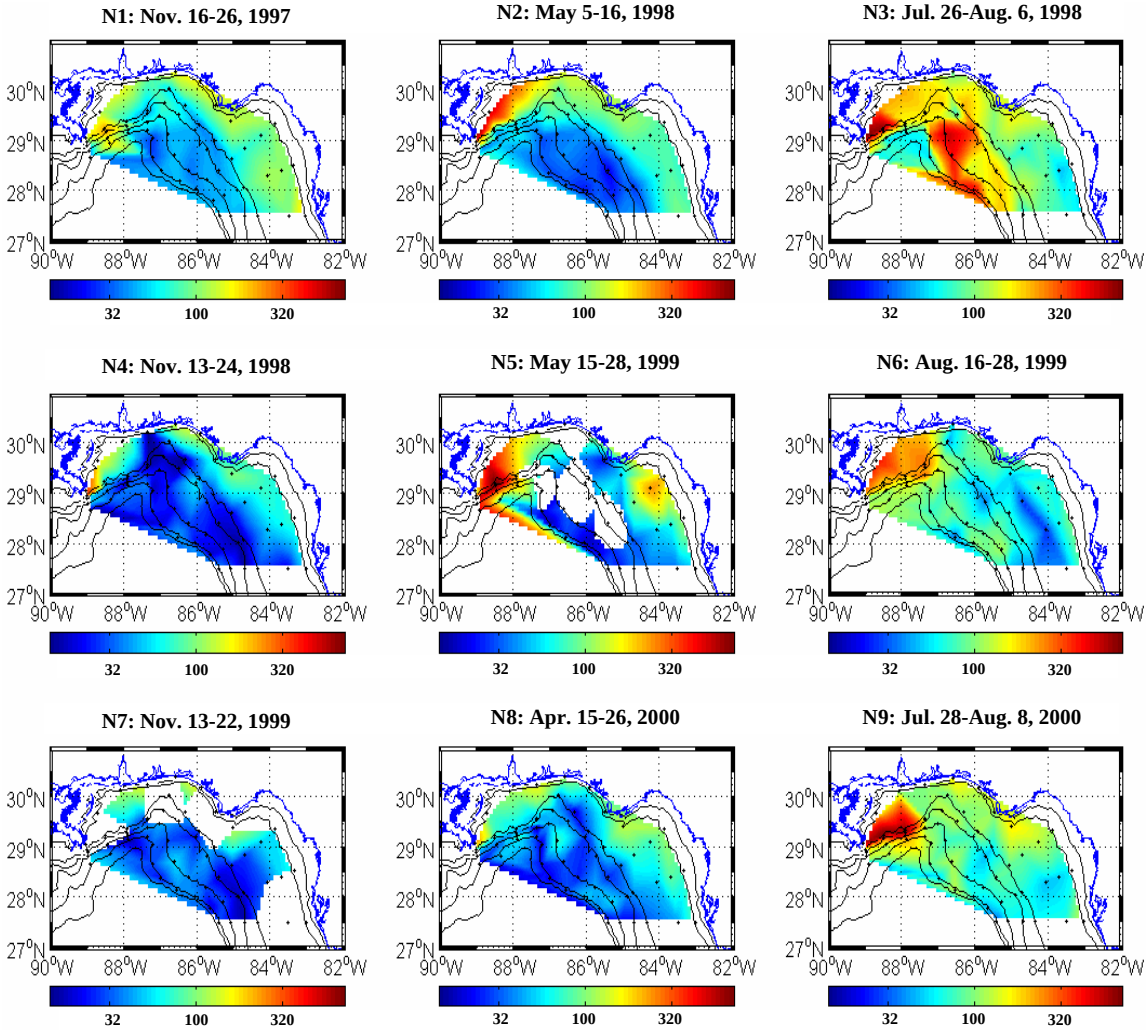

Fig. 2.2. Surface particulate organic carbon concentration (mg/m^3) from bottle data averaged during each NEGOM hydrographic cruise.

Table 2.1. The PM, POC, salinity, and temperature variations of *in situ* measurement during each NEGOM hydrographic cruise.

		N1	N2	N3	N4	N5	N6	N7	N8	N9
PM (mg/m^3)	Mean	284	482	787	607	1082	568	269	323	689
	Max.	2411	6420	9200	10367	15462	2612	2219	4627	5648
	Min.	40	56	87	42	59	99	45	56	99
POC (mg/m^3)	Mean	80	87	178	52	129	111	46	56	139
	Max.	235	667	730	403	771	415	161	252	752
	Min.	26	21	47	13	15	26	15	12	30
CTD Surface Salinity (psu)	Mean	35.3	33.8	31.8	35.2	33.3	31.8	35.7	35.9	33.5
	Max.	36.1	36.4	35.8	36.3	36.4	36.4	36.6	36.5	36.8
	Min.	30.5	23.0	24.4	22.6	18.0	26.3	31.6	31.2	27.5
CTD Surface Temperature (°C)	Mean	22.0	24.2	30.2	24.4	25.5	30.6	23.7	22.5	30.0
	Max.	23.9	25.6	32.0	26.1	28.2	31.4	25.8	24.8	31.8
	Min.	17.6	20.2	28.3	20.2	22.7	29.3	20.7	20.9	28.8

During the fall seasons, lower temperature and salinity values were found on the inner shelf and near major river areas. Surface temperature and salinity were inversely correlated with PM and POC concentrations (Figs. 2.3 and 2.4). In fall of 1997 (N1), fresh water input in all major rivers was greater than during other fall seasons (N4 and N7, Figs. 2.5 and 2.6) excepted the Mississippi River (Fig. 2.5a). Relatively lower temperature and salinity values found near the Mississippi Delta (Figs. 2.3 and 2.4). The water column was strongly stratified with cooler and saltier water compared with other fall seasons (Fig. 2.7).

SST from NOAA satellite data showed that cold water intruded the warm water along the inner shelf during the fall of 1997 (Fig. 2.8). The northern Gulf shelf and slope experienced anticyclonic and cyclonic flows driven by the Loop Current and Eddies during the each sampling period, but location and strength changed between cruises and showed no seasonal trends (Fig. 2.9). Winds, which affect local shore currents, varied with time and space during the fall seasons. During cruises N1 and N4, winds blew west-northwest and were stronger in the western shelf than in the eastern shelf. During cruise N7, winds changed to the southwest (Fig. 2.10).

During the spring seasons (1998 (N2), 1999 (N5), and 2000 (N8)), most of the higher concentrations of POC and PM occurred between Mobile Bay and the Mississippi delta, the area into which higher river inputs of the Mississippi, Pearl, and Tombigbee (Alabama) Rivers (Fig. 1.1). Other areas of high PM and POC concentration were offshore of the Apalachicola and Suwannee rivers in Florida (Figs. 2.1 and 2.2).

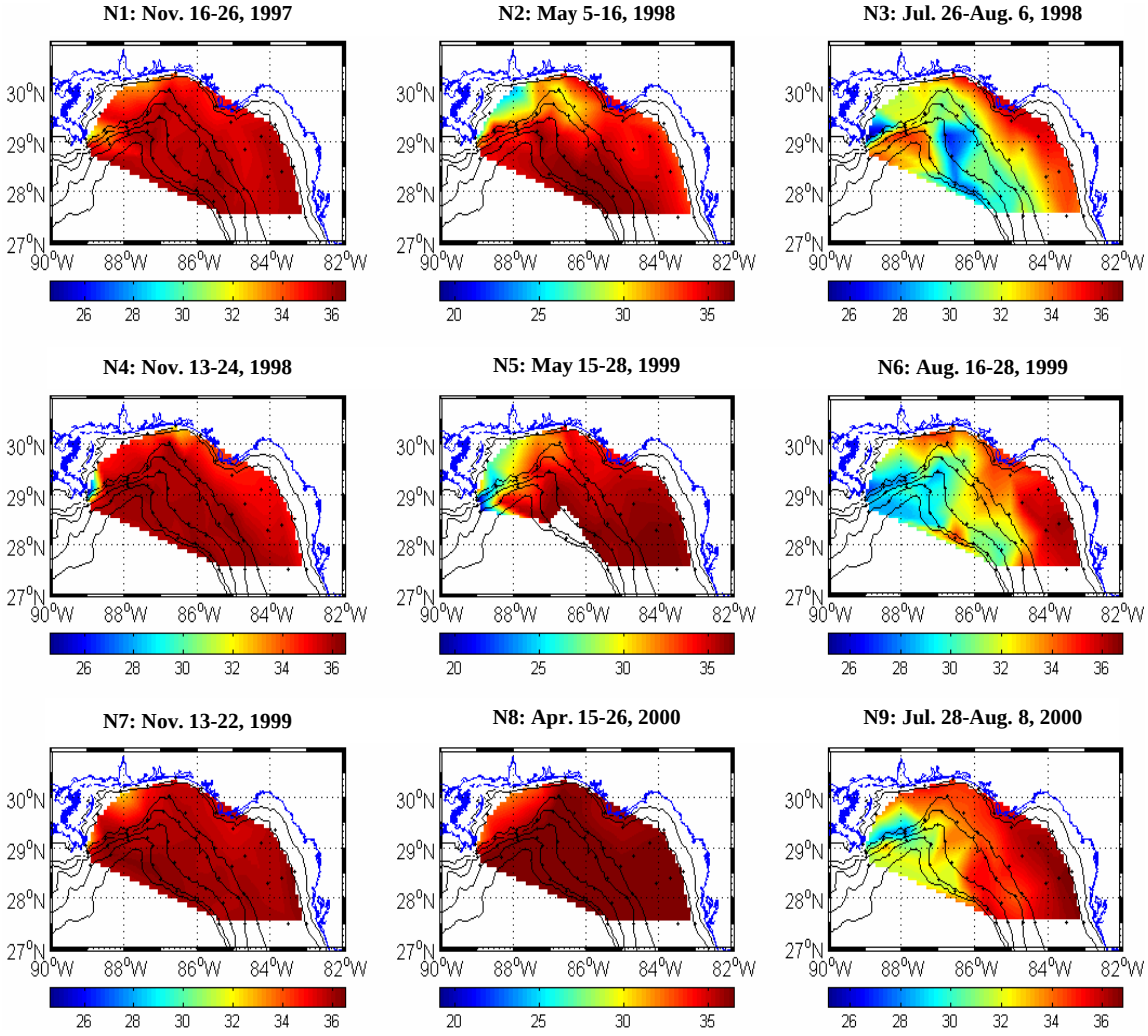

Fig. 2.3. Surface salinity (psu) from CTD data averaged during each NEGOM hydrographic cruise.

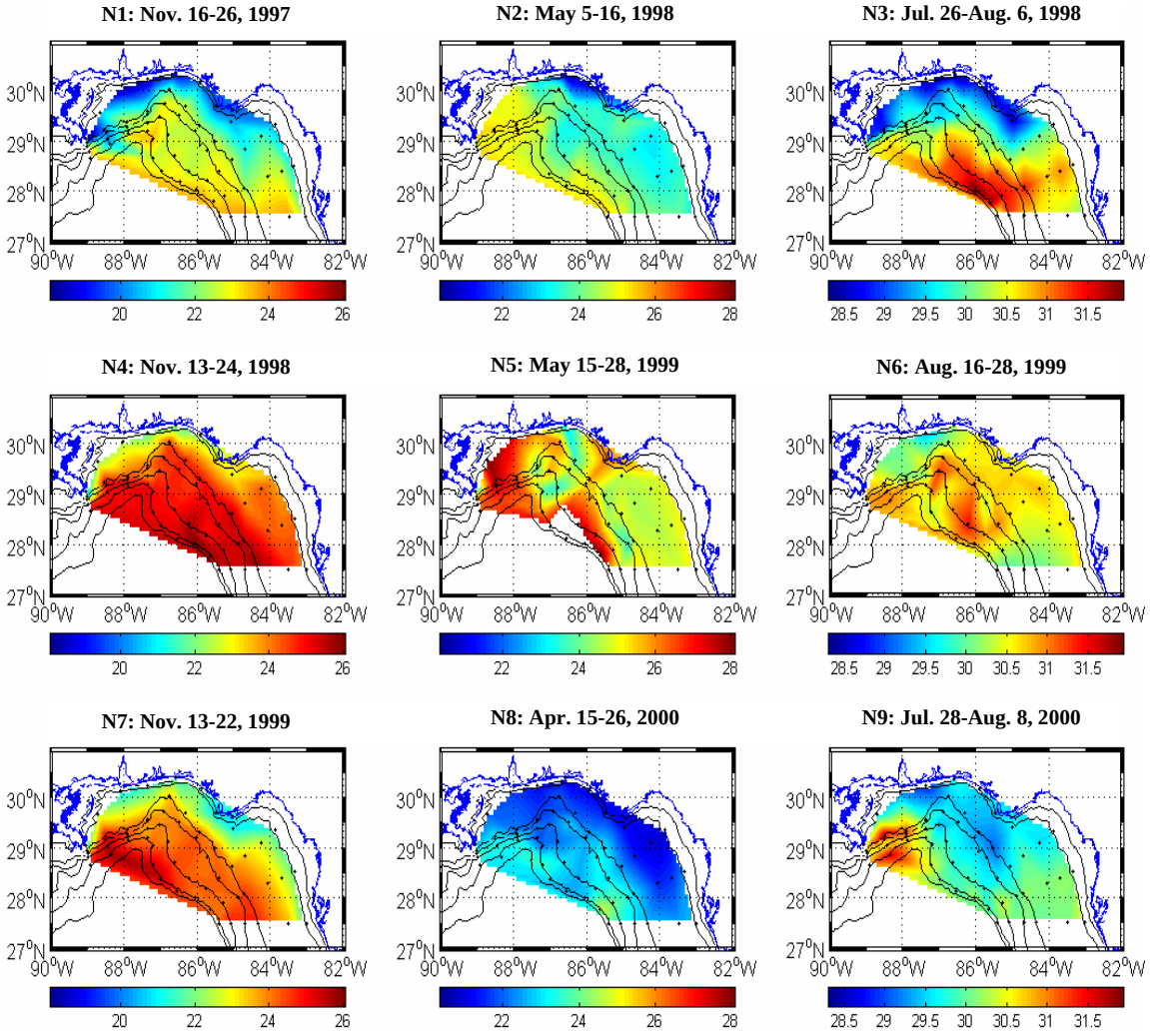

Fig. 2.4. Surface potential temperature (°C) from CTD data averaged during each NEGOM hydrographic cruise.

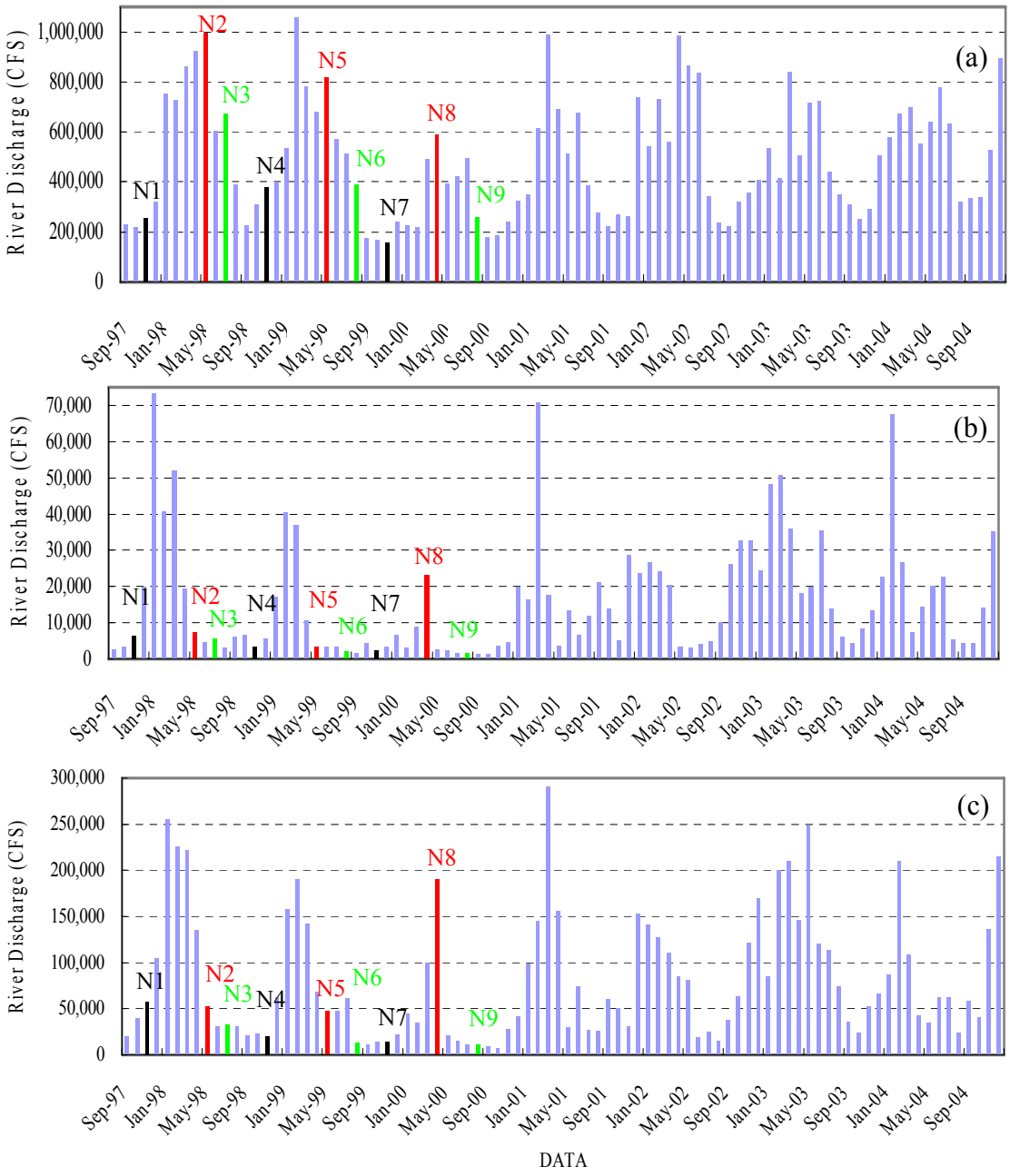

Fig. 2.5. Monthly discharge for major rivers in the northern Gulf of Mexico (fall is black, spring is red, and summer is green) for (a) the Mississippi River; (b) the Mississippi Area; (c) the Alabama Area; (d) the west Florida; (e) the middle Florida; (f) the east Florida.

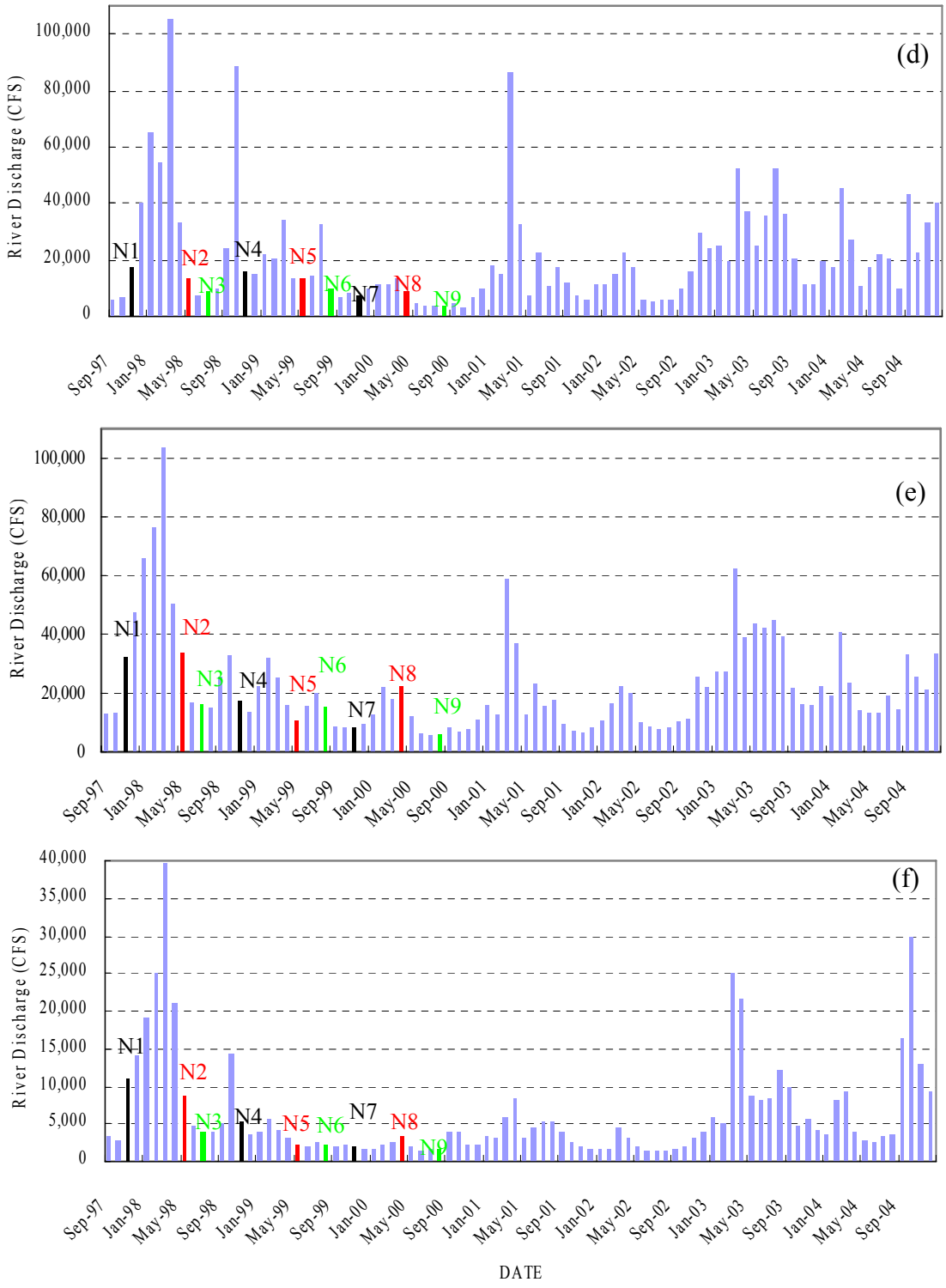

Fig. 2.5. (continued)

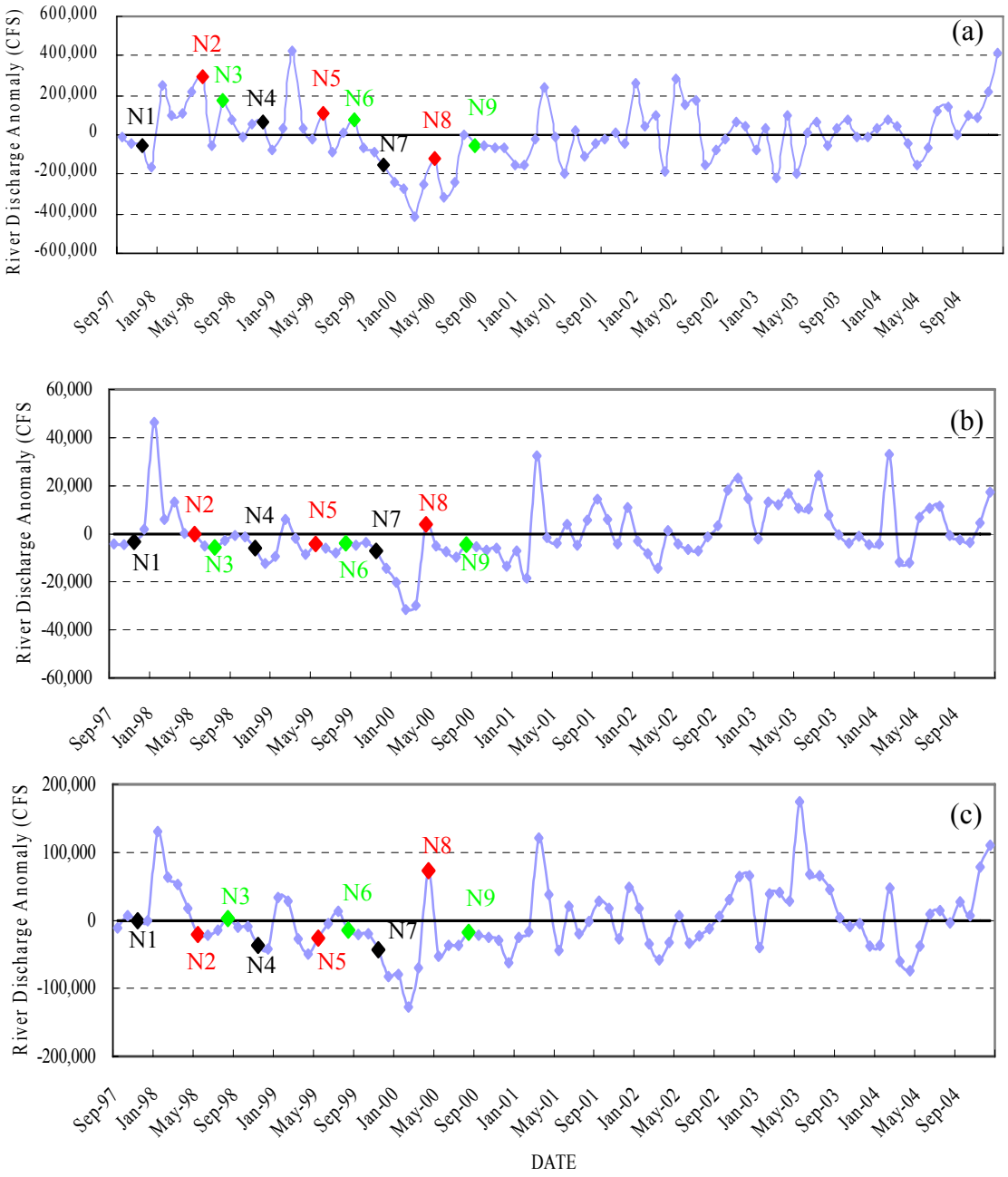

Fig. 2.6. Anomalies of monthly discharge for major rivers in the northern Gulf of Mexico (fall is black, spring is red, and summer is green) for (a) the Mississippi River; (b) the Mississippi Area; (c) the Alabama Area; (d) the west Florida; (e) the middle Florida; (f) the east Florida.

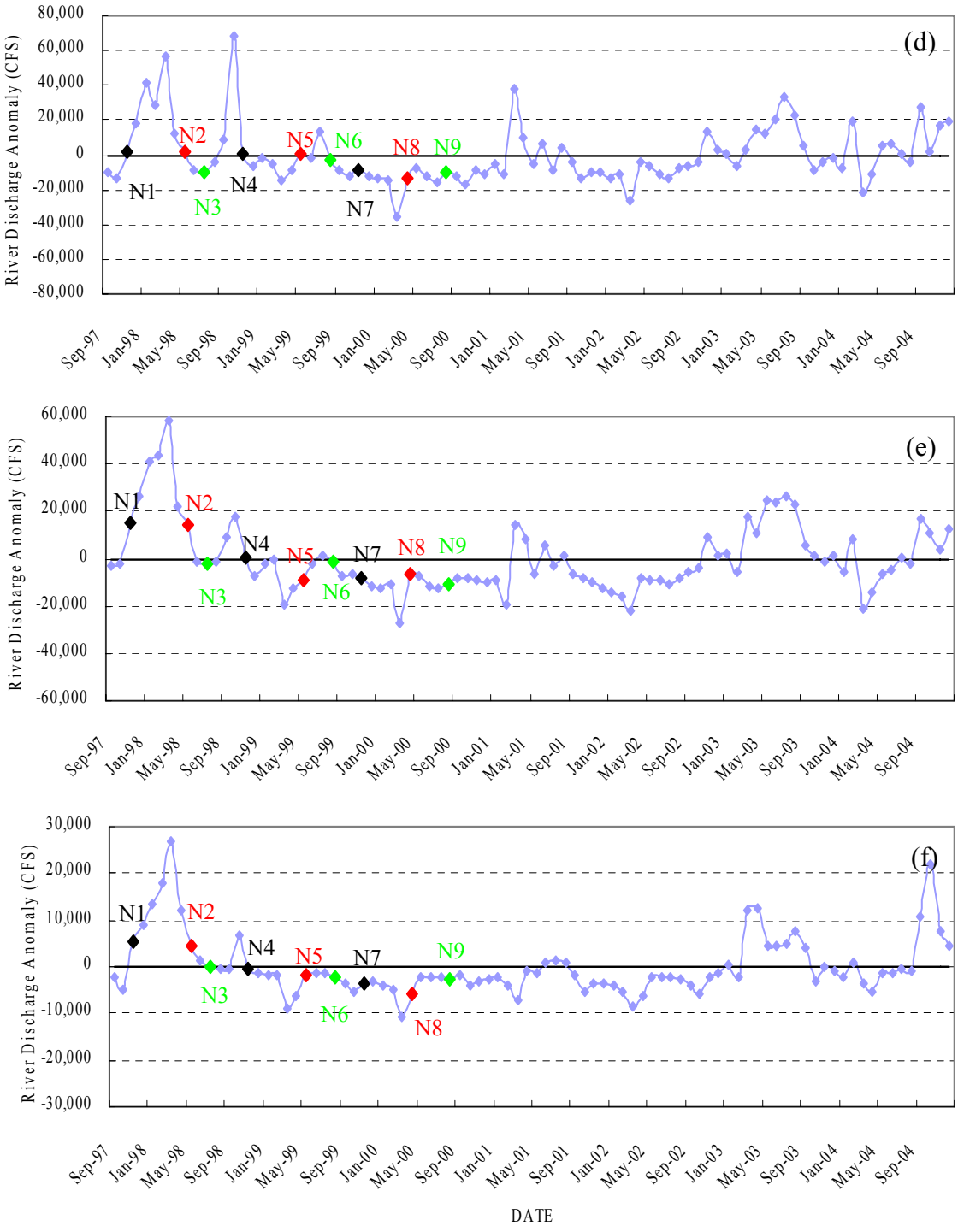

Fig. 2.6. (continued)

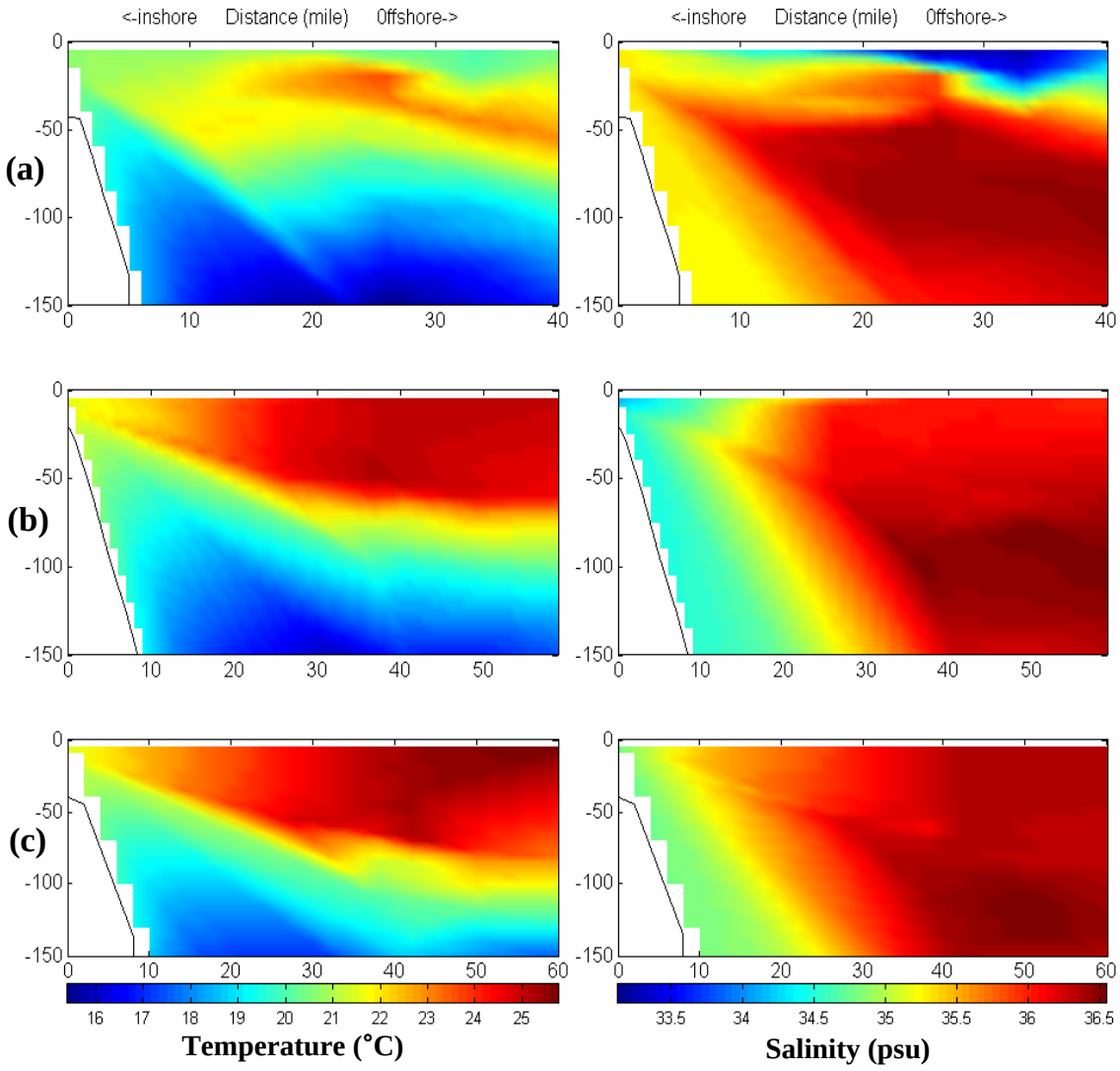

Fig. 2.7. Fall sections of potential temperature (left) and salinity (right) along line 2 of cruise (a) N1-1997, (b) N4-1998, and (c) N7-1999. Line 2 is near the Mississippi Delta (see Fig. 1.1).

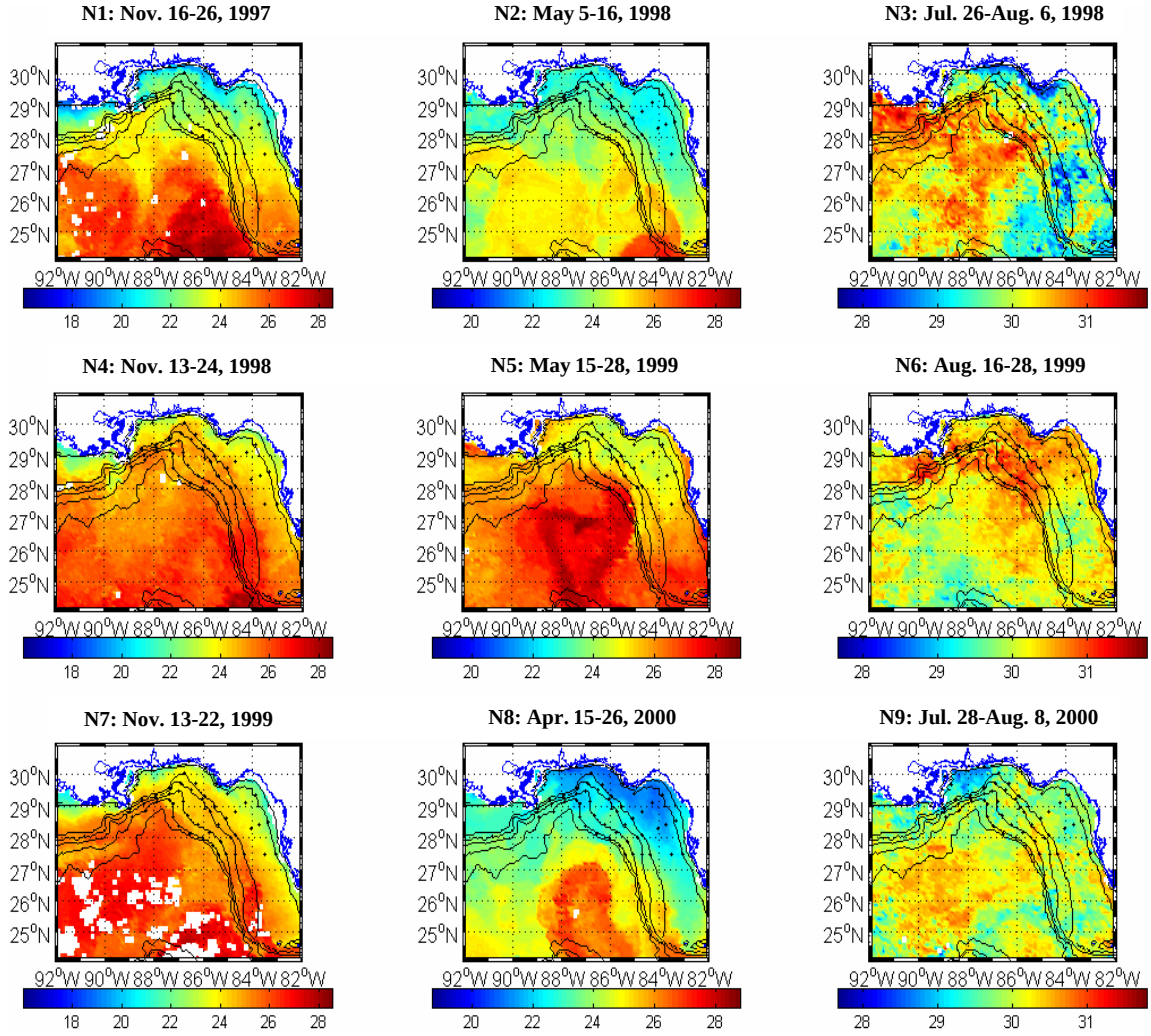

Fig. 2.8. Sea surface temperature (SST) from NOAA AVHRR satellite data averaged over each NEGOM cruise (°C).

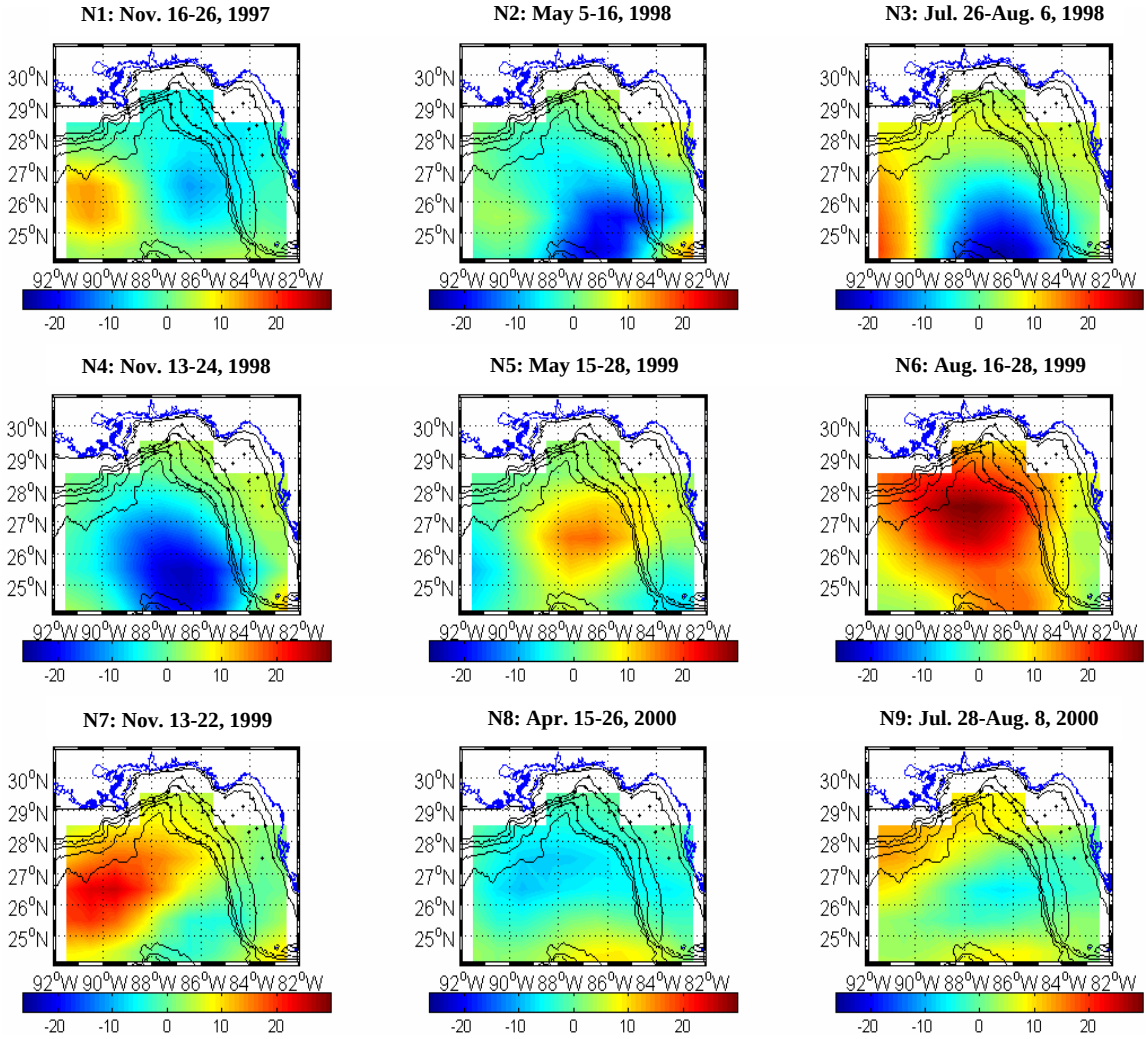

Fig. 2.9. Sea surface height anomaly (SSHA) from TOPEX/POSEIDON satellite altimeter data averaged over each NEGOM cruise (cm).

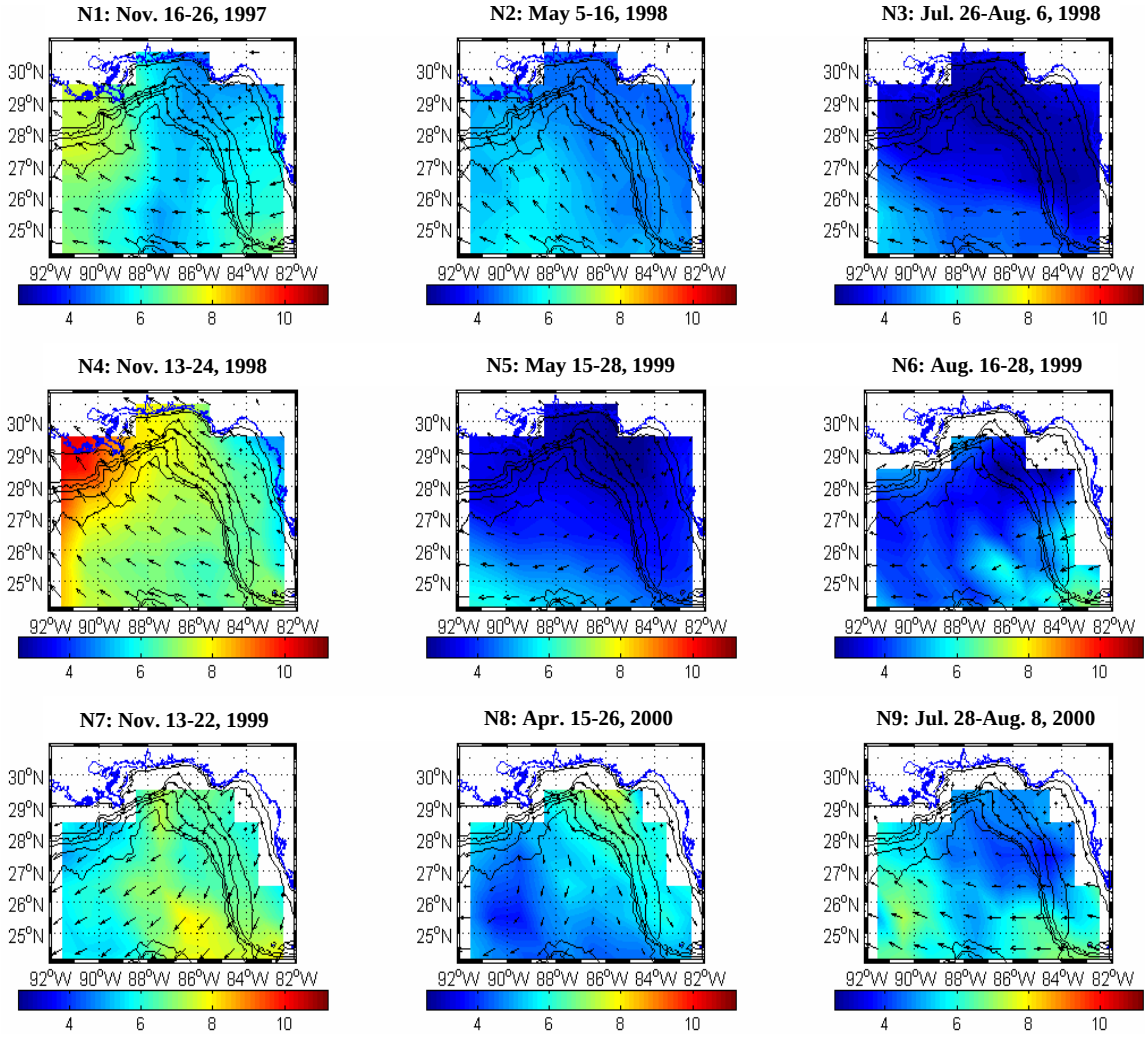

Fig. 2.10. Sea surface wind (SSW) from scatterometer data averaged over each NEGOM cruise (cm/s).

Each river system generally exhibited large discharges year-round during spring (Figs. 2.5 and 2.6, Table 2.2). Surface salinity distributions were well matched with the horizontal distribution of PM and POC. Lower salinity values extended over the outer shelf and the upper slope in the westernmost portion of the study area (Fig. 2.3).

During the spring of 1999, the water column near the Mississippi Delta was more stratified, and stratification extended seaward further than during the spring of 1998 and 2000 (Fig. 2.11). During the spring of 2000, the cold, fresh water were interrupted by the intrusion of warm and salty waters driven by Loop Current Eddies. The warm, salty water impeded the dispersion of the fresh water (Figs. 2.8 and 2.9). Although the N8 sampling season (April 2000) was earlier than other periods (May 1998 and 1999), the patterns of surface temperature corresponded well in the distribution of PM and POC. In the northern Gulf shelf areas, wind patterns changed to the north-northwest during N2, the west-northwest during N5, and southwest-southeast during N8 (Fig. 2.10).

Particle distributions were spatially similar in the fall and spring seasons between 1999-2000 and 1997-1998 but significantly different during summer seasons (1998 (N3), 1999 (N6), and 2000 (n9), Figs. 2.1 and 2.2). Higher surface PM and POC concentrations extended over the upper slope across the study area during the summer seasons. A wide swath of higher than expected concentrations was located across the midsection of the region in a northwest-southeast direction for the both PM and POC (Figs. 2.1 and 2.2). Although the absolute summer river discharge was much lower based on a seven-year average, river inputs from Mississippi were highly correlated with the positive anomalies (Figs. 2.5 and 2.6, Table 2.2).

Table 2.2. Major river discharge rates averaged over NEGOM cruises (×1,000 CFS).

	Mississippi River	Mississippi Area	Alabama Area	West Florida	Middle Florida	East Florida
N1	254.8	6.3	57.0	17.3	32.2	10.9
N2	996.8	7.4	52.7	13.8	33.6	8.8
N3	673.5	5.7	33.0	9.1	16.2	3.9
N4	377.3	3.6	20.6	16.1	17.4	5.3
N5	818.7	3.4	47.7	13.7	10.6	2.3
N6	391.4	2.1	13.7	10.2	15.4	2.3
N7	159.6	2.4	13.8	7.3	8.3	2.0
N8	589.6	23.2	190.3	9.0	22.2	3.4
N9	258.5	1.5	10.7	3.8	6.0	1.7
7 year mean*	496.5	16.1	82.3	21.2	22.5	6.3
Percentage (%)	77.0	2.5	12.8	3.3	3.5	1.0

(* is mean value of river discharges from Sep. 1997 to Dec. 2004.)

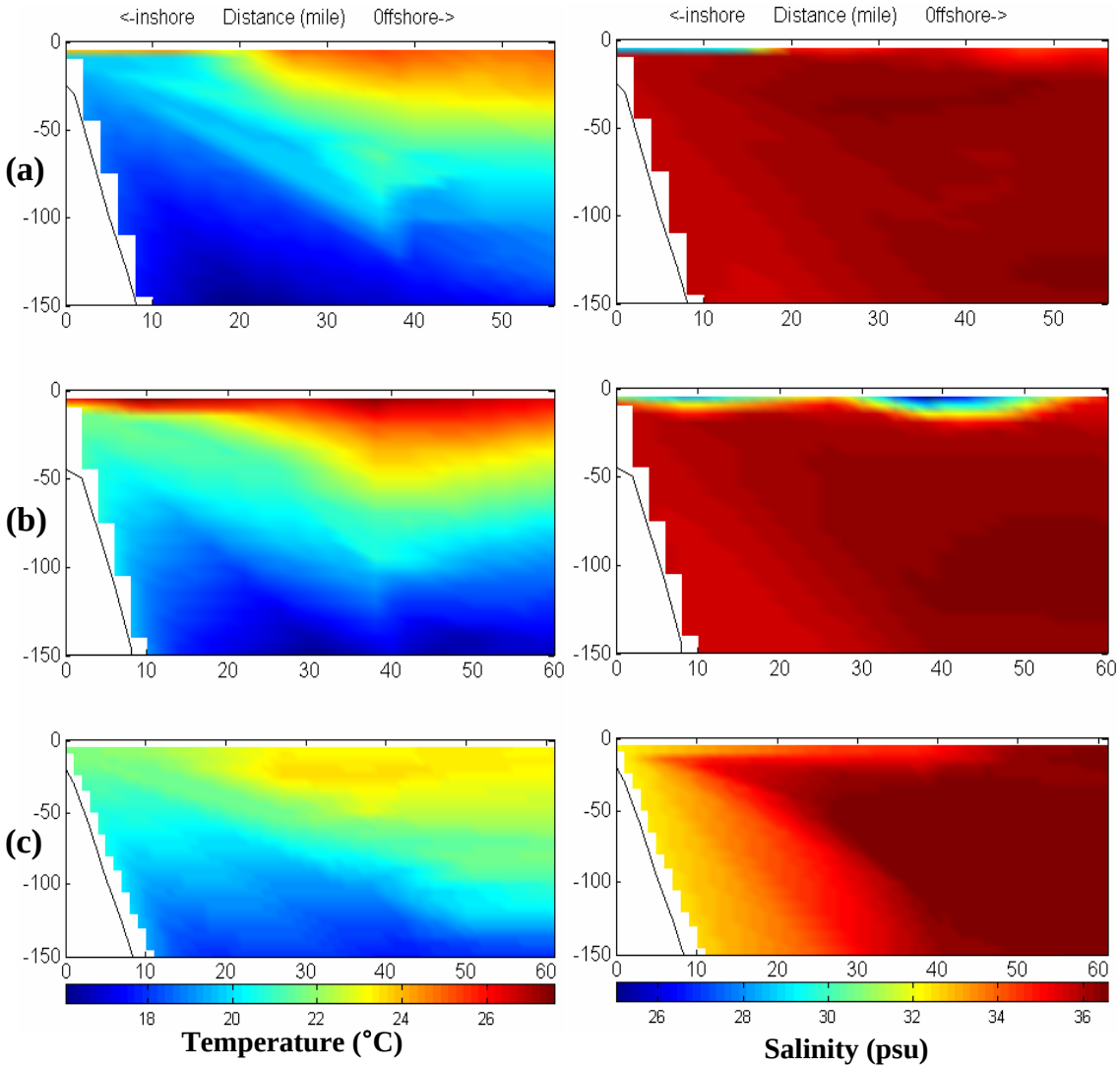

Fig. 2.11. Spring sections of potential temperature (left) and salinity (right) along line 2 of cruise (a) N2-1998, (b) N5-1999, and (c) N8-2000. Line 2 is near the Mississippi Delta (see Fig. 1.1).

During N3, wind blew west-northwest offshore. During N6, wind changed west-southwest offshore and north-northeast inshore. During N9, wind was to west-northwest offshore and north-northeast inshore (Fig. 2.10). The broad lower-salinity waters were probably discharged onto the shelf by the major rivers (Fig. 2.3), and controlled by wind stress (Fig. 2.10), stratification (Fig. 2.12), and anticyclonic and cyclonic flow of Loop Current and Eddies (Figs. 2.8 and 2.9).

The spatial patterns in the percentage of POC to PM concentrations (POC/PM ×100) on NEGOM cruises showed that higher values were more dominant in 1997 and 1998 than in 1999 and 2000, and were observed more offshore than inshore (Fig. 2.13).

2.2.2. River Discharge and Buoyancy

The fate of surface particulate material released on the northern Gulf of Mexico may be controlled by one or a combination of the following factors: (1) the fresh water inputs from major or local rivers into the northern gulf coast and buoyancy; (2) the local wind stresses induced the local shore currents; (3) anticyclonic and cyclonic flows associated with the Loop Current, Loop Current eddies. Each factor is discussed with its inference.

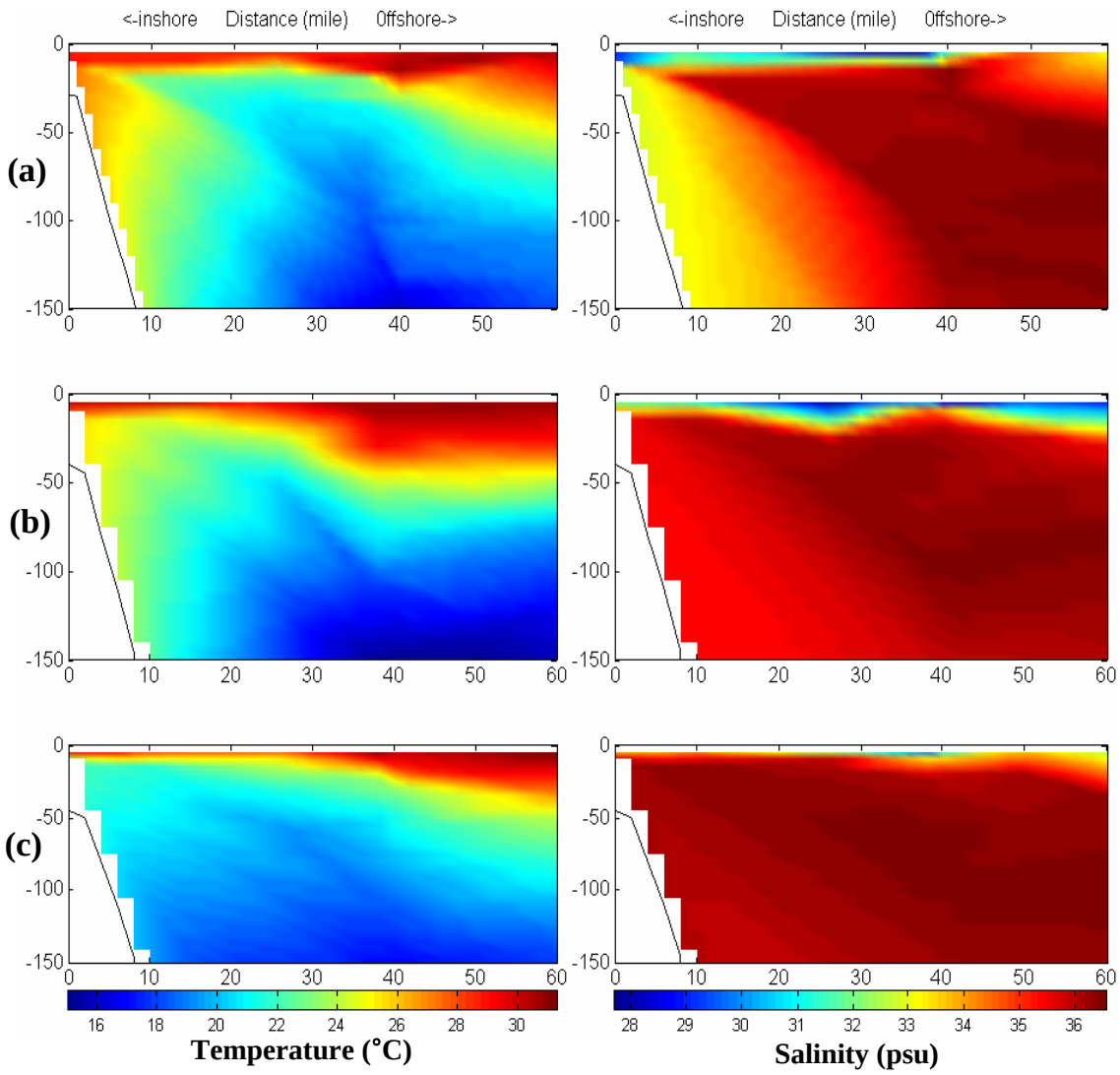

Fig. 2.12. Summer sections of potential temperature (left) and salinity (right) along line 2 of cruise (a) N3-1998, (b) N6-1999, and (c) N9-2000. Line 2 is near the Mississippi Delta (see Fig. 1.1).

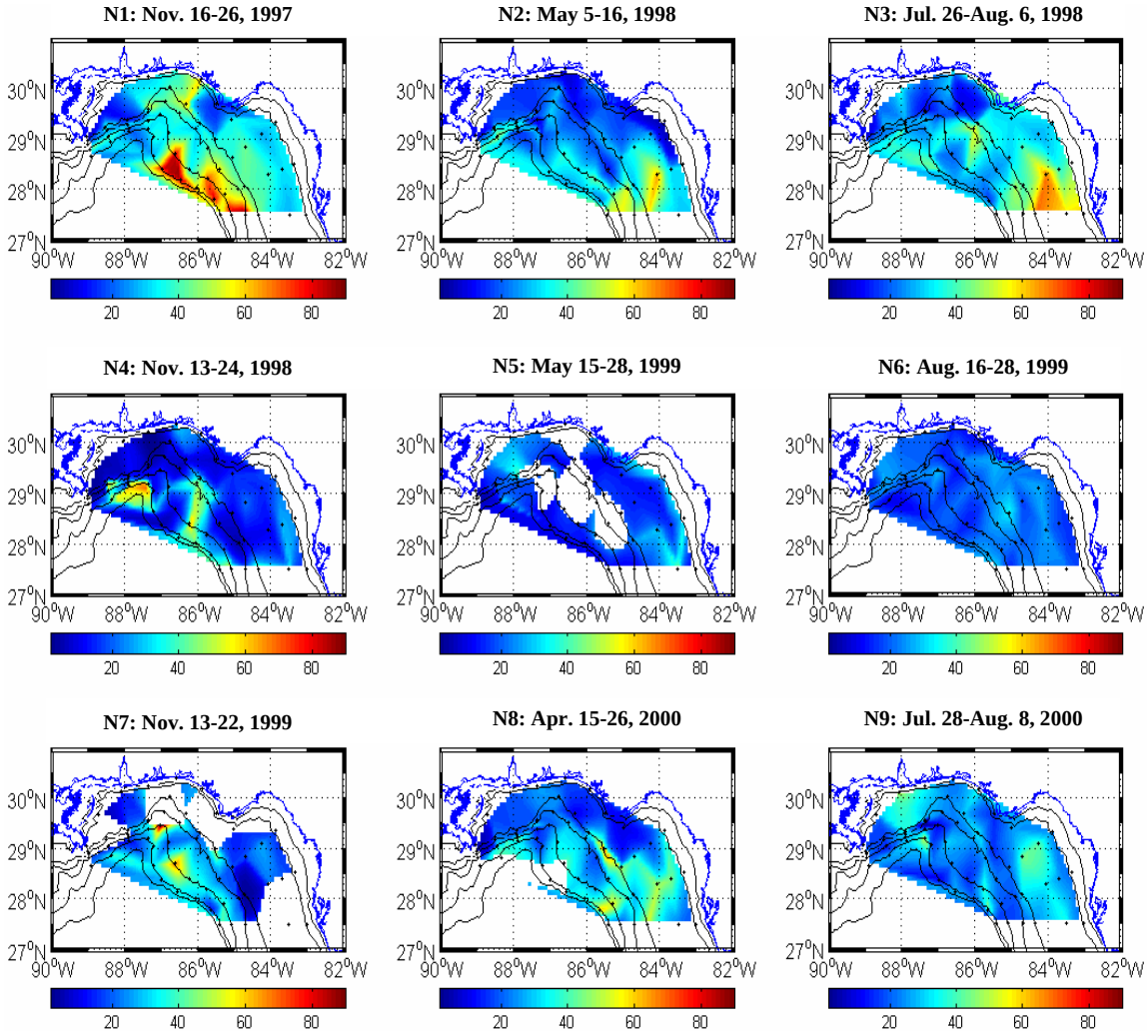

Fig. 2.13. POC percentage of PM concentration on each NEGOM hydrographic cruise $\left(\frac{POC}{PM}\times 100\right)$.

Higher concentrations of particulate materials were associated with large river inputs on the shelf areas. In the northeastern Gulf of Mexico, most fresh water flow (> 92%) entered through the Mississippi and Alabama area, and the rest of fresh water flow was discharged through Florida area (< 8%, Table 2.2). The high seasonal river discharges could provide not only a source of lithogenic and some biogenic particles but also nutrients or pollutants into the Gulf Coast. River runoff into the northern Gulf Coast had distinct annual- and inter-annual cycles, with highest flow occurring in early spring and lowest flow occurring in late summer (Fig. 2.5). The plume of particulate material in the Gulf of Mexico was associated with this discharge cycle.

The high river discharge was primarily concentrated in the coastal region of the Northern Gulf of Mexico. The Mississippi and nearby rivers (Tombigbee and Alabama River) showed a seasonal and inter-annual cycle with maximum discharge in early spring and minimum discharge in late summer and fall. The Alabama regions (Tombigbee and Alabama River) exhibited a seasonal and inter-annual cycle with maximum discharge from January to April and minimum discharge from August to October. The western Florida area (Escambia, Perdido, Blackwater, and Yellow River), middle Florida (Choctawhatchee, Ochlockonee, and Apalachicola River), and east Florida (Econfina, Fenholloway, Steinhatchee, Suwannee River) showed maximum and minimum discharge during spring and fall, and maximum outflow occurred in spring 1998 (Figs. 2.5 and 2.6).

In the Mississippi River, fresh-water discharges during NEGOM cruises generally exceeded the long-term mean with the positive anomaly except for N1, N7, N8,

and N9. The Mississippi and Alabama areas showed average or negative anomalies. Florida river values also had the mean or negative anomalies exception for the fall of 1997 (N1) and the spring of 1998 (N2) (Fig. 2.6). The river discharges for 1997 and 1998 were generally much higher than for 1999 and 2000. Unusually higher river discharges greatly influenced the Gulf of Mexico. Walker et al. (1994) noted that the fresh-water discharge due to great floods of the Mississippi River in 1993 extended out to western Florida, through the Florida Strait into the Atlantic Ocean.

An unexpected dispersion was observed during the late spring and summer seasons and did not occur during the fall seasons. This phenomenon was related to water column stratification. Stratification increased in late spring and maximized in summer, because of increasing solar radiation. The widespread fresh water was rapidly warmed by sun light, resulting in a very stable subsurface water column and increasing buoyancy of the low-density water (Walker et al., 1994). Stronger stratification increased buoyancy forcing of the fresh water that easily spread out into the Gulf due to local wind stresses and circulation systems (Oey, 1995; Morey et al., 2003). Surface temperature and salinity patterns showed that lower salinity waters corresponded with higher temperature values (Figs. 2.3 and 2.4). When stratification of the water column in late fall and early spring decreased (Figs. 2.7 and 2.11), PM and POC concentration did not disperse over the slope (Figs. 2.1 and 2.2). Although abnormally high outflow occurred in the Mississippi and Alabama areas, stratification in early spring during cruise N8 was weak (Fig. 2.11) and inhibited the dispersion of PM and POC (Figs. 2.1 and 2.2).

2.2.3. Shelf Circulation Driven by Wind Stress

Winant et al. (1987) noted that a common source of coastal circulation was wind stress. Coastal circulation was well correlated with wind directions (Blaha and Sturges, 1981; Oey, 1995; Ohlmann and Niiler, 2005). In the northern Gulf of Mexico, surface winds were to light northwest during summer and to south-southwest during the fall and winter (Morey et al., 2003). In the Mississippi River Delta, the prevailing winds are to west, to northwest from March through September and to southwest from October through February (Rhodes et al., 1985). However, the shelf circulation in the Gulf Coast showed a significantly seasonal pattern (Cochrane and Kelly, 1986; Vastano et al., 1995; Ohlmann and Niiler, 2005).

In the study area, surface winds were to the north-northeast during summer and to the west during other seasons (Wang et al., 1998). Walker (1996) inferred that particle dispersions were related to the wind patterns at the Mississippi River Delta. Surface waters with higher particle loads generally extended south toward the upper slope when eastward winds were relatively weak. The east-northeast winds caused reduced flow out of the passes west of the Mississippi delta and increased the east flow of the eastern passes. The results of numerical simulations also showed that the outflow of the Mississippi River was governed by local winds (Oey, 1995).

During the fall of 1997, the presence of moderated river discharge and increased west winds (Fig. 2.10) could induce the dispersion of particulate materials through south-southwest passes (Figs. 2.1 and 2.2), and stratification of fresh water in the upper

water column helped the dispersion of particle plumes (Fig. 2.7a). Other fall seasons did not induce the dispersion of particulate materials offshore because of vertically homogeneous water column (Figs. 2.7b and 2.7c).

During spring seasons, fresh water dispersions during N2 and N5 were related to increasing buoyancy because of the stratification of subsurface water. The northeast-ward dispersion of particulate materials was mainly affected by north-northwest winds (Figs. 2.1, 2.2, and 2.10).

Although higher outflow in the Mississippi and Alabama provided near the northern Gulf coast during winter and early spring, winds increased vertical motion and turbulence maintained particles within the mixed layer. During summer seasons, wind speeds in the northern gulf coast were relatively insignificant (Fig. 2.10) and did not explain the relationship between wind and dispersion of particles. The plumes of fresh water during summer seasons might be controlled by other factors such as the Loop Current / Loop Current Eddy (Figs. 2.8 and 2.9).

The western Florida shelf circulation was investigated by Yang and Weisberg (1999). During a winter season (October to March), Florida Big Bend Gyre induced an offshore northwest-ward flow from the south and a nearshore along shelf southeast-ward flow. In the summer seasons, there was a continuous northwest-ward flow. Many studies suggested that local currents were associated with in-shore wind stress on the western Florida shelf (Cragg et al., 1982; Mitchum and Sturges, 1982). Walker et al. (1994) noted that the Loop Current had a significant year-round effect on maintaining a higher

temperature offshore relative to waters on the West Florida Shelf and caused the southward circulation and plume.

Wind patterns and influences on northern Gulf of Mexico circulation were small compared to the Loop Current or eddy. These results could only explain a dominant mechanism for driving the circulation over the slope of the study area.

2.2.4. Loop Current and Eddies

Another important factor influencing circulation in the northern Gulf of Mexico was the Loop Current and its associated eddies. The Loop Current intrudes into the northern gulf margin near to the Mississippi River Delta. This circulation induces eastward flows over the shelf and the slope of the study area and possibly enhances the rapid eastward movement of river water (Hofmann and Worley, 1986; Smith, 1986; Schroeder et al., 1987; Hamilton et al., 1999, 2000; Sturges and Leben, 2000; Frolov et al., 2004; Romanou and Chassignet, 2004).

Both anticyclonic (warm-core) and cyclonic (cold-core) eddies that are made by separation from the main stream have been observed in the Gulf slope and basin. The anticyclones are identified by a core of high-salinity Subtropical Underwater (SUW) that becomes trapped in the rings upon separation, and are an important part of the heat and salt budget of the Gulf basin. Most anticyclones tend to move westward and eventually dissipate along the Gulf's western boundary. The cyclones can originate as cold perturbations along the northern edge of the Loop Current. They move along the eastern boundary off the western Florida Shelf, toward the south. Before reaching the Straits of

Florida, they either dissipate or move westward across the Loop Current as narrow tongues (Vukovich and Maul, 1985; Vukovich, 1995).

The widespread low-salinity plume of river water was rapidly warmed by solar heating, resulting in a very stable water mass on the continental shelf and increasing buoyancy (Walker et al., 1994). Although river discharges and winds are normal or less values (Figs. 2.5 and 2.10), the fresh water undergoes buoyant spreading and higher particulate concentrations are maintained by the shallow pycnocline (Fig. 2.12). Ohlmann and Niiler (2005) also provided that mean current variation in magnitude and direction changed from west to east, and some circulation across the shelf was related to Loop Currents and Loop Current Eddies. They play a significant role in driving circulation over the shelf rise and interact with relative fresh waters (Gilbes et al., 1996; Sahl et al., 1997).

During N1, N3, N5, N6, N7, and N9, an anticyclonic eddy was located at the southwest of the Mississippi River Delta and sometimes was elongated and extended into DeSoto Canyon (Figs. 2.8 and 2.9). This circulation induced east-ward flow over the shelf and the slope, and enhanced the rapid east-ward movement of river water. Although the outflow of the Mississippi and Alabama rivers during the summer season (N3, N6, and N9) were relatively lower, the fresh-water flows spread particle-laden water across the shelf and slope. The distribution of PM and POC offshore was affected by anticyclonic eddies. The eastern shelf of the study area was under the influence of cyclonic flow. The cyclonic eddy to the east of the anticyclone may have contributed to the north- and northwest-ward advection of warm, salty water along its eastern edge

(Romanou and Chassignet, 2004) and an upwelling through the De Soto Canyon might provide nutrient injections to the inner West Florida Shelf from deep offshore waters.

During N1, N2, N3, N4, N8, and N9, a cyclonic eddy developed on the south of the study area and under the cyclonic flow. In the West Florida Shelf, this cyclonic flow was merged with the inshore north-ward current and advected between cold and warm waters (Figs. 2.8 and 2.9). Relatively higher values in ratio of POC to PM were observed near the cyclonic eddies (Figs. 2.9 and 2.13).

According to results of the above studies, the temporal and spatial patterns of POC and PM were related to one and more factors such as river discharge, stratification, buoyancy forcing, wind stress, and Loop Current/eddies. In the fall and early spring, the distribution of POC and PM inshore was best related to river discharge and local wind stress. In the late spring and summer, the spatial and temporal pattern of PM and POC offshore was linked to increased buoyancy forcing and Loop Current/eddies.

2.3. Conclusions

To provide comparative information, physical oceanographic and ancillary data in the northern Gulf of Mexico have been combined with measurements collected concurrently from the NEGOM field program. Historical data sets include hydrography and current measurements. Concurrent data sets were identified and assembled, included SST from AVHRR satellite sensors, SSHA from satellite altimeter, and SSW from satellite scatterometer. Ancillary data was river discharge.

During NEGOM cruises from 1997 to 2000, surface particle concentrations in the northern Gulf of Mexico varied with time and location. Higher values occurred in the spring and summer and lower values in the fall. The widespread distribution pattern of higher PM and POC concentration was observed in the summer, and the small and local pattern occurred in the early spring and fall.

The temporal and spatial pattern of PM and POC were related to one or more factors such as river discharge, stratification, circulation pattern, loop current, and buoyancy forcing. The observed seasonal change in the sediment plume's response to wind speed in the western delta region resulted from seasonal changes in the upper ocean stratification. Vertical temperature and salinity measurements showed that the pycnocline in the summer lies only a few meters deep, whereas, during winter when the surface mixed layer deepens, it is on the order of 15m. During late spring and summer, the low-density river water is heated rapidly at the surface by incoming solar radiation. This lowers the density of the fresh-water plume and increases the near-surface stratification of the water column. In the absence of significant wind forcing, the plume

undergoes buoyant spreading and the sediment is maintained at the surface by the shallow pycnocline. However, when the wind speed increases substantially, wind-wave action increases vertical motion, reducing stratification, and the sediment were mixed downward rather than spreading laterally. High frequency variability in plume area and length, however, was observed and this phenomenon was unrelated to river discharge. Maximum particle concentrations over the outer shelf and the upper slope during lower runoff seasons were related to the Loop Current/eddies and buoyancy forcing.

CHAPTER III

PARTICULATE ORGANIC CARBON (POC) ALGORITHMS BASED ON THE SPECTRAL REMOTE SENSING DATA: COMPARISON WITH EMPIRICAL AND MODEL-BASED ALGORITHMS

3.1. Introduction

The major biogenic element in the ocean is carbon. Most of the inorganic carbon in the ocean exists as bicarbonate. The other main type of carbon is in the form of organic carbon, both dissolved and particulate. Carbon is fixed into organic matter in the euphotic zone through photosynthesis, and moves up the trophic levels (zooplankton, nekton). Most of the carbon in the upper ocean is recycled, but some sinks to deeper water or to the seafloor. In the ocean, organic carbon is remineralized by bacterial respiration, converting it back to inorganic carbon and producing dissolved nutrients. Oceanic carbon fluxes are generally controlled by the solubility pump and the biological pump. The solubility pump is regulated by physical processes at the air-sea interface. The biological pump is governed by phytoplankton photosynthesis, which converts CO_2 (carbon dioxide) to organic matter and provides a mechanism for sequestration of carbon in the deep ocean.

JGOFS, WOCE, and SAVE studies expanded the information of carbon distribution to global scales (Gardner et al., 1993, 1995, 1999, 2000, 2003; Chung et al., 1996, 1998; Gundersen et al., 1998; Bishop et al., 1999; Morrison et al., 2001), but it has been difficult to estimate the amount and distribution of carbon at oceanic basin and

global scales solely from ship observations, because carbon measurements from water bottle samples are a very labor and time-demanding procedure. In order to expand coverage to a global scale, new approaches are introduced to assess the distribution of POC in the ocean environment.

The ocean color signal is affected by scattering and absorption of visible and near-infrared light in seawater, as well as scattering and absorption by the inorganic, organic, particulate, and dissolved material derived from lithogenic and biogenic sources. Ocean color studies using *in situ* measurements utilize the spectral characteristics and variations of radiometric data to derive information about some of the water constituents, and provide useful information about the seasonal variations and spatial distribution of global / regional carbon production and recycling at the surface of the ocean (Stramski et al., 1999; Loisel et al., 2001; Mishonov et al., 2003; Behrenfeld et al., 2005).

Over the past two decades, most efforts were focused on predicting the concentration of marine chlorophyll *a* concentration using empirical approaches between reflectance or, equivalently, normalized water-leaving radiance and chlorophyll or pigment concentration (Sathyendranath et al., 1989; O'Reilly et al., 1998; Gower et al., 1999; Shen et al., 2001). Recently, new approaches have been developed based on optical closure relationships using model-based approaches between reflectance spectra or normalized water leaving radiance to relevant IOPs of seawater, namely, the backscattering and absorption coefficients (Bukata et al., 1981; Roesler and Perry, 1995; Garver and Siegel, 1997; Carder et al., 1999; Schiller and Doerffer, 1999; Gross et al., 2000). Model-based approaches have the greatest potential of providing accurate

retrieval of several parameters simultaneously because they attempt to model the physics of ocean color. As such, they can handle confounding conditions where multiple factors control ocean color. These models reflect our current understanding of ocean color.

These approaches still have been focused on the parameters of chlorophyll *a* and primary production. However, several attempts to estimate surface POC concentration using SeaWiFS products and *in situ* POC measurements have been made (Stramski et al., 1999; Loisel et al., 2001; Mishonov et al., 2003) and provide reasonable POC distribution on regional to global scales. These approaches used single wavelengths instead of multiple spectral bands. A single wavelength method cannot provide fully for the non-linear response in optically complex environments. An empirical POC approach based on the spectral remote sensing data is necessary for further progress, and we need model-based approaches for more accurate POC estimation. A characteristic vector analysis method using multiple wavelengths has been introduced to determine the relationship between chlorophyll concentrations and spectral wavelengths (Mueller, 1976; Gower et al, 1984; Fischer, 1985; Sathyendranath et al., 1989; Neumann et al., 1995; IOCCG, 2000; Robinson, 2004).

The purpose of this chapter is to develop efficient and suitable POC algorithms in the Gulf of Mexico based on satellite products using numerical methods; to compare POC estimates with spectral remote-sensing data; and to investigate the advantages and disadvantages of various POC algorithms. We will describe the dependence of remote sensing products and the dependence of spectral Normalized Water Leaving Radiance (Lwn) on POC concentrations.

3.2. Methods

3.2.1. Atmospheric Correction of SeaWiFS

Standard SeaWiFS atmospheric correction is used to estimate the normalized water leaving radiance and is carried out using two bands, such as 765 and 865 nm wavelengths (Gordon and Wang, 1994). The primary assumption is no water-leaving radiance at either band (zero values). The current algorithm, however, generally fails in turbid or coastal areas (Case II waters) and yields negative water-leaving radiance values at shorter wavelengths. Turbid water parameters, including suspended sediment, chlorophyll, bottom reflectance, and CDOM, cannot produce a zero value since turbid water constituents cause higher scattering. The non-zero water-leaving radiance values in the near-infrared may cause an over-estimate of aerosol optical thickness, and then this problem produces higher values in the visible part of the spectrum. Studies also indicate that the assumption of the SeaWiFS standard algorithm is not valid over the Case II waters (McClain et al., 1995; Carder et al., 1999). Although many approaches have been developed for the atmospheric correction, the problems still remain over turbid waters.

The practical method of Hu et al. (2000) is applied for this study. This method uses standard SeaWiFS software. A basic assumption is that aerosol type does not vary much over relatively small spatial scales (~ 50-100 km), and defining aerosol over less turbid water applies to the turbid area using a nearest neighbor method. This atmospheric correction scheme is tested under various atmospheric conditions over the Gulf of

Mexico and produces good results by reducing the errors of both the water-leaving radiance and chlorophyll concentration.

3.2.2. Empirical Approach

Empirical algorithms apply simple or multiple regressions between the property of interest and the ratios (or values) of irradiance reflectance or remote-sensing reflectance. They do not require a full understanding of the relationship between remote-sensing reflectance and the properties. Because of the nature of regressions, however, empirical algorithms are generally only applicable to waters with characteristics similar to those used in the algorithm development. Their applicability can be quite limited and can result in significant errors. More importantly, because of the wide variation of optical properties found for global waters, one empirical function cannot fit all waters, unless the waters are restricted to case conditions where all optical properties co-vary with chlorophyll concentrations. The biggest advantages of this kind of algorithm are the simplicity and rapidity in data processing, which are important for the retrieval of information from large data sets such as satellite images.

The most common relationship makes use of the so-called color ratio as described by :

$$P_{con} = \alpha\left(\frac{R(\lambda_i)}{R(\lambda_j)}\right)^{\beta} + \gamma \text{ or } P_{con} = \alpha R(\lambda_i)^{\beta} + \gamma \qquad (3\text{-}1)$$

Where P_{con} is water constituent to be estimated (e.g. chlorophyll concentration, suspended matter, yellow substances, and POC estimate), and $R(\lambda_i)$ is the reflectance (or

radiation) in spectral channel i. The coefficients α, β, and γ are derived from regressions between the reflectance (or radiance) ratios and the desired property (or between the reflectance (or radiance) and the desired property).

To estimate POC concentration based on an empirical approach, we compared ship-board data with satellite ocean color data obtained from the same cruise time. Using atmospheric corrections after the practical method of Hu et al. (2000), daily level 1 data from SeaWiFS ocean color data were used for spectral remote-sensing data collected from November 1997 to August 2000. SeaWiFS level 1 data at 1 km resolution were downloaded from the Goddard DAAC web site. These data were processed to Level 2 products using version 4.7 of SeaDAS. Level 2 standard mapped data include the chlorophyll concentration derived from OC4 version 4, the diffuse attenuation coefficient for downward irradiance at 490 nm (K_{490}), and normalized water-leaving radiance for all SeaWiFS channels.

For comparing satellite and hydrographic data:

1) We matched the location between NEGOM stations and SeaWiFS to extract the satellite data.

2) We then calculated the average value of each SeaWiFS parameter for the NEGOM station location. These data were interpolated to a regular grid and smoothed by averaging the data. A morphological dilation of 1 pixel was applied to cloud and land flags in each daily image, followed by a 3×3 pixel median filtering in the spatial domain to reduce noise and fill small gaps.

3) We compared POC to SeaWiFS chlorophyll *a*, K_{490}, and normalized water leaving radiance (Lwn) for all SeaWiFS channels extracted from the grid along the cruise tracks.

4) We used a least-square analysis for multiple and linear regression methods.

3.2.3. Model-Based Approach

The Principal Component Analysis (PCA) approach is used to produce a reduced variance for the analysis of information content of multi-dimensional data sets. This PCA, however, is used to determine the information of empirical or modeled data sets, to reduce (transform) the data in a manner suitable for analysis and, not least, to separate the useful information from noise contained in the data. This correlated data set is used to determine the spectral dimensionality of the data, and the weighting of each spectral channel required to estimate the geophysical variables of interest (IOCCG, 2000).

We first remove the record mean value $\mu(\lambda)$ from each normalized water leaving radiance (λ). Optionally we may also compute and remove any linear trend existing in the record as long as we are not interested in that trend. Second, we normalize the demeaned (optionally detrended) spectral wavelengths by dividing each of them by its standard deviation $\sigma(\lambda)$. This ensures that the analysis is not dominated by the variance from any given location (all locations are given an equal chance to contribute in the analysis). The resulting demeaned and normalized series $R(\lambda)$ are termed standardized series.

$$R_n(\lambda) = \sum_{i=1}^{n}\sum_{j=1}^{m}\left[\frac{T_{i,j}(\lambda)-\mu_i(\lambda)}{\sigma_i(\lambda)}\right] \quad (3\text{-}2)$$

where T is spectral remote sensing data set of original N × M matrix, i is observation number and j is measurement spectral wavelength number.

$\mu(\lambda)$ is the record mean: $\mu(\lambda) = \frac{1}{N}\sum_{i=1}^{n} T_i(\lambda)$ (3-3)

and $\sigma(\lambda)$ is the record standard deviation: $\sigma(\lambda) = \left[\frac{1}{N-1}\times\sum_{i=1}^{n}\mu_i(\lambda)^2\right]^{1/2}$ (3-4)

The normalization is especially relevant when analyzing two or more fields together, to ensure no dominance of one field over the others.

The singular value decomposition (SVD) of a matrix is based on the concept that any rectangular N × M matrix $R_n(\lambda)$ can be written as the product of three matrices: an N × N matrix U, a N × M diagonal matrix Γ with positive or zero elements, and the transpose ($V^\dagger$) of the M × M matrix V.

$$R_n(\lambda) = U \times \Gamma \times V^\dagger \quad (3\text{-}5)$$

Matrix Γ is a rectangular N × M matrix with zero elements outside the diagonal and positive or zero elements on the diagonal. The scalars on the diagonal, γ_k, are called the singular values and are typically placed in decreasing order of magnitude. Again, there is a maximum of $k \leq \min(N, M)$ non-zero singular values, which defines the maximum number of PCA modes we can determine, so that the effective dimension of matrix Γ is k × k.

An original observation vector, T, may be transformed into its characteristic system representation through the k equations.

$$PC_i = \sum_{j=1}^{n} e_{ij} \times R_j \; ; \; i = 1, 2, ..., K \; and \; j = 1, 2, ..., M \qquad (3\text{-}6)$$

where PC_i is called the *i*th principal component of R_i and e_{ij} is the *i*th characteristic vector. Thus, we effect the transformation

$(R_1, R_2, ..., R_N) \rightarrow (PC_1, PC_2, \ldots PC_k)$,

where k is selected less than or equal to N to retain the desired proportion of sample variance.

3.3. Results and Discussions

3.3.1. An Empirical Approach in Case 1 and Case 2 Waters

An empirical approach can be used to determine a relationship between the optical properties and the constituents of water using a regression equation. In Case 1 waters (open ocean), regression estimates are used to investigate the relationship between chlorophyll concentration (or water constituent) and the ratio of spectral bands (IOCCG, 2000; Robinson, 2004). In Case 2 waters (optically shallow waters), this analysis can be used to derive high concentrations of suspended particulate material from a different band ratio (IOCCG, 2000; Robinson, 2004). Case 2 waters, however, have more complex optical properties and need more spectral representation than Case 1 waters. The algorithms of these regions have to differentiate the multivariate nature of the problem.

Empirical approaches afford easy and simple processing analysis from optical properties and *in situ* measurements. These algorithms have a short computing time because of low-level complexity (simple regression equation). Although they have low or moderate accuracy of prediction, they can be used to easily implement the desired range of measurements. They can derive stable results for regional/global scales.

3.3.2. Empirical Approach with POC and SeaWiFS Products (Chlorophyll and K_{490})

Many studies are used to estimate POC concentration based on Inherent and Apparent Optical Properties (IOP, AOP), such as the radiance, reflectance, absorption, scattering, and beam attenuation. They show a linear relationship with POC concentrations and provide good estimates of POC in surface water (Gardner et al., 1993, 1995, 2005; Walsh et al., 1995; Loisel and Morel, 1998; Bishop, 1999; Bishop et al., 1999; Claustre et al., 1999; Stramski et al., 1999; Loisel et al., 2001; Mishonov et al., 2003). The particulate beam attenuation data is dominated by particles in the phytoplankton size. It is also sensitive to inorganic particles (detrital particles) in the 0.5 to 20 μm size range (Kitchen et al., 1982; Stramski and Kiefer, 1991; Boss et al., 2001). Particulate backscatter coefficient is dominated by submicron particles, but field populations have a significant tail in the phytoplankton size domain (Morel and Ahn, 1991; Stramski and Kiefer, 1991; Osvaldo et al., 1994; Ulloha et al., 1994; Loisel et al., 2001). The study of Cho and Azam (1990) showed that in oligotrophic waters bacterial biomass averaged 40% of POC. However, Stramski et al. (1999) demonstrated that the particulate backscatter coefficient was well correlated with POC. Loisel et al. (2001)

investigates the correlation between particulate backscatter coefficient and chlorophyll / POC. Therefore, particulate backscatter may be more useful in determining the phytoplankton and bacteria carbon than POC.

However, use of beam attenuation data may be restricted for expanded temporal and spatial variations because beam attenuation cannot be determined from remotely sensed AOPs, and it can be difficult to convert ocean color inversion algorithms.

In this study, an empirical algorithm to predict POC based on remotely sensed data was developed using *in situ* measurements collected in the northern Gulf of Mexico from 1997 to 2000, in areas that covered a wide range of water types. Each of 9 cruises was carried out along the same 11-track line. SeaWiFS products included chlorophyll pigment concentration, K_{490}, and spectral normalized water leaving radiance (Lwn). The numerical values of SeaWiFS parameters were extracted from the daily pixel-by-pixel mean values at each NEGOM cruise. They were used to estimate the POC concentration using the least-squares fit method.

In the first approach, we were looking for a correlation between SeaWiFS products and POC concentration. SeaWiFS products (chlorophyll and K_{490}) had similar patterns with POC concentrations in the study area (Figs. 2.2, 3.1, and 3.2). Higher values of both products were found along the inner shelf, especially between the Mississippi delta and Mobile Bay. Lower values were located over the outer shelf and the upper slope. In the fall seasons (N1, N4, and N7 cruises), higher values were constrained to the Mississippi River Delta region and the inner shelf of the study area. In the rest of the study area, values dramatically decreased normal to bathymetry lines. In the spring seasons (N2, N5, and N8 cruises), the higher values were slightly extended over the outer slope in the Mississippi River Delta and broadly distributed along the inner shelf of the study area. Lower values were found over a wide expanse of the rest of the study area. In the summer seasons (N3, N6, and N9 cruises), higher values extended from the Mississippi delta to the shelf break and across the upper slope of the study area. Lower values were found over the rest of the shelf and slope (Figs. 3.1 and 3.2).

The following ranges of variation of *in situ* POC concentration and SeaWiFS products were expected in our study area;

(1) POC concentration: $10 \leq POC \geq 900$ mg/m^3.

(2) Chlorophyll concentration: $0.01 \leq Chl \geq 40$ mg/m^3.

(3) Diffuse attenuation coefficient at 490 nm (K_{490}): $0.01 \leq K_{490} \geq 1.9$ m^{-1}.

These ranges were chosen to cover all the values that are generally encountered.

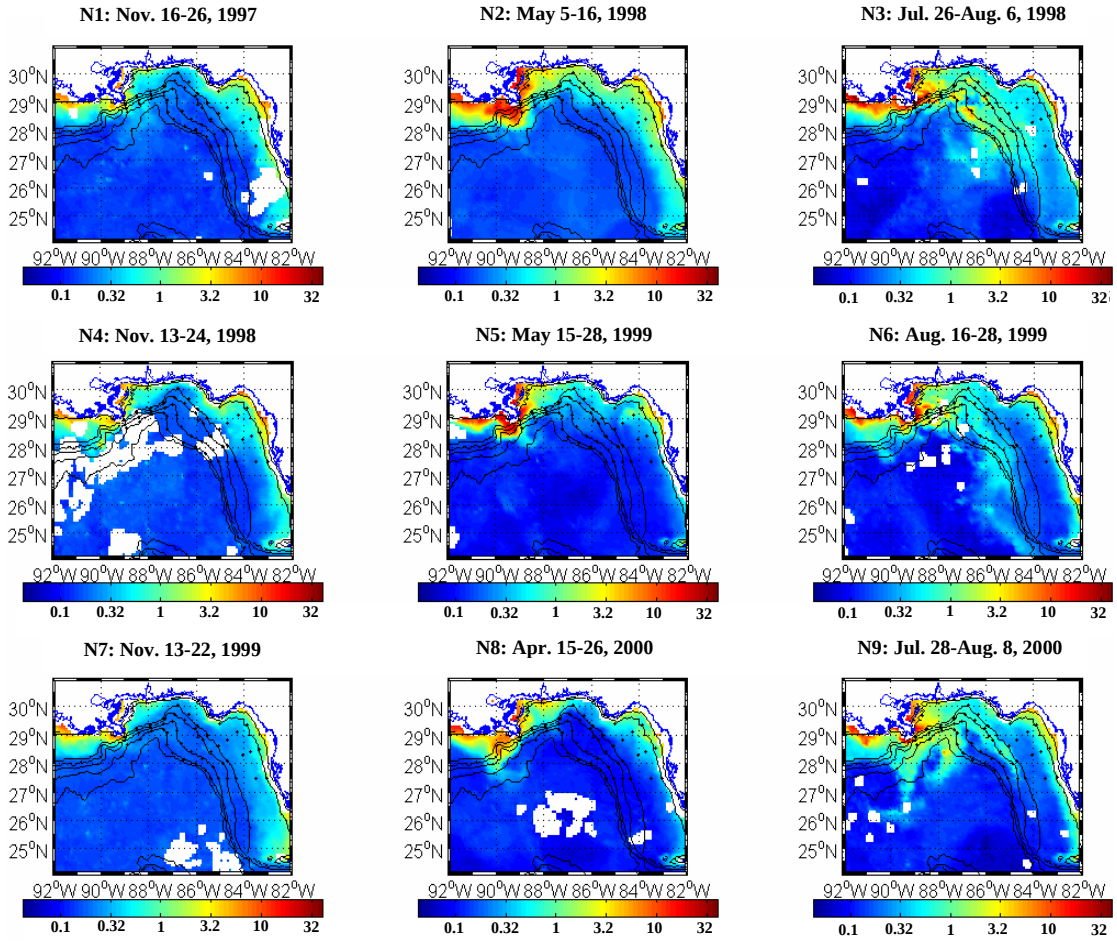

Fig. 3.1. SeaWiFS surface chlorophyll concentration (mg/m^3) averaged over each NEGOM hydrographic cruise.

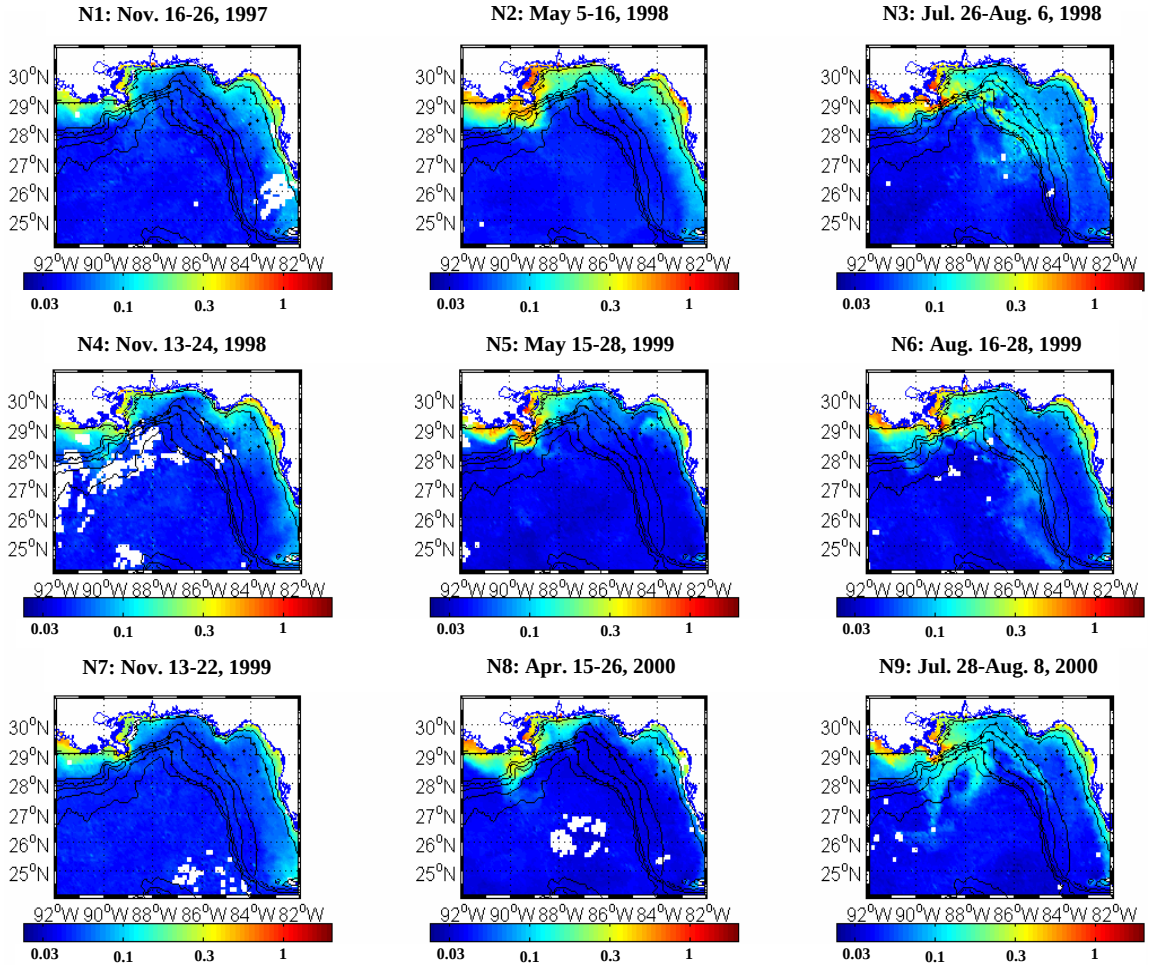

Fig. 3.2. SeaWiFS surface diffuse attenuation coefficient at 490 nm (m^{-1}) averaged over each NEGOM hydrographic cruise.

Sathyendranath et al. (1989) suggest that the logarithmic transformation can enhance the linearity of both data sets. If the variation of each value is large, this transformation can generally help to linearize the system. However, when we used a logarithm function, our data still did not provide a good correlation between chlorophyll or K_{490} and POC. The transformed data increased the linearity, but the data were very scattered at the lower values of both data sets.

A regression between POC and chlorophyll concentrations using a quadratic polynomial function based on equation 3-7 in Table 3.1, showed a fairly constant relationship (R = 0.90, Figs. 3.3a and 3.3b). Our measurements and the result of Loisel and Morel (1998) suggest that lower POC concentrations have a good relationship with lower chlorophyll values, but the correlation was not as tight between higher POC and chlorophyll values. Although the RMS error was small (Table 3.2), the difference between measured and calculated data increased at N3, N5, N8, and N9, which were seasons that showed relatively higher surface POC concentrations.

The regression between POC and K_{490} used a quadratic polynomial function based on equation 3-8 in Table 3.1. The correlation was strong (R=0.86, Table 3.1, Figs. 3.3c and 3.3d), but it also was less sensitive at higher POC concentrations. The root mean square (RMS) error also increased at higher POC measurements (spring and summer seasons, Table 3.2). The standard K_{490} algorithm used the ratio of Lwn(490) to Lwn(555), but the peak of the radiance varied from 490 nm to 555 nm, particularly in green and brown coastal water (Dudek et al., 2003).

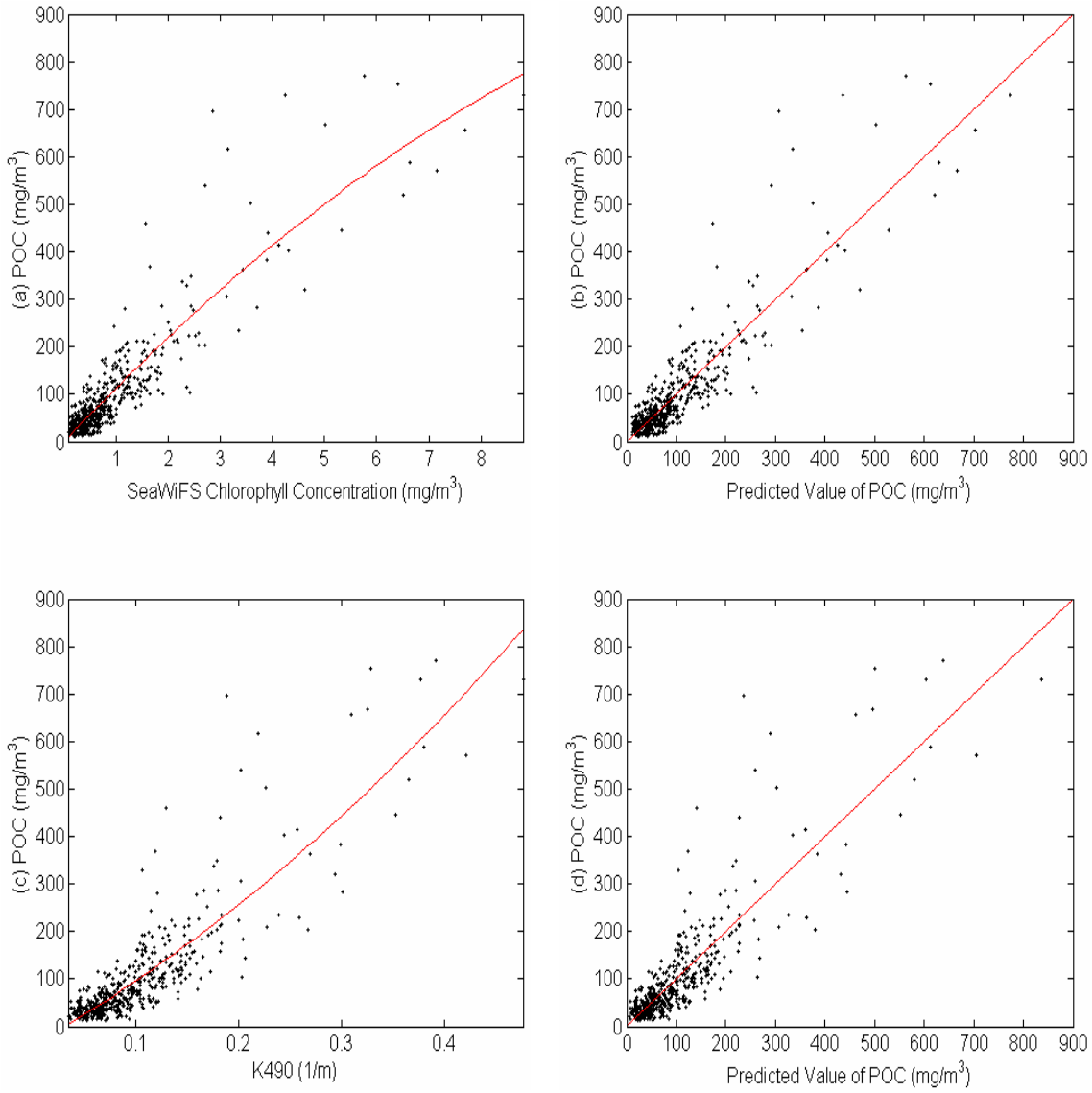

Fig. 3.3. A least-squares fit regression between (a) POC and SeaWiFS chlorophyll concentration and (c) POC and K_{490}. Scatter plots of (b) POC vs. predicted value of POC using equation 3-7 and (d) POC vs. predicted value of POC using equation 3-8 during NEGOM hydrographic cruises. Equation statistics are in Table 3.1. Red lines in (b) and (d) are the 1:1 line.

Table 3.1. The least-square fit of linear or multiple regressions between POC and SeaWiFS products, between POC and ratio of normalized water leaving radiance.

Products/ function	Equation	a	b	c	d	e	R
Chl QP	3-7. $Y=a\times X^2 + b\times X + c$	-3.2607	116.49	0.2832			0.90
K_{490} QP	3-8. $Y=a\times X^2 + b\times X + c$	1289.3	-39.353	-39.353			0.86
Lwn(555) QP	3-9. $Y=a\times X^2 + b\times X + c$	-280.33	60.484	60.484			0.90
Lwn(670) QP	3-10. $Y=a\times X^2 + b\times X + c$	-1615	977.8	6.4021			0.88
2 bands P	3-11. $Y_{log} =a\times R_{412} + b$	-0.9147	2.0259				-0.82
2 bands P	3-12. $Y_{log} =a\times R_{443} + b$	-1.1457	2.1426				-0.84
2 bands P	3-13. $Y_{log} =a\times R_{490} + b$	-1.6404	2.2963				-0.86
2 bands CP	3-14. $Y =a\times R_{555}^3 + b\times R_{555}^2 + c\times R_{555} + d$	-322.5	1788.3	-3318	2104.7		-0.89
3 bands Multiple linear	3-15. $Y_{log} =a\times R_{510} + b\times R_{670} + c$	-2.805	-0.140	2.205			0.86
3 bands Multiple linear	3-16. $Y_{log} =a\times R_{510} + b\times R_{490} + c$	-2.563	-0.083	2.310			0.86

Table 3.1. (continued)

Products/ function	Equation	a	b	c	d	e	R
5 bands Multiple linear	3-17. $Y_{log} = a \times R_{412} + b \times R_{443} + c \times R_{490} + d \times R_{510} + e$	0.896	-2.065	1.629	-3.096	2.289	0.86
2 bands QP	3-18. $Y=a \times SR^2 + b \times SR + c$	497.26	516.6	170.28			0.85
5 bands CP	3-19. $Y=a \times MSR^3 + b \times MSR^2 + c \times MSR + d$	675.71	1288.4	864.15	235.07		0.89

*(*Chl*=SeaWiFS chlorophyll concentration based on NASA standard OC4 algorithm,

$$R_{412} = \log_{10}\left(\frac{Lwn(412)}{Lwn(555)}\right), R_{443} = \log_{10}\left(\frac{Lwn(443)}{Lwn(555)}\right), R_{490} = \log_{10}\left(\frac{Lwn(490)}{Lwn(555)}\right),$$

$$R_{510} = \log_{10}\left(\frac{Lwn(510)}{Lwn(555)}\right), R_{555} = \left(\frac{Lwn(510)}{Lwn(555)}\right), R_{670} = \log_{10}\left(\frac{Lwn(670)}{Lwn(555)}\right),$$

$$SR = \left(\frac{Lwn(555) - Lwn(443)}{Lwn(555) + Lwn(443)}\right),$$

$$MSR = \left[\frac{\left\{\frac{Lwn(555)}{Lwn(510)} - \frac{(Lwn(412) > Lwn(443) > Lwn(490))}{Lwn(510)}\right\}}{\left\{\frac{Lwn(555)}{Lwn(510)} + \frac{(Lwn(412) > Lwn(443) > Lwn(490))}{Lwn(510)}\right\}}\right],$$

Y=POC estimation, $Y_{log}=\log_{10}(POC)$, P = Power function, QP = Quadratic Polynomial function, CP=Cubic Polynomial function).

Table 3.2. The Root Mean Square (RMS) between the measured and calculated data (Number of regression equation is shown in Table 3.1).

RMS/ Equation	N1	N2	N3	N4	N5	N6	N7	N8	N9	Total RMS
3-7	28.0	45.6	79.0	27.9	52.2	48.8	18.7	126.2	75.0	49.3
3-8	30.4	49.5	94.3	35.1	58.8	48.1	22.0	142.7	88.4	56.3
3-9	32.8	42.7	93.6	38.2	51.2	44.4	36.4	30.4	47.4	49.9
3-10	36.5	43.7	101.6	49.9	66.8	42.1	44.1	31.8	49.7	55.1
3-11	31.8	62.3	117.0	52.8	75.0	53.7	16.6	36.6	112.6	70.5
3-12	28.2	53.9	115.3	51.1	66.2	47.5	16.0	30.7	93.7	63.9
3-13	27.2	50.5	101.5	48.7	63.9	41.8	17.1	25.0	66.8	55.3
3-14	27.5	49.5	87.1	46.7	50.6	51.9	22.6	30.5	58.8	51.0
3-15	29.9	47.5	98.9	49.5	53.9	42.9	17.3	24.0	63.9	53.2
3-16	29.5	44.3	99.7	47.7	52.2	42.9	18.7	23.8	62.3	52.4
3-17	29.1	49.2	125.3	49.3	51.7	43.1	17.9	23.2	59.9	58.6
3-18	33.9	69.3	95.8	49.4	55.1	51.9	17.8	44.0	77.1	59.6
3-19	25.6	53.1	93.4	47.2	49.1	46.7	17.3	28.2	59.1	51.6
3-22 (PCA)	36.7	33.2	84.8	30.7	47.6	44.4	24.2	30.0	54.9	46.6

However, the current NASA global algorithms generally over-estimate chlorophyll concentrations at low pigment concentrations and under-estimate chlorophyll at higher concentrations (McClain et al., 1995; Carder et al., 1999; Stramska et al., 2003). The results of POC estimates using chlorophyll and K_{490} data were under-predicted at higher POC concentrations and slightly over-predicted at lower POC standing stocks. Although the POC: phytoplankton carbon ratio had a good relationship, phytoplankton carbon represents only 19-49% of POC (Eppley et al., 1992; DuRand et al., 2001; Gundersen et al., 2001). Cho and Azam (1990) suggested that the sum of bacterial carbon and phytoplankton carbon was generally about one-half of POC.

The plot of POC measurements vs. POC estimates showed more scatter at higher concentrations than at lower values (Figs. 3.3b and 3.3d). However, there was no significant difference between on-shore and offshore data, or by season in terms of the POC to SeaWiFS products relationship (Richardson et al., 2003). The correlation between K_{490} and POC was slightly less than between *Chl* and POC.

Adsorption and backscatter coefficients were well correlated with POC (Stramski et al., 1999), but had zero values at lower concentrations in our study (Son et al., 2004).

3.3.3. Empirical Approaches between POC Concentrations and Spectral Radiances

In the second approach, empirical regressions were used to quantify correlations between the spectral radiances and surface POC concentrations. The radiance, recorded by the SeaWiFS ocean color sensor, penetrates the air-water interface, interacts with water surface and water constituents, and then exits the water column. This radiance in spectral bands is differentially sensitive to concentrations of optical constituents and provides valuable information about the internal bulk characteristics of the water column. In general, spectral reflectance of clear water drops continuously after about 580 nm due to absorption in the water column. As the suspended sediment concentration is increased, reflectance increases at the visible and near-infrared wavelengths for both organic and inorganic contents. Organic constituents produced approximately 10 percent lower volume reflectance at all wavelengths than inorganic matter. Reflectance increased in the 580 – 690 nm regions and in the near-infrared region as more minerals were suspended in the water. Thus, the peak reflectance shifts toward longer wavelengths in the visible as suspended sediment concentrations increased (Lodhi et al., 1997). Suspended sediment concentrations generally have a significant relationship with near-infrared bands (713-880 nm, $r > 0.9$, Bhargava and Mariam, 1990; Han and Rundquist, 1994). Therefore, by measuring the wavelength of radiance that is reflected (emitted) by targets on surface water over a variety of different wavelengths, we can compile a spectral response for various objects.

The following ranges of variation for spectral normalized water leaving radiance can be expected in our study area;

(1) $0.0 \leq Lwn(412) \geq 45$ mw/cm^2/μm/sr.

(2) $0.0 \leq Lwn(443) \geq 35$ mw/cm^2/μm/sr.

(3) $0.0 \leq Lwn(490) \geq 20$ mw/cm^2/μm/sr.

(4) $0.0 \leq Lwn(510) \geq 10$ mw/cm^2/μm/sr.

(5) $0.0 \leq Lwn(555) \geq 10$ mw/cm^2/μm/sr.

(6) $0.0 \leq Lwn(670) \geq 10$ mw/cm^2/μm/sr.

In this study, spectral radiances driven from the ocean water were used to estimate the POC concentration. When the POC concentrations in the surface water increased, the peak of radiance increased at the longer visible wavelength (555 nm, green band). As surface POC concentration decreased, radiances increased at the shorter visible band (412 nm and 443 nm, violet). Radiance at 510 nm did not change significantly with various POC concentrations (relatively constant signal). The radiance peak shifted toward longer visible wavelengths as more particulate organic carbon was added (Fig. 3.4a).

The signals of the spectral wavelengths in the fall and early spring seasons were higher at shorter wavelengths than for the late spring and summer seasons (Fig. 3.4b). However, the information extracted from the spectral response curve is used to estimate POC concentrations and yield regional and global POC algorithms.

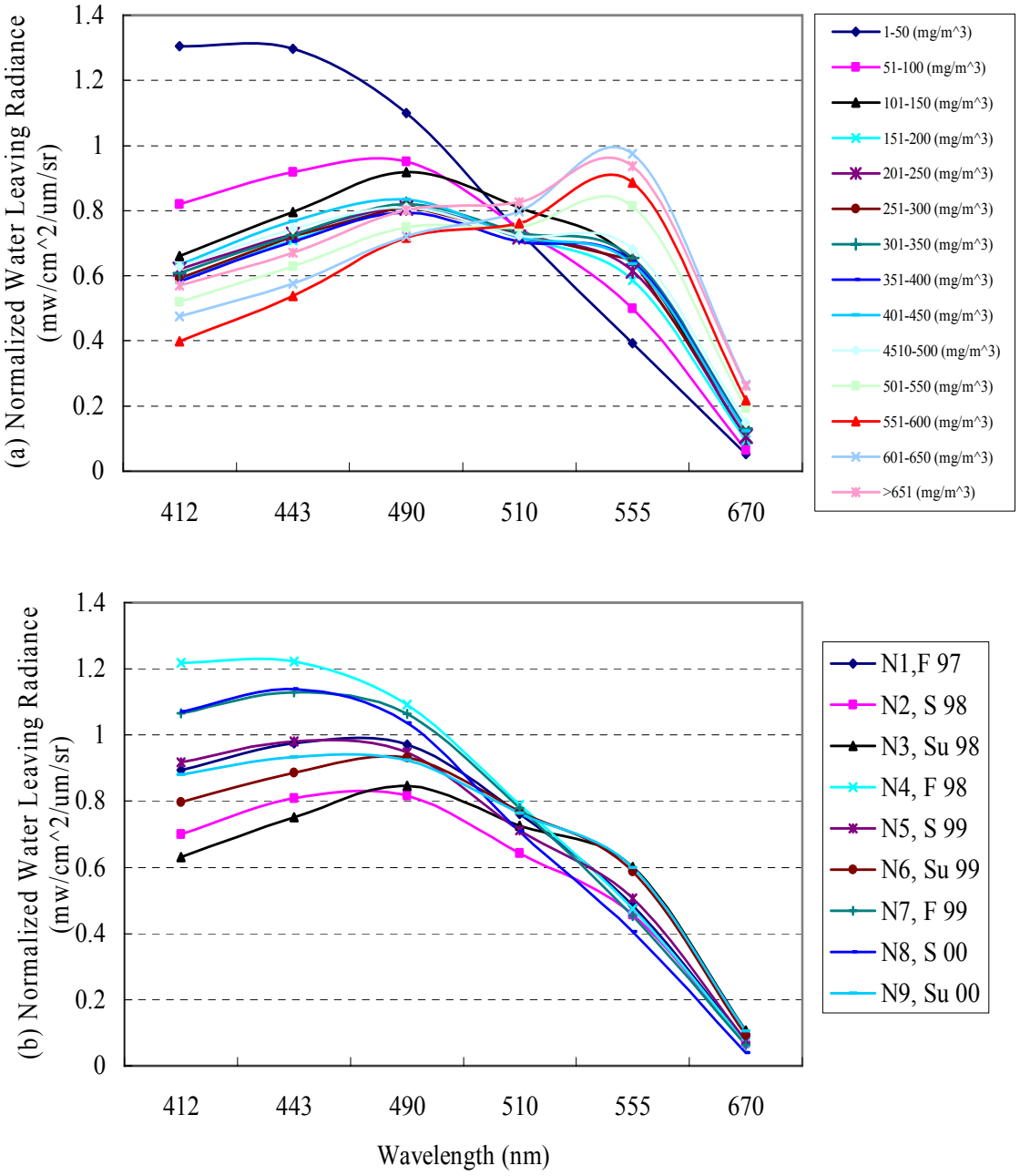

Fig. 3.4. Normalized water leaving radiance with various levels of (a) averaged and binned POC concentration over all NEGOM cruises (1-750 mg/m^3) and (b) averaged for all data of each NEGOM hydrographic cruise. For POC, the peak radiance shifted toward longer wavelengths as concentration increased.

Figs. 3.5 and 3.6 provide the correlation between spectral normalized water leaving radiances and POC concentration (Table 3.1). Shorter visible wavelengths (412 ~ 510 nm) were not significantly correlated with POC concentrations (R values varying from -0.006 to 0.64, Fig. 3.5).

The regression approach used the quadratic polynomial function using equation 3-9 in Table 3.1. Normalized water leaving radiances at 555 nm (Lwn(555)) were well correlated with lower and higher POC concentration but scattered at moderated POC concentrations (R = 0.90, Table 3.1, Figs. 3.6a and 3.6b). RMS error was relatively small (Table 3.2) except during N3 and N5 cruises. Stramski et al. (1999) used the remote sensing reflectance at 555 nm (Rrs(555)) for correlation instead of Lwn(555). They suggested that POC measurements were highly correlated with Rrs(555). However, a single band approach using Lwn(555) was well developed and used to estimate surface POC concentration (Mishonov et al., 2003).

Another single band regression used the quadratic polynomial function of equation 3-10 in Table 3.1. The correlation in normalized water leaving radiance at 670 nm (Lwn(670)) was over-estimated with lower POC concentration and scattered at higher POC concentrations (R=0.88, Figs. 3.6c and 3.6d). RMS error was also large (Table 3.2).

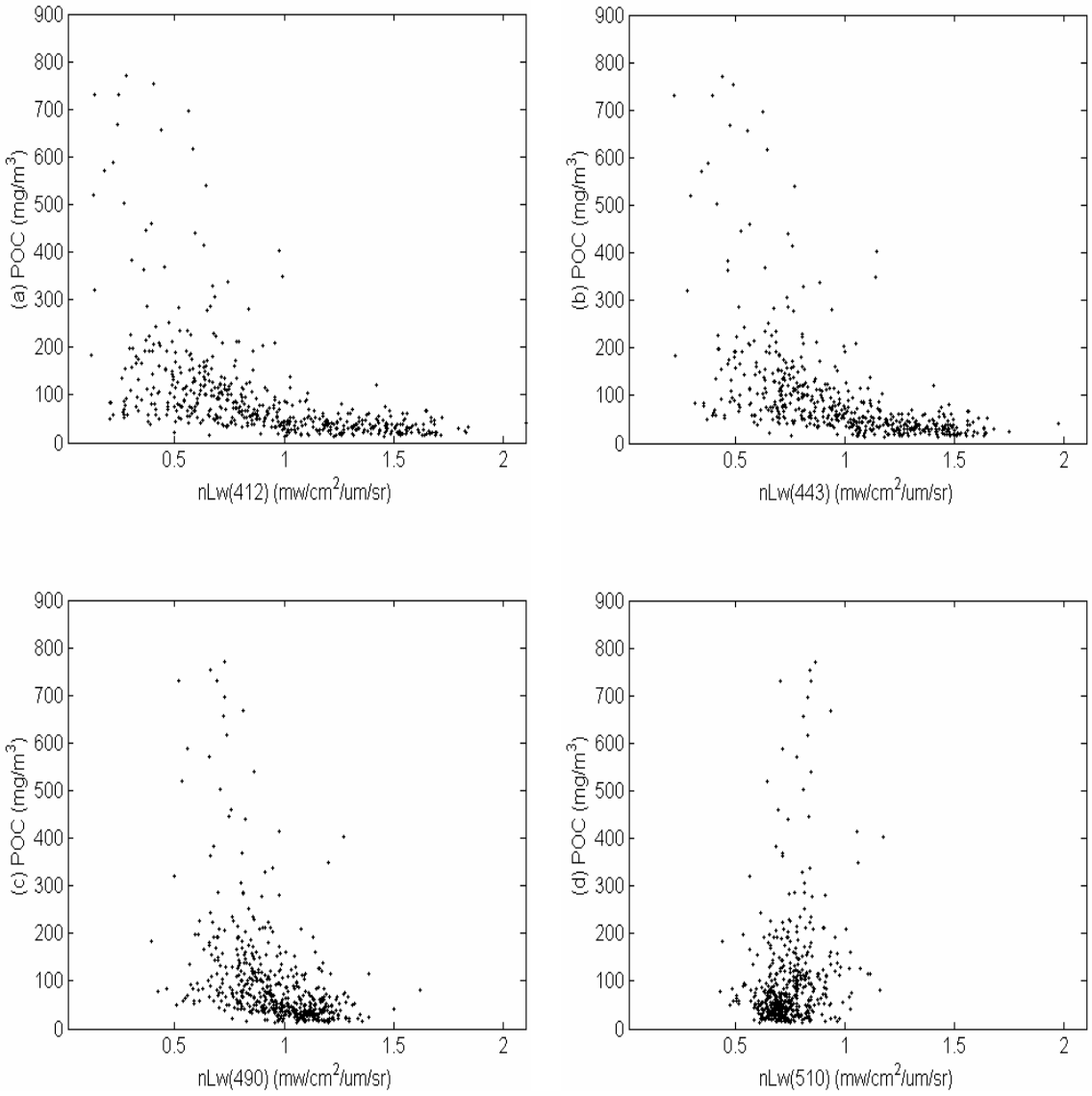

Fig. 3.5. Scatter plots of (a) POC and Lwn(412), (b) POC and Lwn(443), (c) POC and Lwn(490), and (d) POC and Lwn(510) on all NEGOM hydrographic cruises.

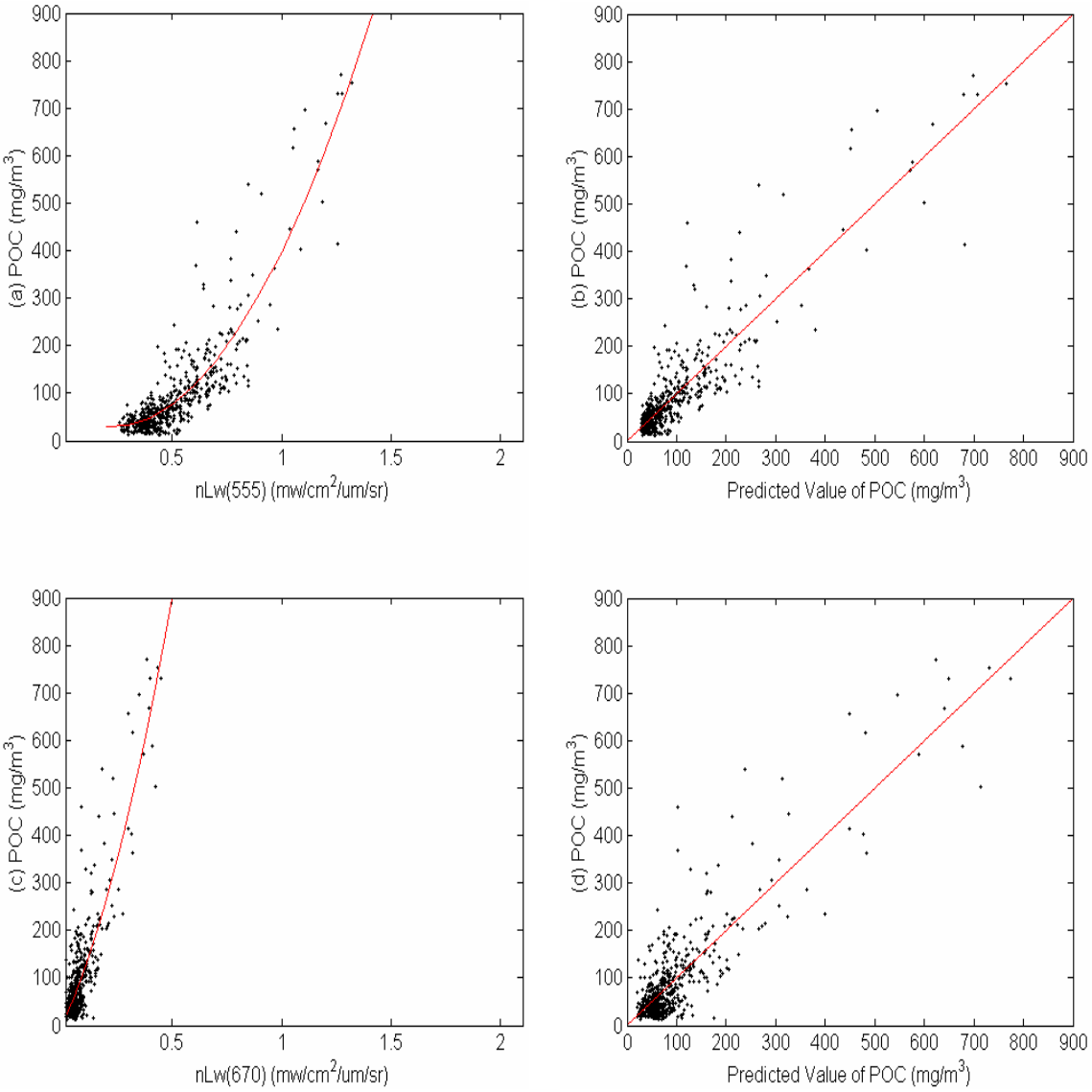

Fig. 3.6. A least-squares fit regression between (a) POC and Lwn(555) and (c) POC and Lwn(670). Scatter plots of (b) POC vs. predicted value of POC using equation 3-9 and (d) POC vs. predicted value of POC using equation 3-10 during NEGOM hydrographic cruises. Equation statistics are in Table 3.1. Red lines in (b) and (d) are the 1:1 line.

However, lower values of POC concentrations were well correlated with radiance of longer visible wavelengths, but higher POC concentrations have less correlation because of existing phytoplankton, heterotrophic microorganisms as well as nonliving organic particles. In these complicated conditions, spectral radiances could not provide peaks for each optical constituent, but yield a mixed signal of water constituents. Using a single radiance approach would be difficult to separate each peak of the radiance from compound substances in the water column. For this reason, different correlations can be expected to produce different results.

In the third approach, we used the blue-to-green ratio (using the 555 nm wavelength as the normalizing factor), because Lwn(555) has a comparatively small effect on absorption relative to the particulate and dissolved substances. These ratios are less sensitive to possible errors in the atmospheric correction than the magnitude of normalized water leaving radiance at a single wavelength. Thus, these regressions can provide good estimates of POC concentration ($R \geq -0.82$, Table 3.1, Figs. 3.7 and 3.8).

These approaches applied a logarithmic transformation, and the results of the square-fit regression method had an inverse correlation between POC concentration and each blue-to-green ratio. Although the predicted POC values using the ratio of Lwn(412) to Lwn(555) and Lwn(443) to Lwn(555) (equation 3-11 and 3-12 in Table 3.1) had a good relationship ($R \geq -0.82$), these approaches were under-estimated at higher POC concentrations (Fig. 3.7). The RMS error was overall large (Table 3.2).

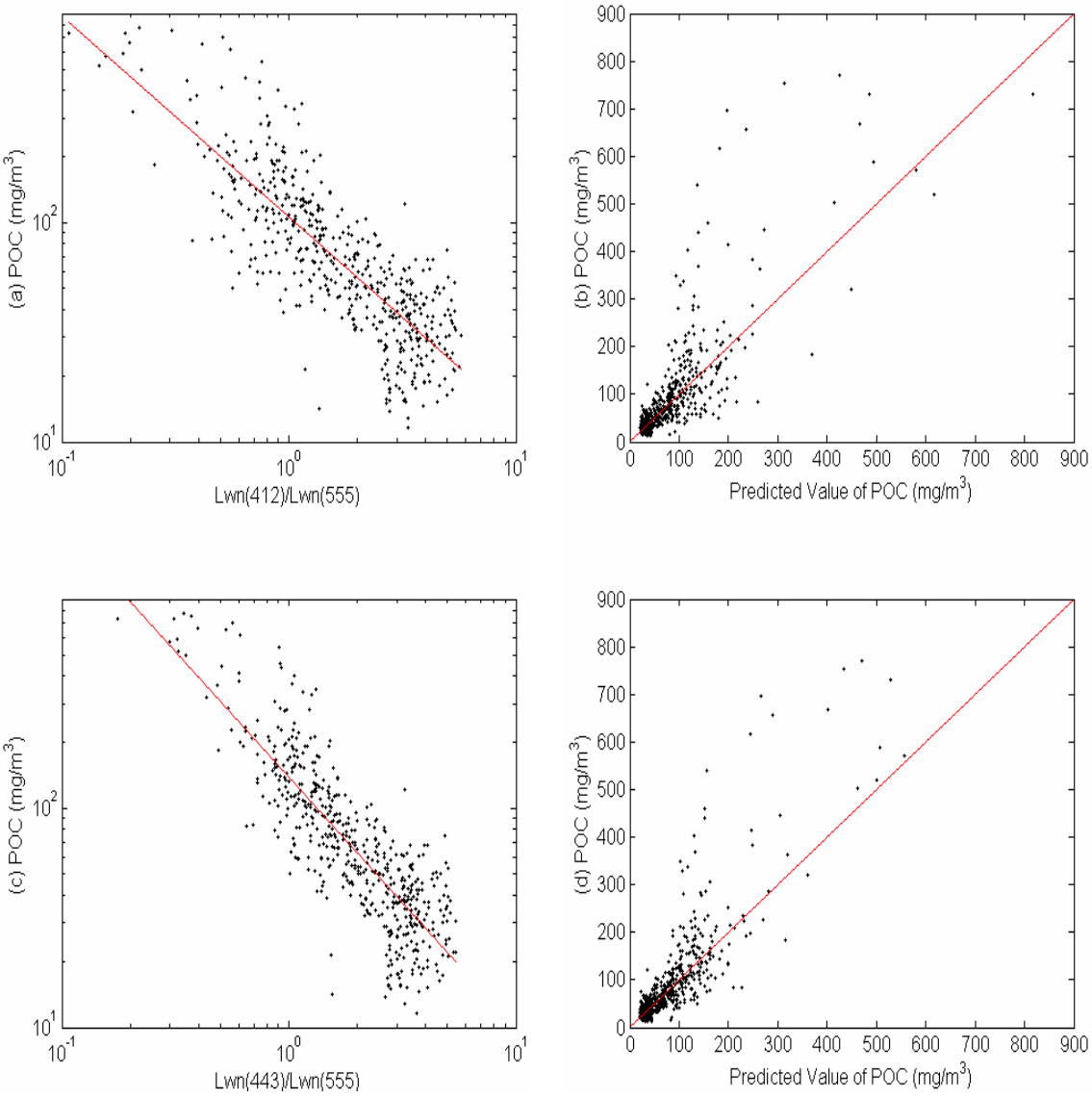

Fig. 3.7. A least-squares fit of regression between (a) POC and Lwn(412)/Lwn(555) and (c) POC and Lwn(443)/Lwn(555). Scatter plots of (b) POC vs. predicted value of POC using equation 3-11 and (d) POC vs. predicted value of POC using equation 3-12 during NEGOM hydrographic cruises. Equation statistics are in Table 3.1. Red lines in (b) and (d) are the 1:1 line.

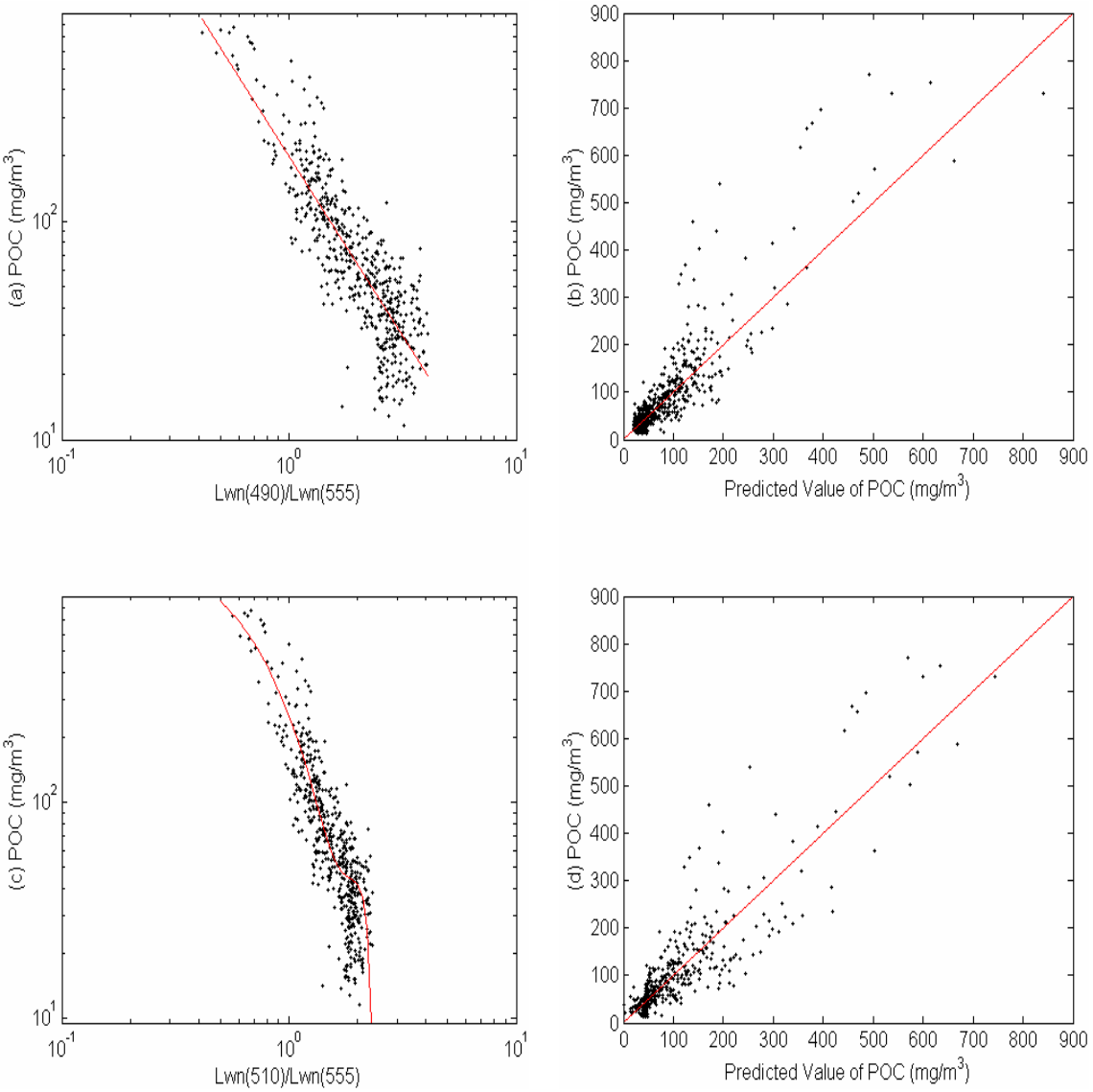

Fig. 3.8. A least-square fit regression between (a) POC and Lwn(490)/Lwn(555) and (c) POC and Lwn(510)/Lwn(555). Scatter plots of (b) POC vs. predicted value of POC using equation 3-13 and (d) between POC vs. predicted value of POC using equation 3-14 during NEGOM hydrographic cruises. Equation statistics are in Table 3.1. Red lines in (b) and (d) are the 1:1 line.

The ratio of Lwn(490) to Lwn(555) using equation 3-13 in Table 3.1 was well correlated with lower POC concentrations but scattered at higher POC concentrations (R=-0.86, Table 3.1, Figs. 3.8a and 3.8b). The high scatter was affected by PM in surface layers of shallow water (Case 1 water), and by bottom effects through the water column. The topography of the water surface (rough and smooth) caused the increasing scattering attenuations and the resulting errors making it were difficult to disentangle true signals (Lee and Carder, 2002).

The approach using the ratio of Lwn(510) to Lwn(555) was a better estimate of POC concentration than other blue-to-green ratios (R=-0.89, Table 3.1, Figs. 3.8c and 3.8d). This regression used the cubic polynomial function using equation 3-14 in Table 3.1. The predicted values of POC were less scattered at various levels of POC concentrations with an especially good correlation at higher POC concentrations. RMS error was relatively low compared to other approaches (Table 3.2).

In Fig. 3.9, three different approaches of estimating POC concentration using multiple regressions were well correlated between *in situ* measurement and predicted value (Table 3.1, R=0.86). The first approach used the multiple least-square fit regression using equation 3-15 in Table 3.1. It was used to investigate the correlation between the ratio of Lwn(510) to Lwn(555) and of Lwn(670) to Lwn(555) (Fig. 3.9a). The second approach used the multiple square-fit regression using equation 3-16 in Table 3.1, and provided the correlation between the ratio of Lwn(490) to Lwn(555) and of Lwn(510) to Lwn(555) (Fig. 3.9b).

The third approach used the multiple least-square fit regression using equation 3-17 in Table 3.1, and determined the correlation among the ratio of Lwn(412) to Lwn(555), of Lwn(443) to Lwn(555), of Lwn(490) to Lwn(555), and of Lwn(510) to Lwn(555) (Fig. 3.9c). All of them had similar RMS errors and results, but multiple regressions using the ratio of Lwn(490) to Lwn(555) and Lwn(510) to Lwn(555) should be a better POC estimate than the other two approaches (Fig. 3.9 and Table 3.1 and Table 3.2).

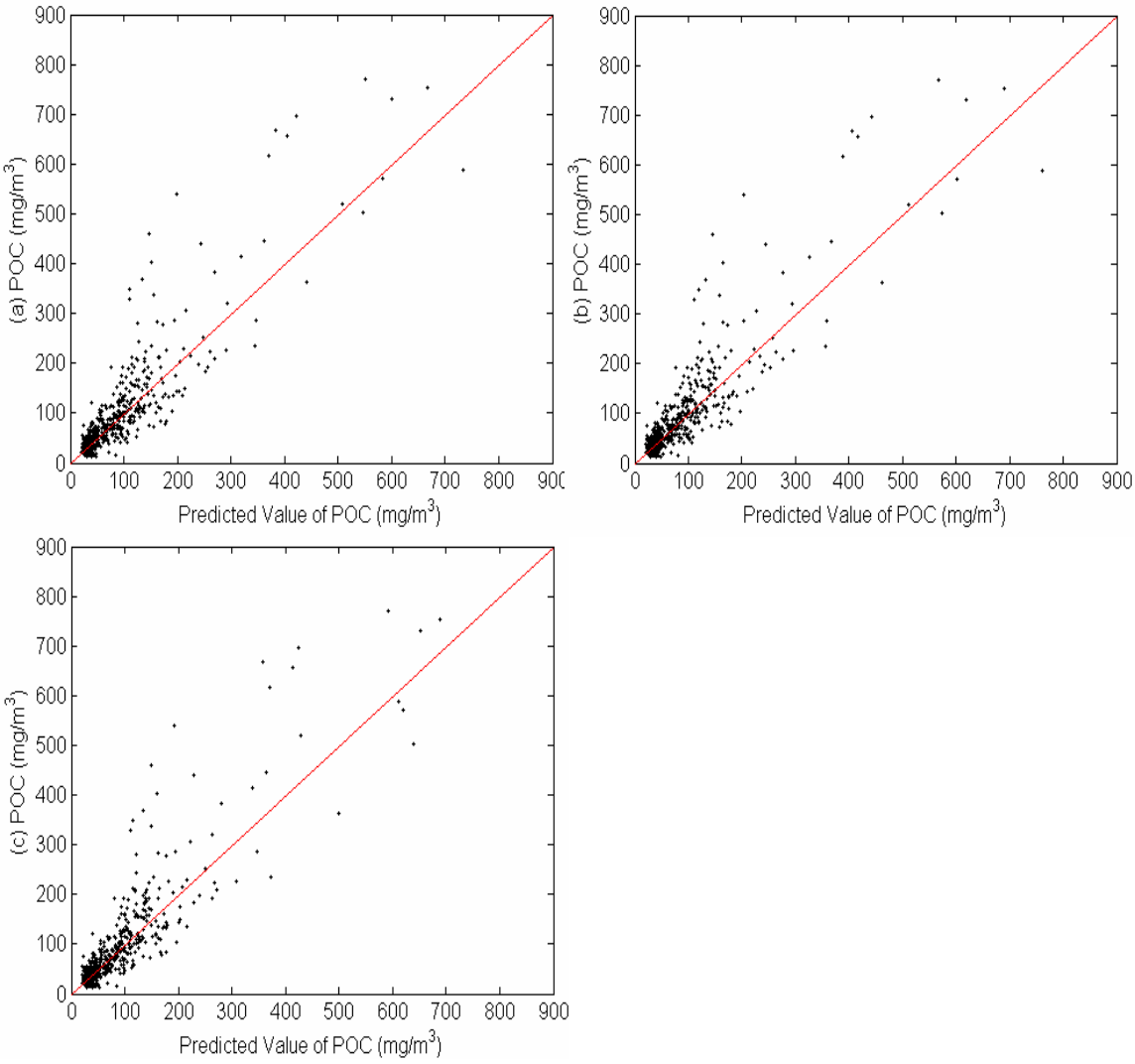

Fig. 3.9. Scatter plots of the results of three different multiple regression methods. (a) The correlation between POC and predicted value of POC using Lwn(510)/Lwn(555) and Lwn(670)/Lwn(555) in equation 3-15, (b) Lwn(490)/Lwn(555) and Lwn(510)/Lwn(555) in equation 3-16, and (c) Lwn(412)/Lwn(555), Lwn(443)/Lwn(555), Lwn(490)/Lwn(555), and Lwn(510)/Lwn(555) in equation 3-17 during NEGOM hydrographic cruises. Equation statistics are in Table 3.1. Red lines are the 1:1 line.

In a fourth approach, we used for the simple ratio method to estimate the POC concentration using equation 3-18 in Table 3.1. According to Fig. 3.4a, when surface POC concentrations increased (decrease), the peak radiance shifted toward the longer (shorter) wavelengths. We could identify POC concentrations based on the spectral response of the normalized water leaving radiance. A simple ratio approach was used to determine the relationship between two high/low signal bands;

$$\text{Simple Ratio} = \left[\frac{\left(Lwn(555) - Lwn(443)\right)}{\left(Lwn(555) + Lwn(443)\right)}\right] \tag{3-20}$$

When higher POC concentrations were found in ocean surface water, the signal values of simple ratios increased. When lower POC concentrations were present, simple ratios decreased (Fig. 3.10a). The plot between measured and calculated data was scattered at various levels of POC concentrations (Fig. 3.10b). This result using the simple ratio approach shows a high RMS error at the oceanic POC standing stock (Table 3.2).

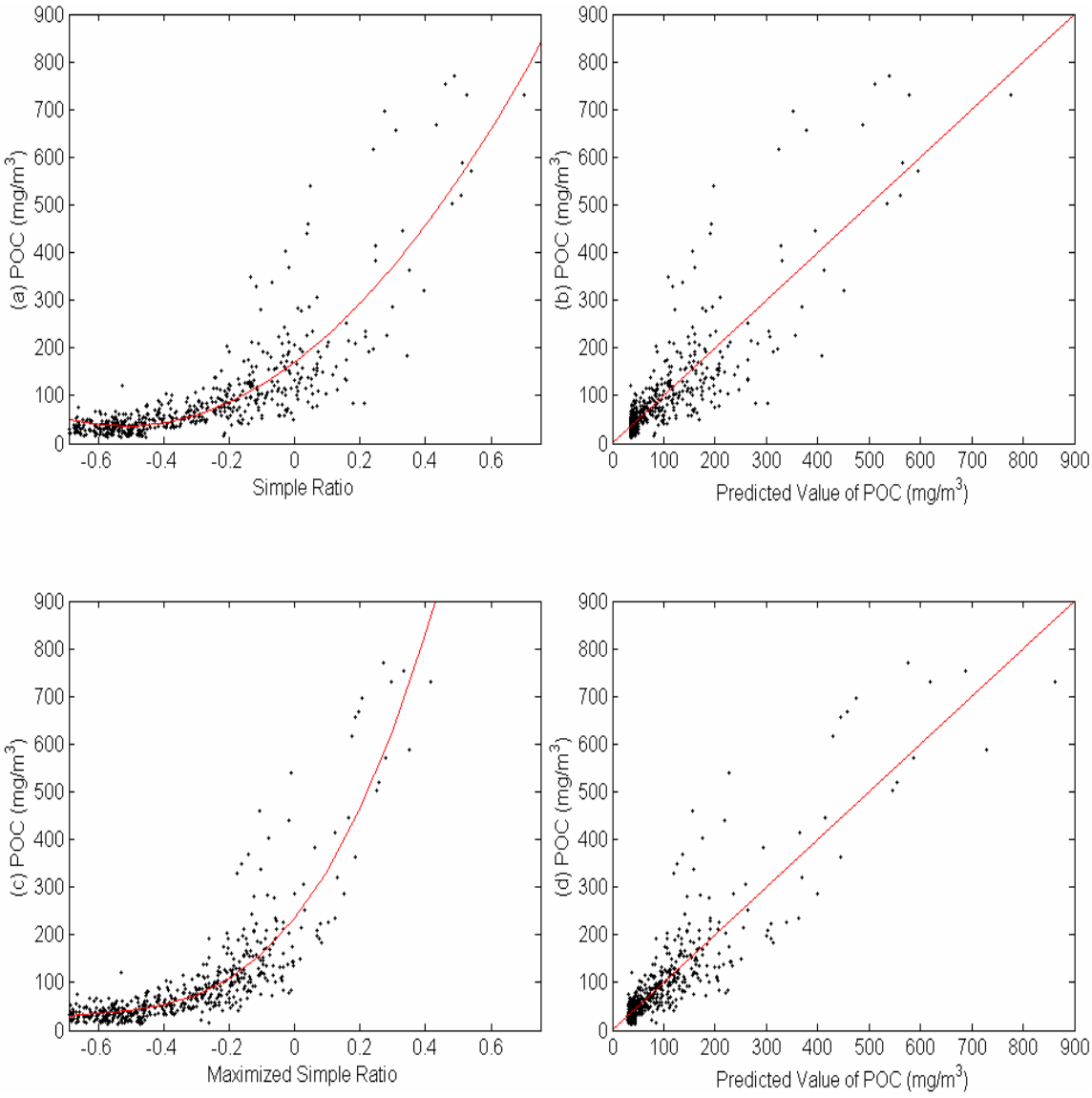

Fig. 3.10. A least-squares fit regression between (a) POC and simple ratio and (c) POC and maximized simple ratio. Scatter plots (b) POC vs. predicted value of POC using equation 3-18 and (d) POC vs. predicted value of POC using equation 3-19 during NEGOM hydrographic cruises. Equation statistics are in Table 3.1. Red lines in (b) and (d) are the 1:1 line.

Another approach, the maximized simple ratio, was based on the idea of the simple ratio, but used all blue-to-green bands in equation 3-19 in Table 3.1. To reduce the scatter of the radiance signal, we applied the Lwn(510) as a normalizing factor. In the shorter visible wavelengths, the value of the radiance peak used the maximum value among Lwn(412), Lwn(443), and Lwn(490), and was then normalized by Lwn(510). In the green visible wavelengths, the ratio of Lwn(555) to Lwn(510) was considered;

$$MSR = \left[\frac{\left\{ \frac{Lwn(555)}{Lwn(510)} - \frac{(Lwn(412) > Lwn(443) > Lwn(490))}{Lwn(510)} \right\}}{\left\{ \frac{Lwn(555)}{Lwn(510)} + \frac{(Lwn(412) > Lwn(443) > Lwn(490))}{Lwn(510)} \right\}} \right] \tag{3-21}$$

Higher values were found at higher POC concentrations, and lower values were found at lower POC standing stocks (Fig. 3.10c). It had a relatively lower RMS error (Table 3.2) and was useful for extracting the signal information at high POC standing stock (R value = 0.89, Figs. 3.10c and 3.10d).

3.3.4. A Model-Based Approach in Case 1 and Case 2 Waters

The PCA method suggests the relationship between the spectral responses in different bands, and enhances the potential discrimination and reconstruction accuracy of yielded constituents (Mueller, 1976; Gower et al, 1984; Fischer, 1985; Sathyendranath et al., 1989; Neumann et al., 1995; IOCCG, 2000). PCA algorithms can be optimized to take into account regional or seasonal variations by applying regional optical models to derive the weighting coefficients for the estimator.

The spectral normalized leaving radiance collected from SeaWiFS ocean color sensor was extracted at each NEGOM station, digitized, and averaged. Each spectral wavelength removed the trend from the mean values of each spectrum. This de-trended data included 6 wavelengths at 526 stations and was analyzed using PCA to obtain the orthogonal planes and reduced dimensions of the simulated data. The PCA calculated the eigenvalue and eigenvector of the dimensionally reduced data. The weighting factors of the first five characteristic vectors were calculated. The correlation between these weighting factors and POC concentrations were applied using multiple linear regression. This approach reduces the data to a small number of orthogonal vectors and the corresponding weight factors for each sample. The reduced data set simplifies the task of information extraction.

Fig. 3.11a illustrates the total variance (eigenvalue) from the PCA approach. The first mode (87.63%) was clearly dominant, followed by a very steep drop in variance of second and third modes. The second and third modes accounted for 9.85 and 2.21% of the total variance. The first three modes accounted for 99.69% of total sample variance, and the first five modes accounted for 99.94% of total variance; virtually all of the variance.

In Fig. 3.11b, the radiance peak in the mean value of each spectral band occurred at the shorter wavelengths and rapidly dropped off in the green and red visible wavelengths. The eigenvector of the first mode showed that the radiance peak occurred at shorter wavelengths. The radiance peak in the second eigenvector occurred at 555 nm, and the third eigenvector was at 490 nm. The rest of the eigenvectors had double peak wavelengths but no significant eigenvalues (0.18 and < 0.07 % of total variance, Fig. 3.11a). However, the orthogonality of the radiance signals of the individual components will determine our ability to recover these components from the total radiance spectrum.

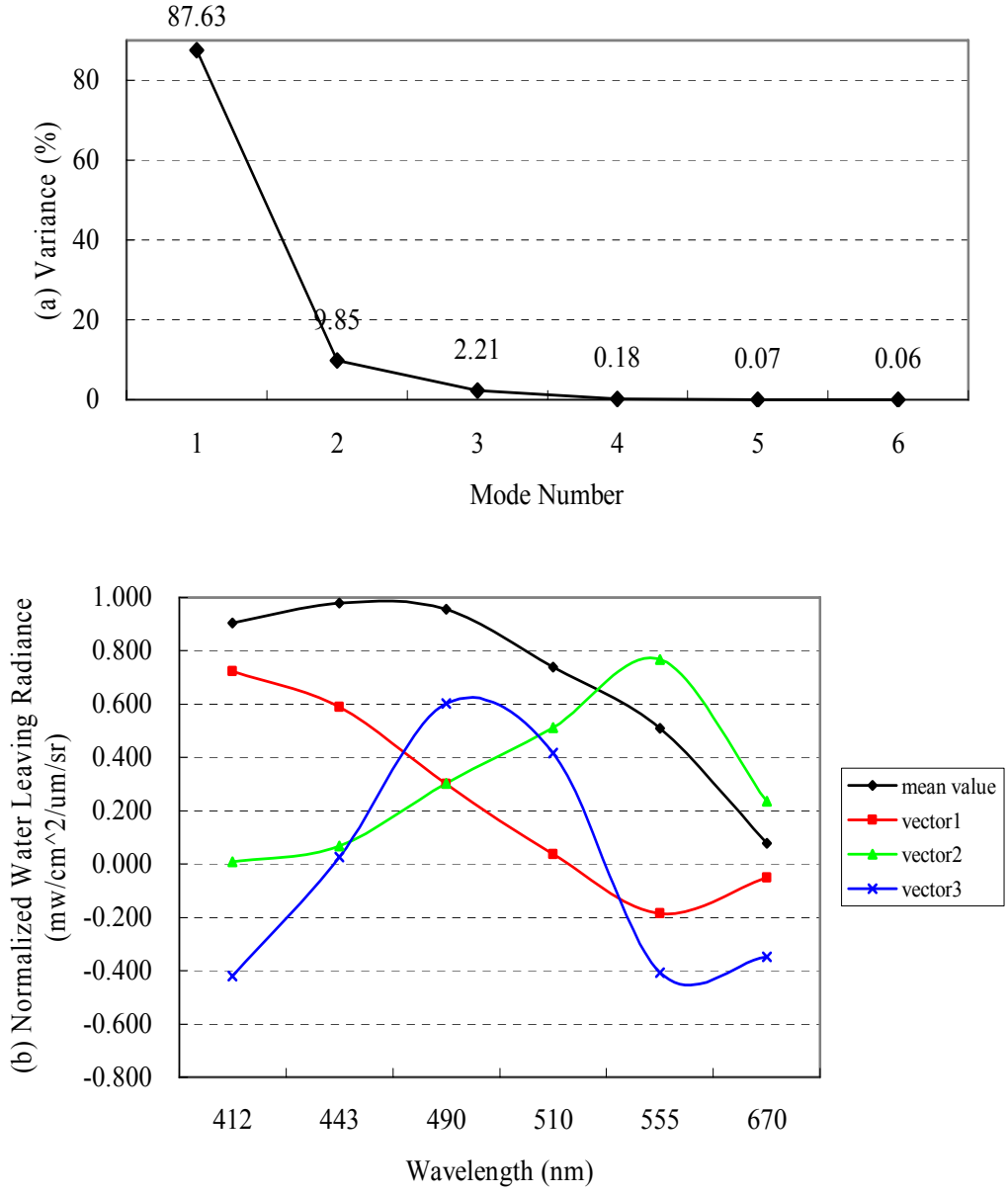

Fig. 3.11. (a) Total variance versus PCA mode and (b) mean spectrum and characteristic spectra eigenvectors derived from NEGOM hydrographic cruises. The eigenvector of the first mode showed that the radiance peak occurred at 412 nm, the second mode at 555 nm, and the third mode at 490 nm. PCA analysis using 526 samples and six visible wavelengths.

According to the spectral response in POC concentrations of various levels (Fig. 3.4b), the first eigenvector was similar to the pattern of lower POC concentration (Case 1 water). Most samples beyond the shelf were from areas of low surface POC concentration. The scattering in the open ocean was primarily the planktonic particles. Longer wavelengths were absorbed by the water more than shorter visible bands. Fig. 3.12 shows the reconstruction of principal components (PC) of the first mode revealing the spatial and temporal variation during NEGOM hydrographic cruises. In the fall, positive PC values were dominant in all the study area, and especially on the outer shelf and the upper slope. In the summer, the spatial pattern of positive values was reduced compared to other seasons.

The second eigenvector was considered to be turbid water (the Case 2 water, higher surface POC concentrations). A radiance peak of the second mode was at 555 nm (Fig. 3.11b). Although the total attenuation summed by the scattering and absorption attenuation is larger in longer visible wavelengths than in shorter visible wavelengths, this band has a small effect on the scattering related to the water and on the absorption related to the particulate and dissolved substances. Therefore, radiance was strongly reflected by the particles present. Although the total attenuation was small at shorter wavelengths, dissolved organic matter dominated absorption at these wavelengths. Therefore, the radiance peak decreased in shorter wavelengths. The positive spatial pattern in the second principal component was well matched with higher POC distributions (Figs. 2.2 and 3.13).

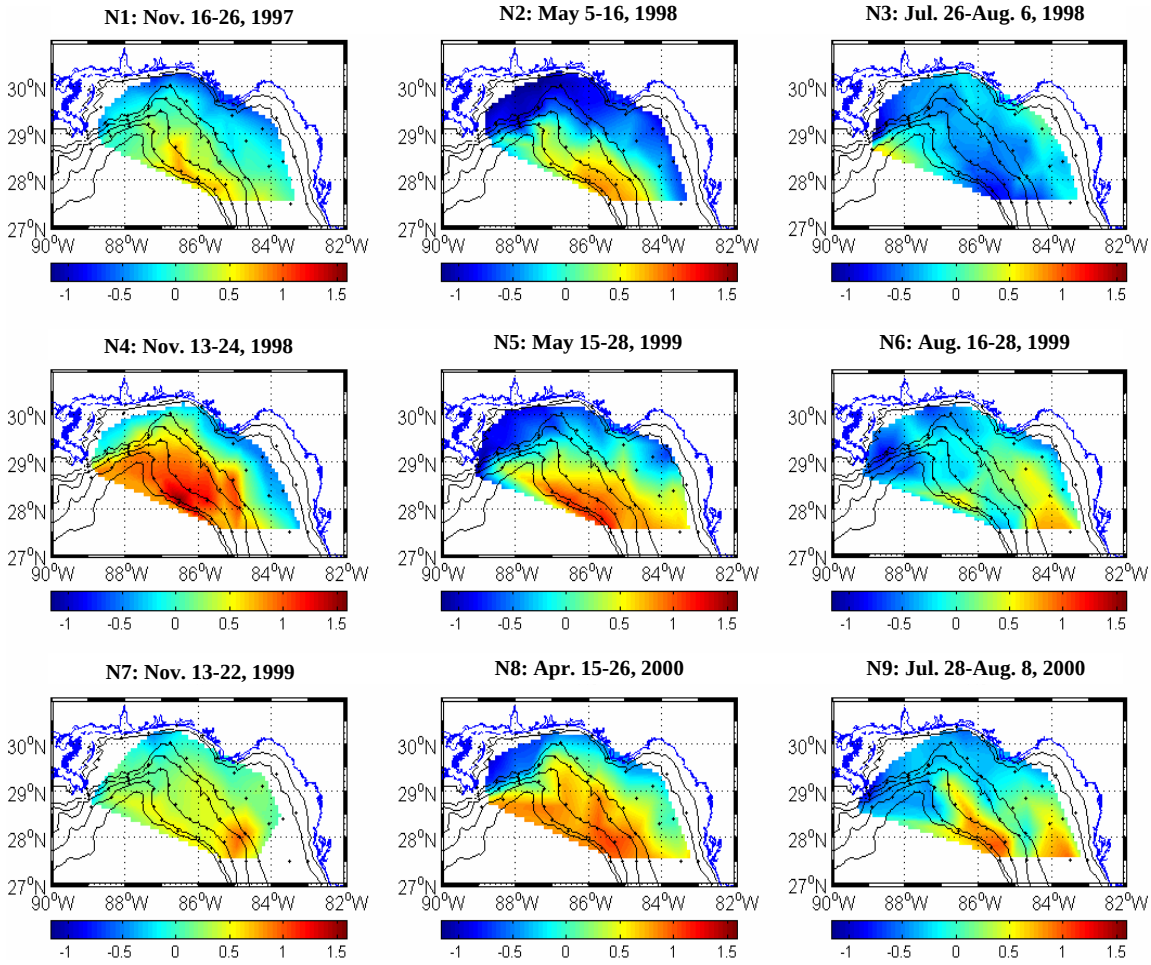

Fig. 3.12. Plots of the first principal component (eigenvalues) from the dimensionally reduced data at stations of NEGOM hydrographic cruises.

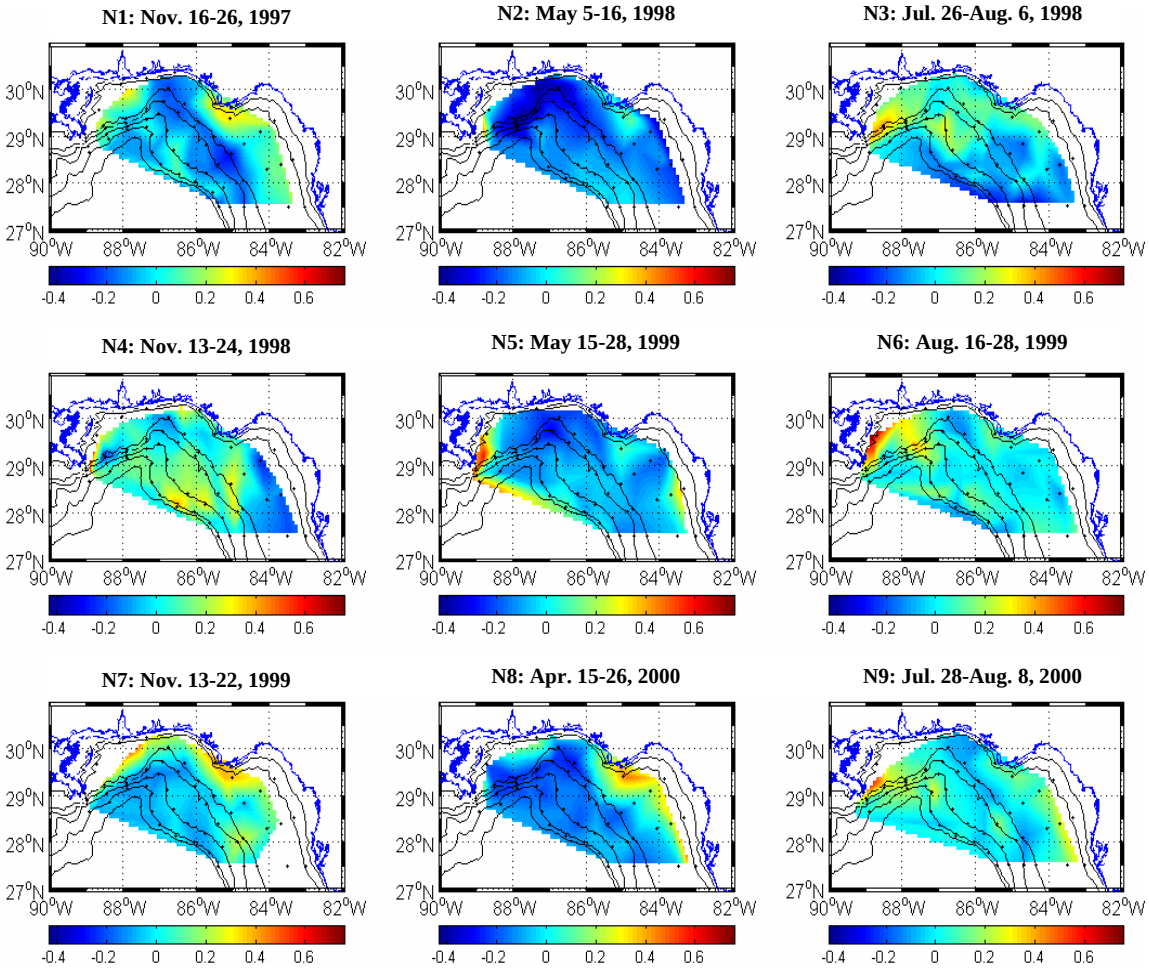

Fig. 3.13. Plots of the second principal component (eigenvalues) from the dimensionally reduced data at stations of NEGOM hydrographic cruises.

In the fall and spring seasons, positive PCs were found on the inner shelf, and isolated structures occurred at the upper slope. In the summer seasons, positive principal components extended out over the upper slope and were widely dispersed in the study area (Fig. 3.13).

The third mode of the eigenvector had a radiance peak at 490 nm (blue visible wavelength, Fig. 3.11b). This pattern presented information about intermediate surface POC concentration compared to the spectral response curve in Fig. 3.4a. This wave-band caused moderate scattering and absorption attenuation in pure water, and then this signal was reflected by the particles having moderate concentrations. Higher positive principal components were found in the Florida area and near Mobile Bay (Fig. 3.14). Lower negative principal components were noted near the Mississippi River. In the fall and spring seasons, highly positive values were found between the Choctawachee and Suwannee River. In the summer seasons, all of the study area had slightly positive principal components except for the Mississippi River Delta.

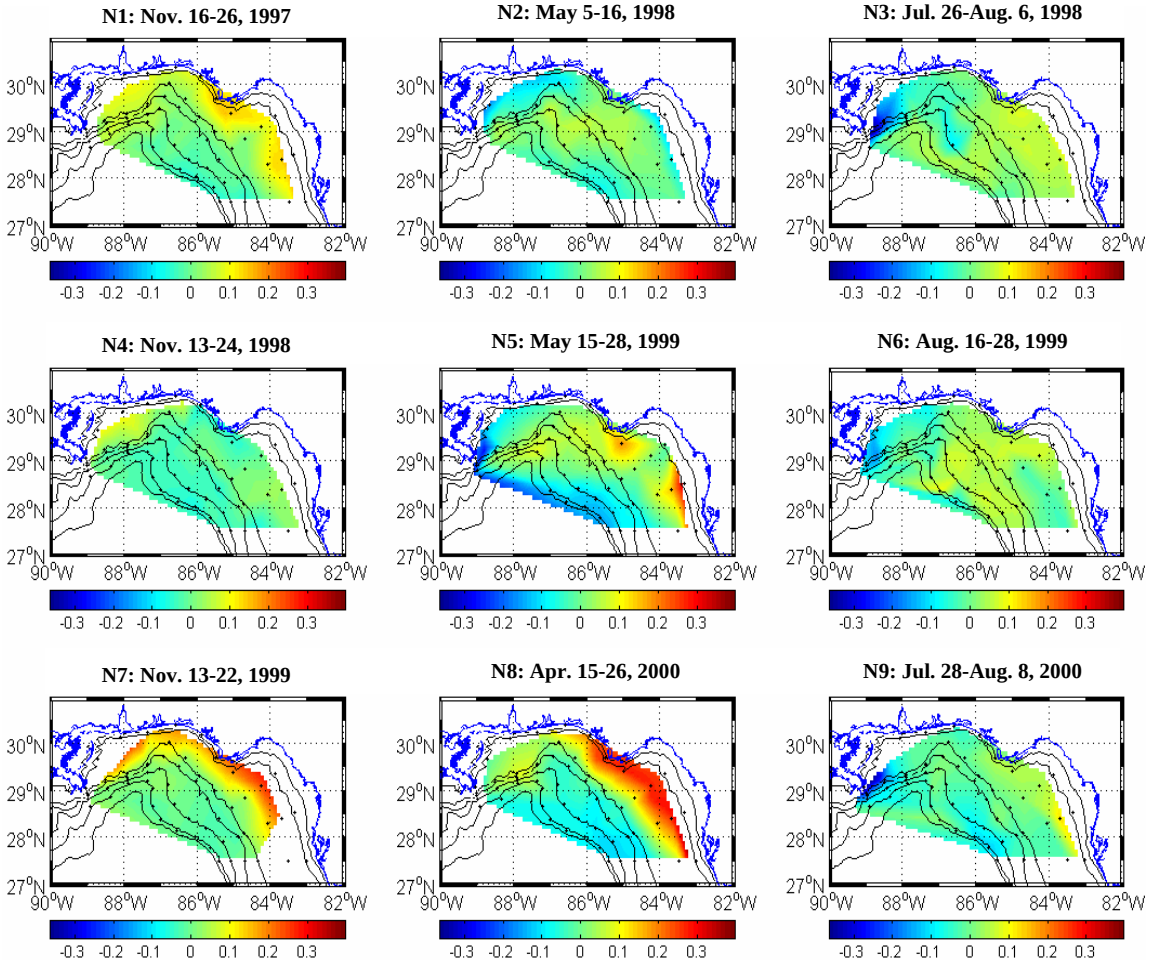

Fig. 3.14. Plots of the third principal component (eigenvalues) from the dimensionally reduced data at stations of NEGOM hydrographic cruises.

A least-squares fit of the PC values to POC concentrations using the multiple-linear regression method determined that POC estimates (mg/m^3) were related to each principal component of the SeaWiFS visible wavelengths by the equation:

$$Y_{[POC]} = -111.1 \times PC_1 + 342.2 \times PC_2 - 535.1 \times PC_3 + 737.2 \times PC_4 - 770.9 \times PC_5 + 98.1 \quad (3\text{-}22)$$

where $Y_{[POC]}$ is POC estimate, and $PC_{1,2,\ldots.5}$ are the principal components of the first, second,…, and fifth mode.

Fig. 3.15 shows the scatter plot between *in situ* surface POC measurements and POC estimates using equation 3-22. This multiple regression had a significant relationship between POC measurements and weighting data of spectral wavelengths with R=0.91 ($R^2 = 0.83$). Although this estimate yielded a pattern similar to that of other empirical algorithms, the RMS error was smaller (Table 3.2).

Fig. 3.16 is the reconstruction of POC estimates based on the PC multiple regression. This predicted value (Figs. 3.15 and 3.16) of POC was well correlated with lower POC standing stocks, but slightly under-estimated at higher POC concentrations compared to Fig. 2.2. However, this result suggested that spectral variations in the modes defined by the first five characteristic vectors may be more closely identified with POC concentration than with other optically important properties of sea water.

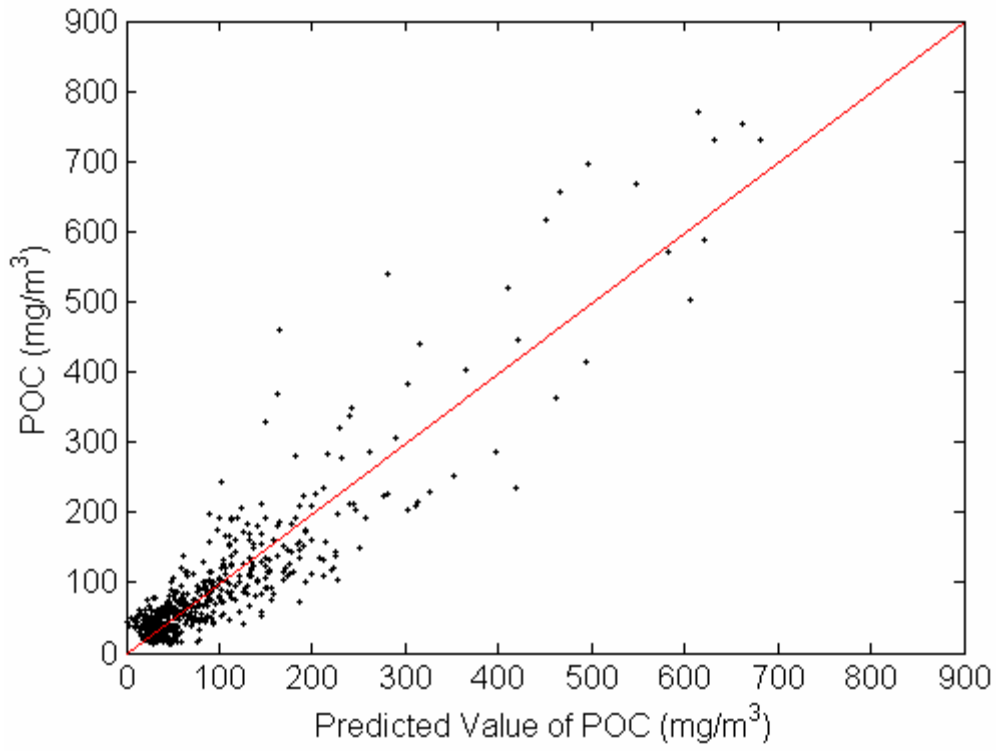

Fig. 3.15. The correlation between POC and predicted POC using PCA method (R=0.912, $Y_{[POC]} = -111.1 \times PC_1 + 342.2 \times PC_2 - 535.1 \times PC_3 + 737.2 \times PC_4 - 770.9 \times PC_5 + 98.1$).

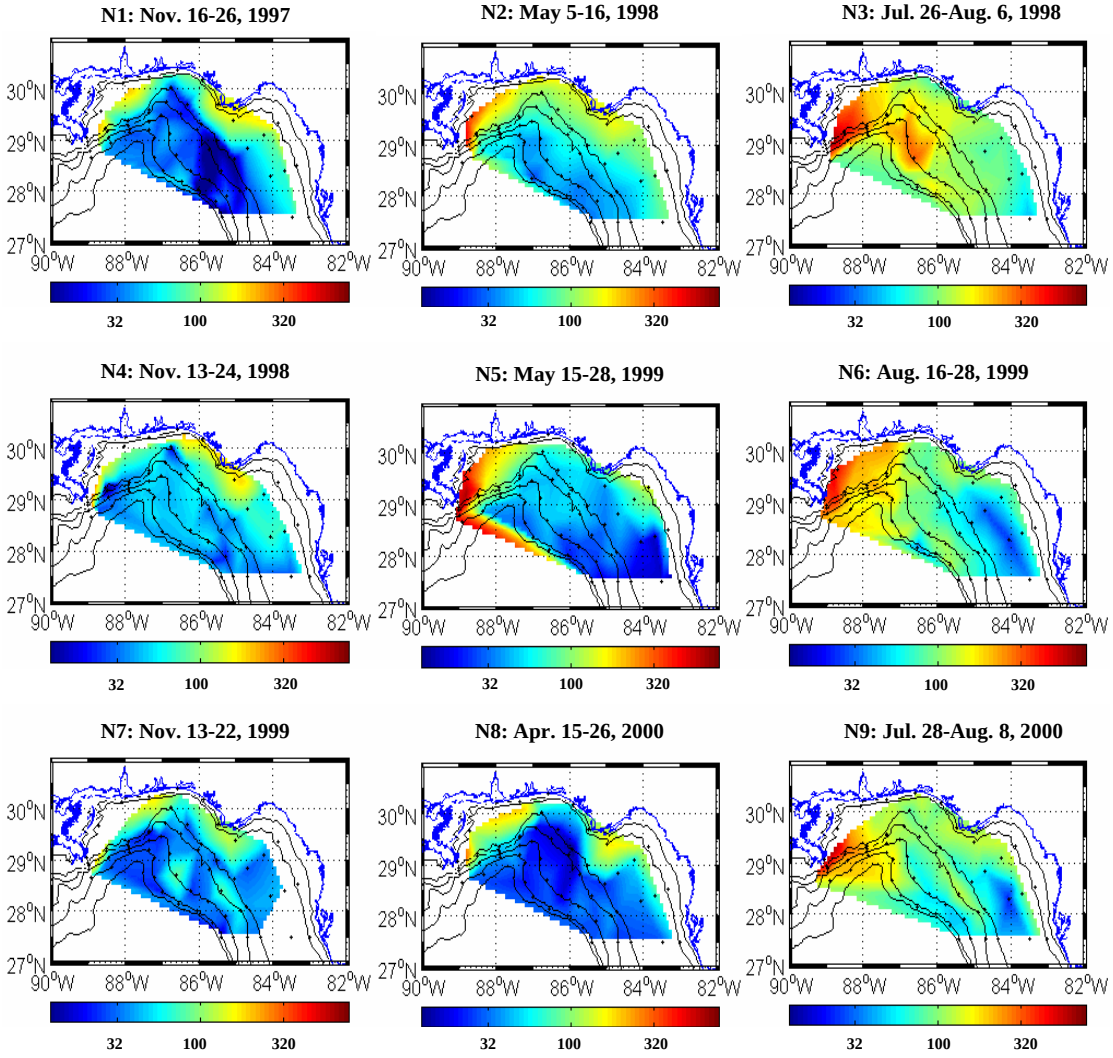

Fig. 3.16. Construction of POC concentration in the Northeastern Gulf of Mexico as determined using six spectral bands of SeaWiFS normalized water leaving radiance. Each cruise map of POC concentration is obtained by the PCA method using the dimensionally reduced data and calculated using equation 3-22.

3.3.5. POC Estimates in Case 2 Waters

For this study, several approaches were used to derive POC estimates from *in situ* POC measurements and sea spectral radiance data from satellites. The general principal approaches in Case 1 water (lower POC concentrations) yielded the optical characteristics of the water constituents, but they failed in Case 2 water (higher POC concentrations). Most natural water bodies contain a variety of organic and inorganic constituents. When natural waters represent a mixture of these materials, one of the most difficult remote sensing problems is to extract quantitative information about each specific constituent from the remotely sensed data.

To solve this problem, two very different approaches were applied in this study. One approach uses empirical POC algorithms based on the SeaWiFS products that could easily be calculated to estimate POC standing stocks. The second approach is a model-based algorithm that was determined from theoretical considerations, and validated by comparison with spectral radiances.

Empirical POC algorithms used the regression method to fit simulated data with power, quadratic polynomial, and cubic functions as did empirical chlorophyll algorithms (O'Reilly et al., 1998). However, these approaches had their limitations. In coastal waters, the presence of suspended sediments and dissolved organic matter creates an optically complex situation. In non-linear conditions, linear regression methods did not transfer well to linear conditions and did not model nonlinear relations well except over small ranges. The nonlinear regression requires a priori knowledge of the nature of the nonlinear behavior, which has not been studied completely.

Although the standard NASA SeaWiFS chlorophyll algorithms typically over- or under-estimate chlorophyll concentration, POC concentrations in this study were moderately correlated with SeaWiFS chlorophyll pigment concentration (Figs. 3.3a and 3.3b). The RMS error was relatively small (Table 3.2)

The single normalized water leaving radiance using 555 nm was better correlated with higher POC concentration than with lower POC values (Fig. 3.6). The blue-to-green ratio (Lwn(510)/Lwn(555)) using Lwn(555) as the normalized factor can greatly reduce the scatter between predicted and sampled data compared to the single Lwn(555), reducing the error especially between the low and moderate POC concentrations (Fig. 3.8). In Fig. 3.9, each result using the blue-to green ratio was similar, but the predicted value of POC concentrations less than 300 mg/m^3 was sensitive to the change of POC concentrations compared to the single blue-to-green algorithm. Although proper use of multiple parameters could allow a better fit, the difference was small.

Simple ratio and maximized simple ratio methods were used to determine the POC concentration using the relationship between peak radiances of spectral response curves (Fig. 3.4a). The correlation using maximized simple ratio had less scatter at lower POC concentrations than using the simple ratio. This maximized simple approach effectively used all blue-green visible radiance and provided information at all wavelengths. However, these empirical POC approaches need a more systematic explanation in a variety of nonlinear conditions.

In model-based approaches, any fixed number of spectral radiances does not give the same number of independent optical parameters because of the similarity of the spectral dependence of different oceanic optical parameters. Therefore, only a small number of spectral measurements yield independent information about interesting water constituents. The degree of interdependence between radiances measured at different wavelengths can be determined with an eigenvalue analysis (Twomey, 1977). Each vector in Fig. 3.11b indicates the possibility of POC estimates from turbid waters. One or a combination of the weighted eigenvalues reduced the noise levels from an optically complex environment. Although this linear approach did not accurately describe the physical relationship between PCs of the spectral radiances and POC concentrations, the results of PCA showed that retrieved signals from full spectral radiance to the first five radiances lost virtually no information from the original constituents.

However, the potential errors of many POC algorithms in this study area also break down in turbid water of the study area. The RMS errors in all approaches increased at higher POC concentrations more than at lower POC measurements. Case 1 water approaches were simply not applicable to Case 2 water. The errors of these algorithms can occur for the following reasons and required consideration of corrected approaches:

1) The signals radiated from the surface water constituents did not exactly match the collected samples from each station, because the averaging method from pixel-by-pixel cannot provide exactly the same conditions of the *in situ* measurements.

2) Due to attenuation by various water constituents in the remotely sensed radiance (or reflectance), we cannot separate or extract the independent information about the signal of water components. Retrieval becomes difficult in waters where the signal from small quantities of data is drowned in the noise from large quantities of non-chlorophyll particles and CDOM. Non-chlorophyll particles are the easiest to recover, while CDOM appears to be the most difficult. This condition can occur especially in turbid waters. It appears that use of data other than the single ratio can greatly reduce the scatter.

3) Sometimes a small number of spectral bands cannot account for non-linear conditions. However, in many algorithms subsets of only two or three channels can be used to estimate oceanographic parameters based on more or less empirical a prior knowledge. One reason for this is that it is complicated to handle imaging spectrometer or hyper-spectral data sets of tens or even hundreds of bands simultaneously to derive object parameters. Therefore a systematic algorithm for the analysis of high dimensional spectral data is needed.

4) The simple statistical approaches (e.g., regression method) cannot calculate the multi-variable conditions of surface waters. We require more than simple adjustments to Case 1 algorithms. To function in Case 2 waters, the algorithms must be able to separate the different water constituents using multispectral, multivariate data. The shape of the spectral response could possibly adjust to optically complex conditions because the characteristic spectrum curves were reflected in the presence of each water constituent.

3.4. Conclusions

POC concentrations from NEGOM data were analyzed to determine temporal and spatial variations in the Northern Gulf of Mexico and to develop estimates of POC based on remote sensing data. Surface POC concentrations and SeaWiFS products had higher values on the inner shelf and near the Mississippi delta, and decreased across the shelf and over the slope.

The two major classical types of algorithms for estimating POC concentrations were empirical and model-based approaches. A large data set including *in situ* measurements and ocean color products were used to estimate POC concentration for validation of algorithms. Simple and successful empirical approaches were presented for deriving POC concentration, using the information from SeaWiFS's chlorophyll, K_{490}, and six visible wavelengths. Empirical POC algorithms used regression methods with power, quadratic polynomial, and cubic functions. Although SeaWiFS products (chlorophyll concentration and K_{490}) were well correlated with temporal and spatial variations of surface POC concentrations, this approach had some limitations in turbid water.

From the study of the spectral response curve, we found that the peak radiance was significantly dependent on POC concentrations or water constituents. Several approaches using this relationship were carried out for POC estimates. The blue-to-green approaches using broad band spectral properties were more sensitive to non-linear conditions than using the single spectral radiance. It appeared that the potential errors

created by a blue-to-green correlation also were reduced. Using wide bands allowed reliable estimates of surface POC concentration over a wide range of concentrations.

A model-based PCA approach was carried out for POC estimates from normalized water leaving radiances. The approach was tested on 6 spectra for which corresponding *in situ* measurements were available. The characteristic eigenvalues and eigenvectors were derived from the reduced dimension of spectral radiances. The results showed that the variability of the radiances could be described for POC estimates in just a few modes. The first three modes explained nearly the entire spectral response of the POC concentration range. The first vector yielded the information about lower POC concentrations. The second vector yielded information about conditions at higher POC concentrations. The third vector yield information about moderate POC concentrations. Other vectors did not yield further information about POC concentrations, because of optically non-linear conditions due to one or more influences of scattering and absorption conditions by suspended matter and CDOM. Correlation between measured and calculated data was significant, and RMS errors also were relatively low.

For this study, the best method for estimating POC was achieved using a PCA algorithm for a narrow spectral range. The result was promising for mapping POC concentration based on remote sensing data. These results were useful to estimate and monitor the POC concentration at regional scales.

CHAPTER IV

CLIMATOLOGICAL VARIABILITY OF SURFACE PARTICULATE ORGANIC CARBON (POC) AND PHYSICAL PROCESSES BASED ON OCEAN COLOR DATA IN THE GULF OF MEXICO

4.1 Introduction

One of the important biogeochemical cycles is the carbon cycle. Many studies have been made to determine ocean carbon dynamics using *in situ* observations and remotely sensed data. The Joint Global Ocean Flux Study (JGOFS) has provided some understanding of the production and export of carbon from the surface ocean to the deep sea floor (Gardner et al., 1995, 1999, 2000, 2003; Chung et al., 1996, 1998; Gundersen et al., 1998; Bishop et al., 1999; Berelson, 2001; Morrison et al., 2001; Doney and Ducklow, in press). To extend global coverage, other studies have been integrated, such as the World Ocean Circulation Experiment (WOCE), South Atlantic Ventilation Experiment (SAVE), North Atlantic Bloom Experiment (NABE), and Bermuda Atlantic Time Series Station (BATS) (Berglund, 1989; Gardner et al., 1990, 1993, 2001; Wood, 1993; Gundersen et al., 1998; Mishonov et al., 2000; DuRand et al., 2001; Gundersen et al., 2001). Still, it is difficult to estimate the amount and distribution of ocean carbon at basin and global scales from ship-based surveys, because it is a very labor and time demanding procedure.

Recently, new ocean color studies have presented biological, ecological and oceanographic information from various water types. Most ocean color studies have

focused on pigment concentrations to predict primary production (Sathyendranath et al., 1989, 1994; Gower et al., 1999; IOCCG, 2000; Behrenfeld and Boss, 2003; Behrenfeld et al., 2005; Carr et al., in press). Phytoplankton plays an important role in the carbon cycle. Phytoplankton concentrations can be indirectly measured by satellite sensors, through the influence of its Inherent Optical Property (IOP) on the spectral signature remitted from the water body. To estimate concentrations, empirical and model-based approaches are used (Mueller, 1976; Gower et al, 1984; Fischer, 1985; Sathyendranath et al., 1989; Neumann et al., 1995; Garver and Siegel, 1997; O'Reilly et al., 1998; Carder et al., 1999; Keiner and Brown, 1999; Schiller and Doerffer, 1999; IOCCG, 2000; Lee et al., 2002; Maritorena et al., 2002). However, observations using standard ocean color algorithms have been used for indirect estimates of ocean color products such as chlorophyll/pigment concentration, primary production, suspended sediment, dissolved/particulate matter, physical dynamic, and its time series data set (Sathyendranath et al., 1989; Doerffer and Fischer, 1994; Strub and James, 2000; Tanaka et al., 2000; Shen et al., 2001; Hu, 2002; Thomas et al., 2003).

With increasing availability of ocean color data, we can determine POC variations with much better temporal and spatial coverage than the very limited data offered by ship observations (Stramski et al., 1999; Loisel et al., 2001; Mishonov et al., 2003; Gardner et al., in press). Time series data of other physical oceanic parameters can provide ancillary data to POC concentrations to determine climatological variations and physical forcing functions. In order to determine the physical processes, ocean observations are carried out by various satellite sensors. Altimetry sensors can determine

ocean circulation and its variability by observing the geostrophic component of ocean circulation. Synthetic aperture radar can delineate current boundaries by surface roughness. Scatterometer sensors can measure wind stress components generated by sea surface currents or waves. Thermal infrared sensors can measure SST and the advection of surface layers by mesoscale circulation (Robinson, 2004).

Routine archives have been used to study time-series patterns of interesting oceanographic parameters. Empirical orthogonal function (EOF) analysis has become standard statistical methods in the meteorology and oceanography (Preisendorfer, 1988; Emery and Thomson, 1997; Kantha and Clayson, 2000; Lee et al., 2003). This has become a particularly useful tool in studying large quantities of multi-variable data (Unal and Ghil, 1995; Lee et al., 2002; Yoder et al., 2002; Fujii and Kamachi, 2003; Thomas et al., 2003; Son, 2005). The eigenfunctions allow us to represent spatial and temporal variability as a number of empirical modes. Because most of the variance in the data can be captured by a small number of modes, their decomposition may be useful for interpreting the variability in various fields.

To identify climatologically important time scales and oceanographic processes, EOF analysis has often been used in satellite imagery. Most EOF studies using ocean color provide the temporal variations with seasonal / inter - annual time scales and the spatial variations to one or more oceanographic processes. EOF analysis also explains physical dynamics based on the signal strength of EOF parameters tested (Kantha and Clayson, 2000; Strub and James, 2000; Thomas et al., 2003; Son, 2005). The dominant signals identify temporal and spatial indices of change in the oceanic environment.

The purpose of this study is to investigate annual and inter-annual variations in temporal and spatial POC estimates based on ocean color data and physical processes, and to evaluate the possible physical forcing functions that affect the temporal and spatial distribution of POC in the Gulf of Mexico.

4.2. Methods

In studying oceanographic fields, the goal of EOF analysis is to provide a compact description of the spatial and temporal variability of data series in terms of orthogonal functions or statistical modes. Each empirical mode is formed by a space pattern and a time series that are derived from an eigenvalue and eigenvector of the covariance (or correlation) matrix (Preisendorfer, 1988; Emery and Thomson, 1997).

In order to detect temporal and spatial patterns of a large ocean color data set in the Gulf of Mexico, EOF analysis was calculated with a monthly time-series data of POC estimates, SST, SSHA, SSW, and PR data during 88 months (September 1997 to December 2004). The original multi-variable data set had two spatial dimensions (longitude and latitude in a monthly image) and one temporal dimension (88 monthly images). The monthly data set was arranged into a two-dimensional array $T(t_m, x_n)$, where M is the number of elements in the temporal dimension, in this case the number of monthly images, and N is the number of elements in the spatial dimension, in this case the number of pixels in an image.

$$T_{mn} = \begin{bmatrix} x_{11} x_{12} \ldots\ldots\ldots\ldots x_{1n} \\ x_{21} x_{22} \ldots\ldots\ldots\ldots x_{2n} \\ . \\ . \\ x_{m1} x_{m2} \ldots\ldots\ldots\ldots x_{mn} \end{bmatrix} \quad \begin{matrix} \text{A map for time n} \\ \\ \\ \\ \text{A time series for location m} \end{matrix} \tag{4-1}$$

where each matrix row contains all pixels from a monthly image strung together continuously and each column is a time series of observations at a given location (pixel) during 88 months.

Paden et al. (1991) suggested that removing each mean value from the temporal and spatial dimension of the data matrix before EOF analysis provided more detailed information from EOF analysis. Since the removal of the temporal and spatial mean values revealed patterns that varied strongly in time and space, i.e. the variations from the mean.

Therefore, from the data matrix, $T(t_m, x_n)$, we first removed the record mean μ from each column (temporal dimension) and row (spatial dimension). Second, we normalized the demeaned time series by dividing each column by its standard deviation σ. This approach ensured that no data points in the time series were dominated by the variance, but all data were given an equal opportunity to contribute in the analysis. The resulting demeaned and normalized series F(t, x) were termed standardized series.

$$F_{temp}(t,x) = \left(\frac{T_x(t) - \mu_{temp}}{\sigma_{temp}} \right) \quad \text{and} \quad F_{spat}(t,x) = \left(\frac{T_t(x) - \mu_{spat}}{\sigma_{spat}} \right) \tag{4-2}$$

$$\mu_{temp} = \frac{1}{N} \sum_{t=1}^{m} T_x(t) \qquad \text{and} \quad \mu_{spat} = \frac{1}{N} \sum_{x=1}^{n} T_t(x) \tag{4-3}$$

$$\sigma_{temp} = \sqrt{\frac{1}{N-1} \sum_{t=1}^{m} \mu_{temp}(t)^2} \quad \text{and} \quad \sigma_{spat} = \sqrt{\frac{1}{N-1} \sum_{x=1}^{n} \mu_{spat}(x)^2} \tag{4-4}$$

where μ(t, x) was the record mean, and σ(t, x) was the standard deviation. The normalization was especially relevant when analyzing two or more fields to ensure no dominance of one field over the others.

In order to make EOF analyses, we used a singular value decomposition (SVD) approach rather than covariance (correlation) matrix approach. SVD provided a one-step method for computing all the components of the eigenvalue problem, without having to compute and store large covariance matrices. The resulting decomposition was computationally more stable and robust (Bretherton et al., 1992; Wallace et al., 1992).

The SVD of a matrix was based on the concept that any rectangular M × N matrix F(t, x) was written as the product of three matrices: an N × N matrix U, an M × N diagonal matrix Γ with positive or zero elements, and the transpose ($V^{\dagger}$) of an N × N matrix V.

$$F_{temp} = U_{temp} \times \Gamma_{temp} \times V_{temp}^{\dagger} \quad \text{and} \quad F_{spat} = U_{spat} \times \Gamma_{spat} \times V_{spat}^{\dagger} \tag{4-5}$$

Matrix U contained the eigenvectors, and $\Gamma \times V^{\dagger}$ was their amplitude. Matrix Γ was a diagonal matrix corresponding to the *k*th EOF modes. We denoted γ_k as the singular values. The principal component (PC) of the *k*th EOF is given by the time series A^k.

$$A_{temp}{}^{k} = F_{temp} \times U_{temp}{}^{\dagger k} \qquad \text{and} \qquad A_{spat}{}^{k} = F_{spat} \times U_{spat}{}^{\dagger k} \tag{4-6}$$

Each eigenvalue γ_k was proportional to the percentage of the variance of the field F that is accounted for by mode *k*.

$$\%\ \text{temporal variance in mode k} = \frac{{}_{temp}\gamma_k^{\,2}}{\sum {}_{temp}\gamma_i^{\,2}} \times 100 \quad \text{and} \tag{4-7}$$

$$\%\ \text{spatial variance in mode k} = \frac{{}_{spat}\gamma_k^{\,2}}{\sum {}_{spat}\gamma_i^{\,2}} \times 100 \tag{4-8}$$

The EOF spatial pattern was dimensionless and represented the amplitude of a typical event when the PCs were ±1 (von Storch and Zwiers, 1999).

The coupled fields of SVD (combined EOF (CEOF) analysis) allowed for the identification of a pair of EOF patterns and PCs which accounted for a fraction of the covariance between two variables analyzed jointly. After preparing the two datasets of variables *X* and *Y*, we organized the time series of each of the two variables separately in two data matrices. We thus obtained an $M \times N_X$ data matrix *X* and an $M \times N_Y$ data matrix *Y*. The spatial dimensions of the two variables, N_X and N_Y, need not be the same, but all time series had the same number of time steps, *M*.

We then constructed the cross-covariance matrix between time series of *X* and *Y* as $R_{XY} = X \times Y^{\dagger}$. Since we were again comparing two fields, removal of the temporal mean value and normalization of the two variables as explained above was also applied to this marix.

$$R_{XY} = U \times \Gamma \times V^{\dagger} \tag{4-9}$$

Matrix U was the eigenvectors of *X*, and V was the eigenvectors of *Y*. Matrix Γ was the diagonal matrix corresponding to the *k*th EOF modes. The PCs of fields *X* and *Y* are obtained for each field.

$$\text{Field X} = \Sigma\, U^{k} \times X_{m}(t) \qquad \text{and} \qquad \text{Field Y} = \Sigma\, V^{k} \times Y_{m}(t) \tag{4-10}$$

Each eigenvalue γ_k derived from diagonal matrix Γ was proportional to the squared covariance fraction between *X* and *Y* accounted for by mode *k*, such that:

$$\%\ \text{squared covariance mode k} = \frac{\gamma_k^{\,2}}{\sum \gamma_i^{\,2}} \times 100 \tag{4-11}$$

Each SVD mode of covariability between *X* and *Y* was determined by a pair of spatial patterns (one for each field). A pair of PCs showed how the respective spatial patterns evolve in time. Variance indicated how much of the squared covariance between the two fields was accounted for by the mode. The correlation coefficient between the two PCs of mode *k*, provided a measure of how strongly field *X* and *Y* were related to one another through mode *k*.

4.3 Results

4.3.1. Monthly Mean Values

The climatological monthly mean (September 1997-December 2004) of surface POC estimates based on a principal component analysis (PCA) algorithm using SeaWiFS spectral radiance data were used to create distribution maps for the Gulf of Mexico (Fig. 4.1). The highest POC values were consistently on the inner shelf, diminishing offshore.

The monthly mean of SST derived from NOAA AVHRR images for the period of September 1997 to December 2004 showed a north-south gradient, approximately parallel to the coast, with temperature diminishing northward (Fig. 4.2). Satellite SST measures only the skin of the ocean. Winter SST had a definite regional signature and wide range (February SST ranged from 15°C to 26°C), while summer SST was more uniform and warmer (August mean SST was 29°C). Cold surface water was constrained to the inner shelf of the northern Gulf of Mexico, generated by surface cooling, coastal upwelling, and runoff along the coast. Inflow of the warm Loop Current was best observed during winter month, although the flow presented year round.

The monthly mean of dynamic SSHA archived from TOPEX/POSEIDON and Jason-1 altimeters for September 1997 to December 2004 showed mesoscale circulation patterns in the Gulf of Mexico (Fig. 4.3). The monthly mean values do not adequately explain the description of either their continued evolution or motion. Cyclonic and anticyclonic eddies that are shed periodically from the Loop Current show a chaotic distribution.

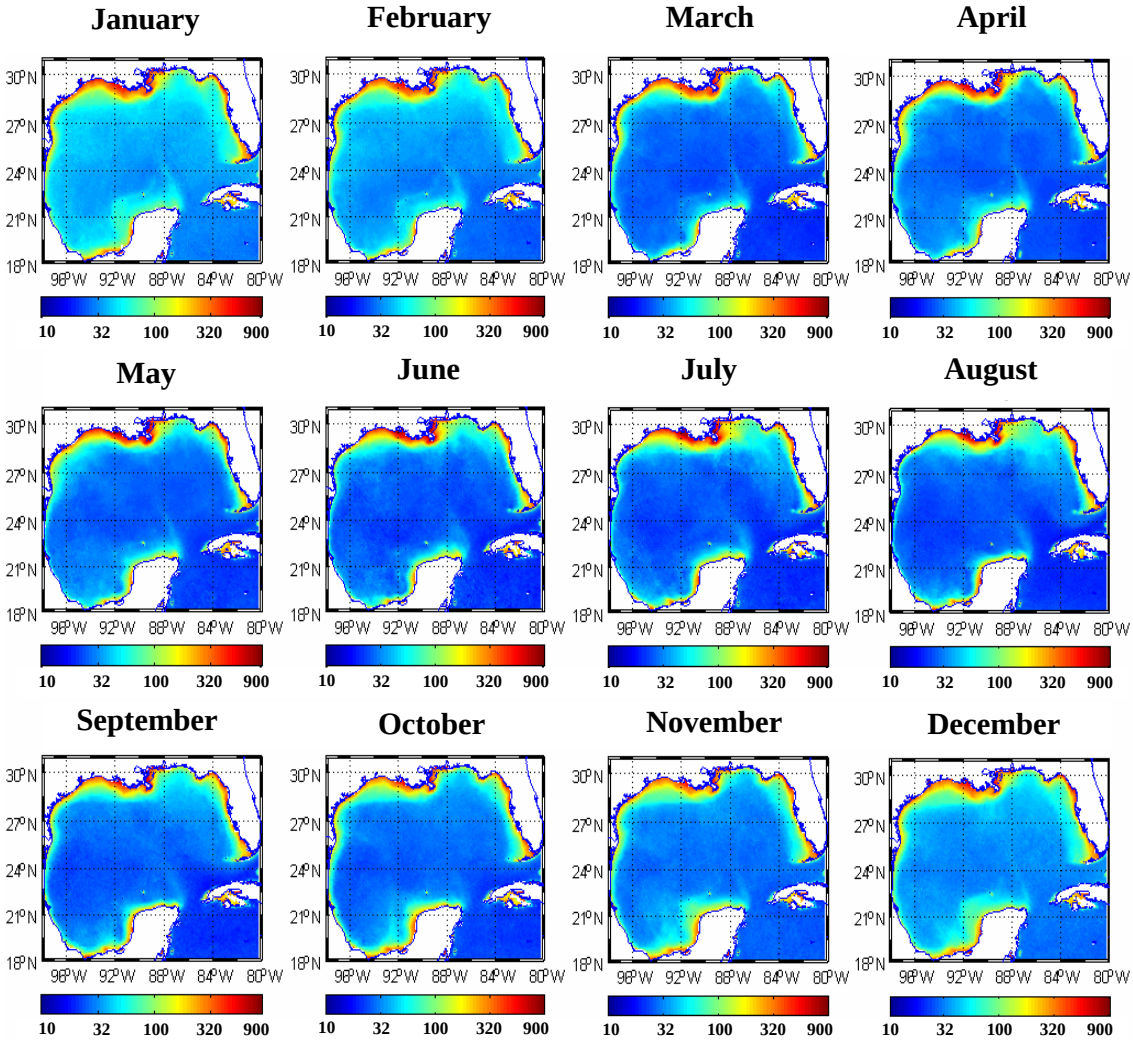

Fig. 4.1. Climatological monthly mean of particulate organic carbon (POC, mg/m^3) based on SeaWiFS radiance data in the Gulf of Mexico (September 1997 – December 2004). The algorithm used to estimate POC for these maps was based on equation 3-22.

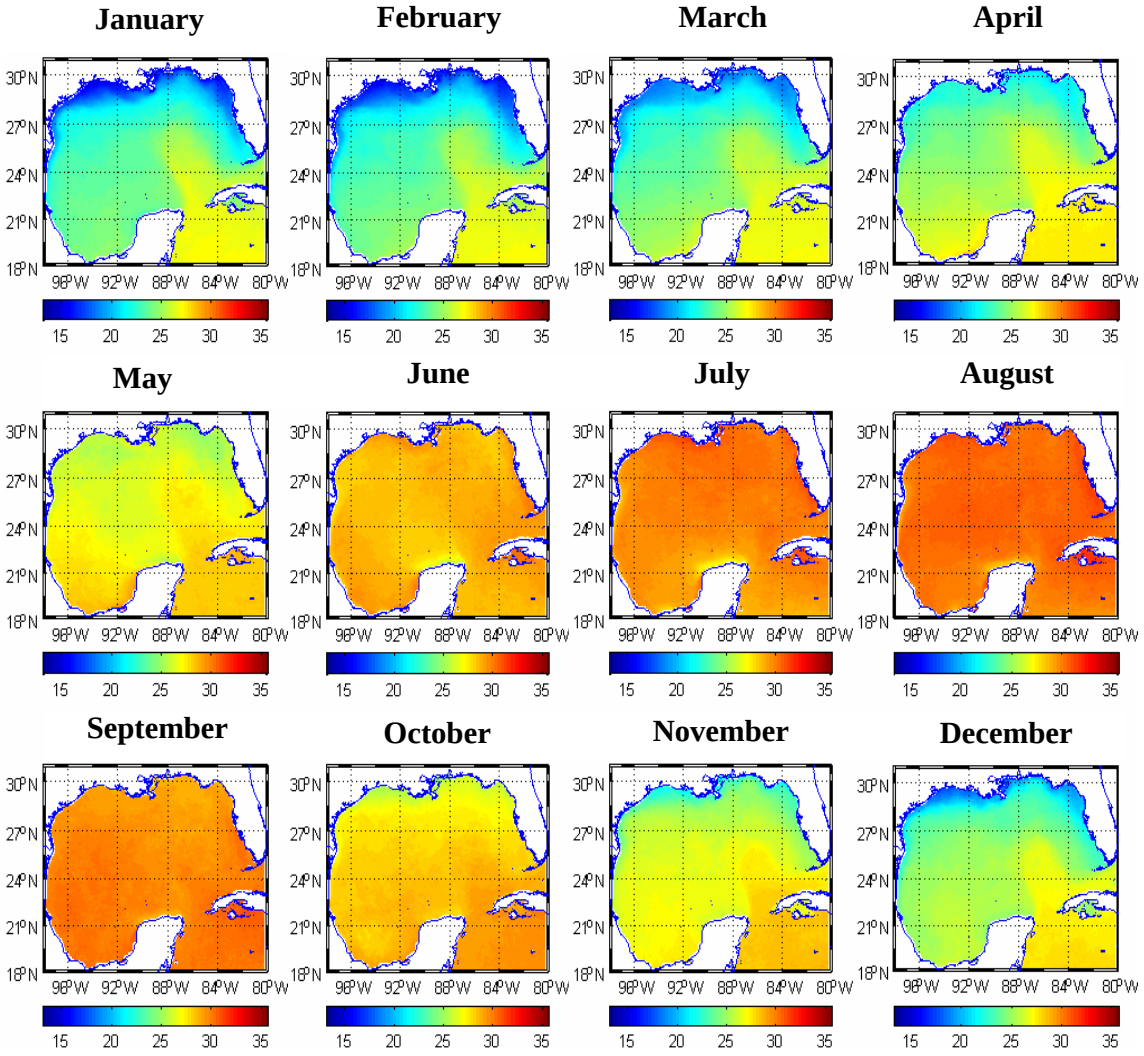

Fig. 4.2. Climatological monthly mean of sea surface temperature (SST, °C) from AVHRR NOAA radiometer data in the Gulf of Mexico (September 1997 – December 2004).

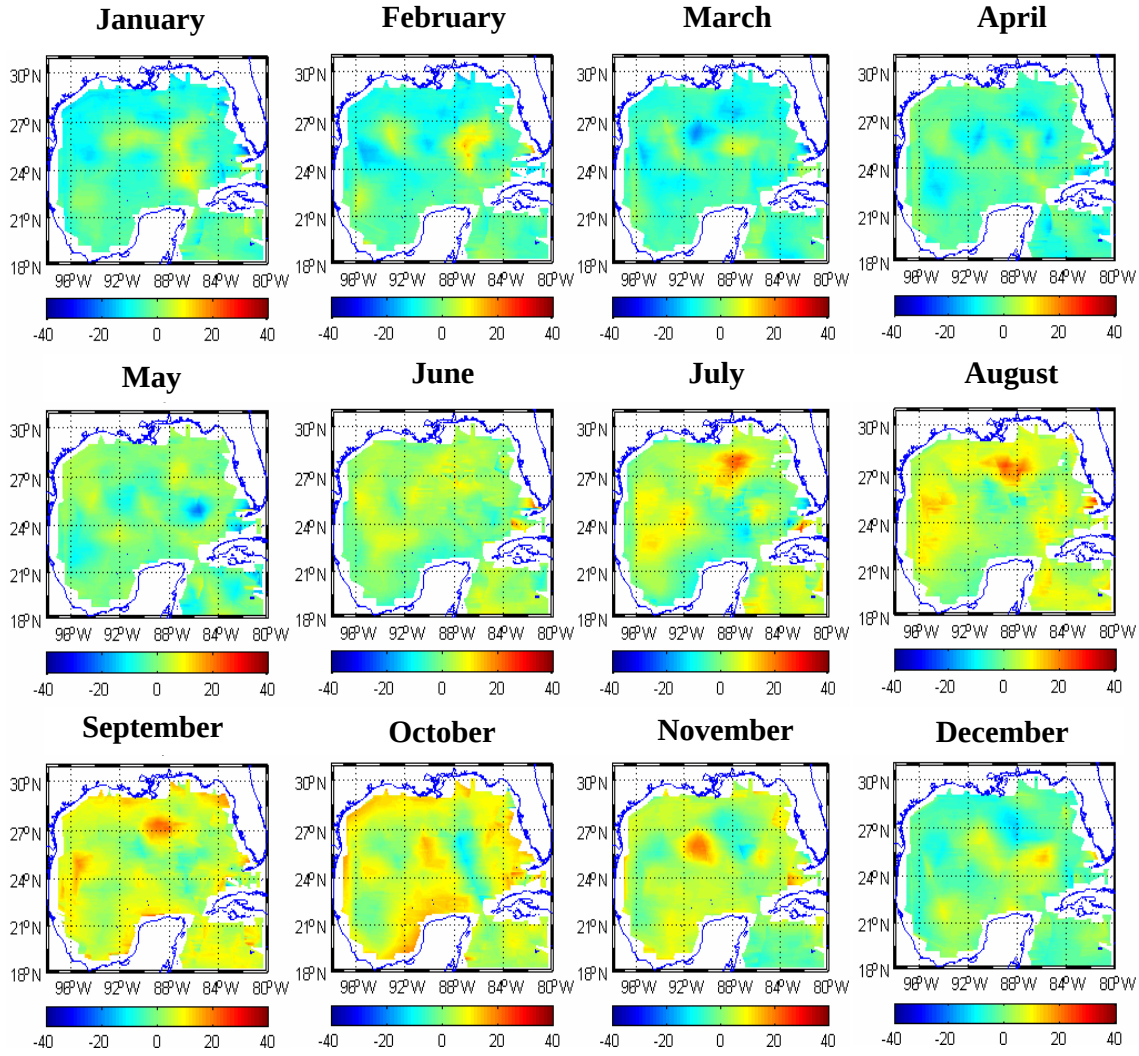

Fig. 4.3. Climatological monthly mean of sea surface height anomaly (SSHA, cm) from TOPEX/POSEDON and Jason-1 altimeter data in the Gulf of Mexico (September 1997 – December 2004).

The monthly mean of SSW derived from QuickScat and SSM/I scatterometers for September 1997 to December 2004 showed much lower winds in summer than winter (Fig. 4.4). In spring (March to May), a west wind prevailed in the central Gulf of Mexico, and the northwest-southwest wind dominated in the northern Gulf of Mexico. During summer (June to August), winds were weak in the Gulf of Mexico and westward in the central Gulf of Mexico and north-northeast in the northern Gulf. During fall (September to November), winds increased and shifted to the southwest in the northern Gulf of Mexico. During winter (December to February), a south-southwest wind dominated in the Gulf of Mexico.

Monthly PR based on SSM/I scatterometer satellite data for September 1997 to December 2004 showed that rainfall was focused on the northeastern Gulf of Mexico from January to April. Rain was heaviest through the Gulf in September, tapered in October, and was fairly uniform, but moderate in November and December. White areas indicate less than 0.001 (mm/hr) precipitations (Fig. 4.5).

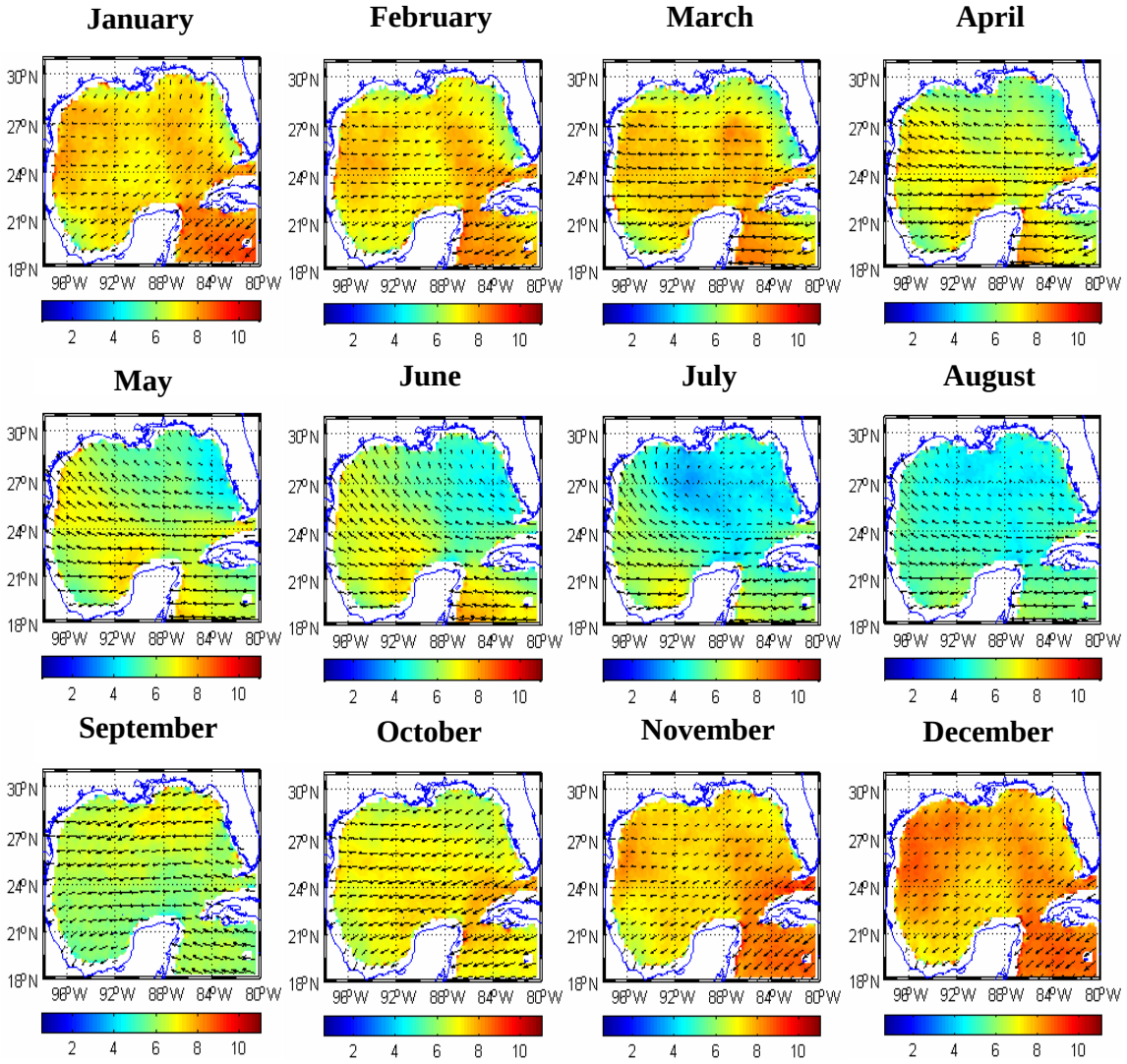

Fig. 4.4. Climatological monthly mean of sea surface wind (SSW, m/sec) from QuickScat and SSM/I scatterometer data in the Gulf of Mexico (September 1997 – December 2004).

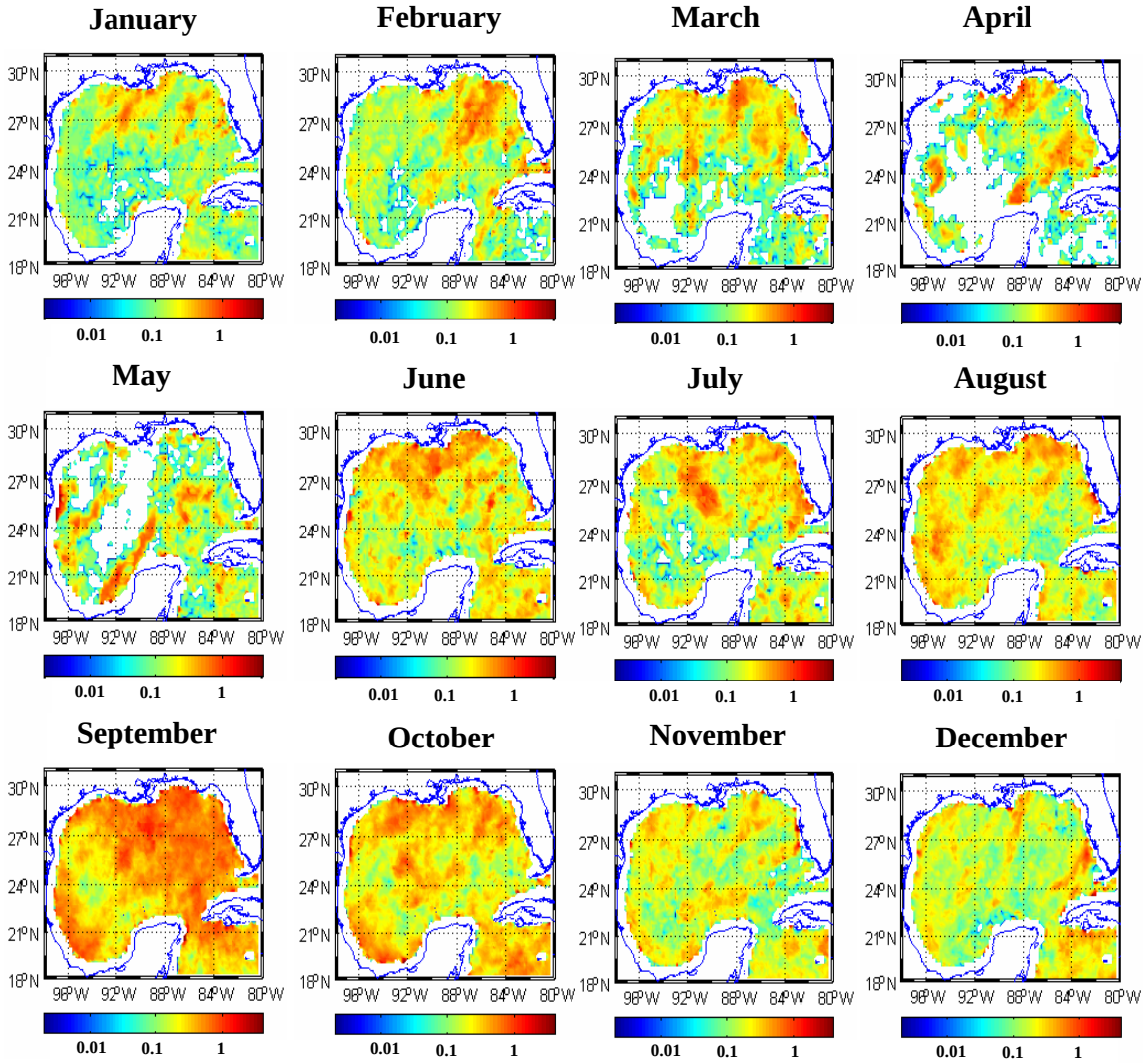

Fig. 4.5. Climatological monthly mean of precipitation rate (PR, mm/hr) from SSM/I scatterometer data in the Gulf of Mexico (September 1997 – December 2004). White areas indicate <0.001 mm/hr precipitation.

4.3.2. Single EOF Analysis –Spatial and Temporal Variations

Each EOF unit was interpreted considering amplitude and spatial patterns as a unit of information. A given EOF pattern described a spatial pattern of residual variance, which was modulated by its corresponding time-varying amplitude. This provided spatial and temporal patterns and elucidated the relationship between POC concentrations and physical processes in the Gulf of Mexico.

The POC eigenvalues for the spatial and temporal variance EOFs are graphically shown in Fig. 4.6a. The first and second modes in the temporal variances accounted for approximately 58% and 36% of the total variance, respectively with a very steep drop off in variance for the next few modes (Fig. 4.6a). If the first three modes were summed to reconstruct the most coherent part of the POC variability, they accounted for 97% of the total monthly POC variance. Dominant modes represented the spatial and temporal variability of 1997-2004 POC concentrations in the study area.

The first temporal mode of POC represents 58% of the total variance (Fig. 4.6a). The spatial pattern of the first temporal mode shows strong positive values along the inner shelf and near the Mississippi River in the northeastern Gulf of Mexico. Negative values are found in the southwestern Gulf of Mexico (Fig. 4.7a). A positive eigenvector indicates POC concentration above the mean for the time-series. Positive POC values in the time series of the first temporal mode were observed for most of 1998 and 2003-2004. Periods of negative anomalies occurred in 2000-2002. Values fluctuated in 1999 (Fig. 4.7d). This time-series pattern was related to a non-seasonal cycle.

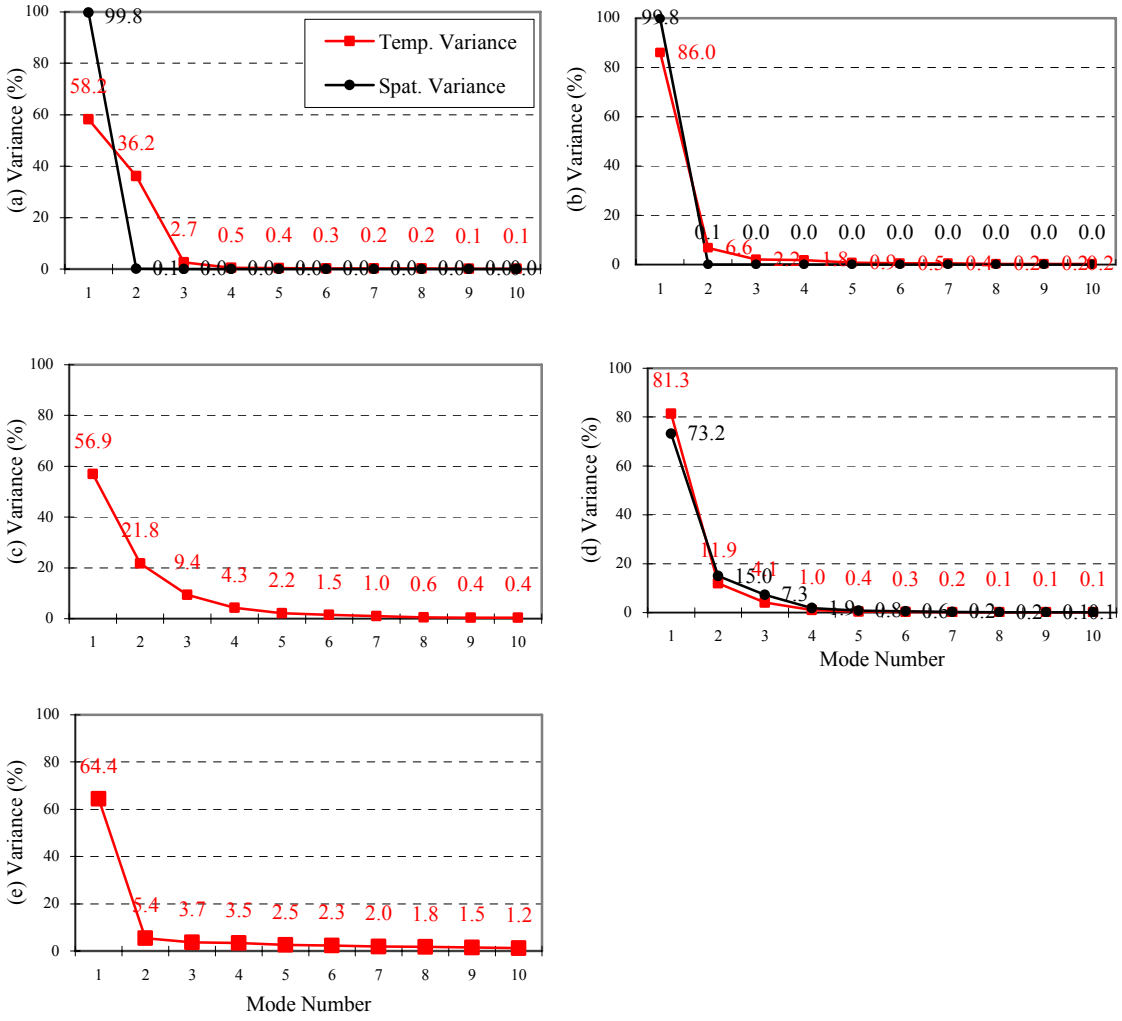

Fig. 4.6. EOF eigenvalues of monthly (a) POC, (b) SST, (c) SSHA, (d) SSW, and (e) PR for temporal variance (red line) and spatial variance (black line).

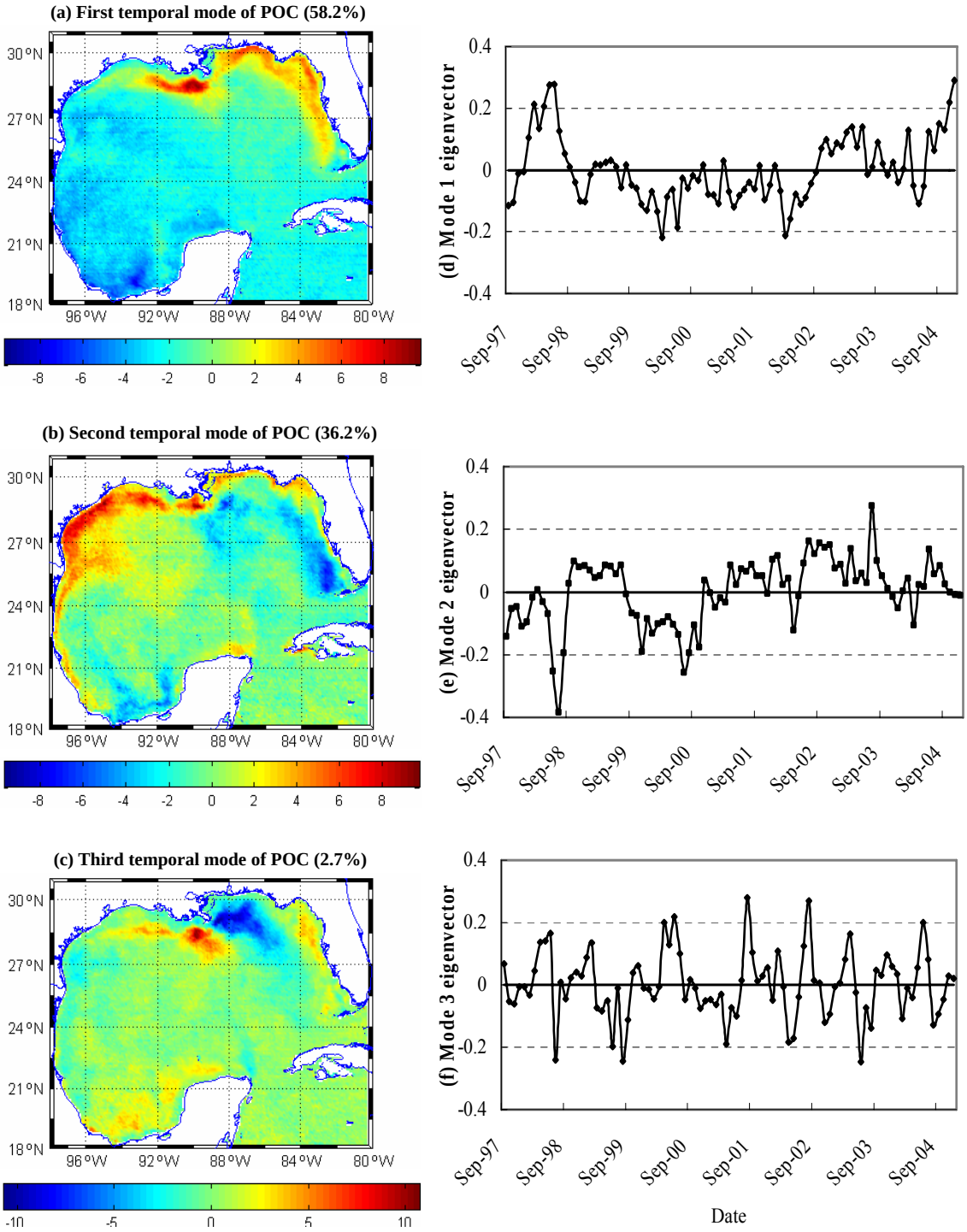

Fig. 4.7. Temporal modes of POC for EOF patterns (left) and their time series (right) in the Gulf of Mexico.

The power spectrum shows that the first temporal mode had two strong peaks at frequencies of 30 and 15 months. The rest of the frequency was mostly constant and had a small peak at 5 and 11 months (Fig. 4.8a).

The second temporal mode of POC explains 36% of the total variance (Fig. 4.6a). The spatial pattern of the second temporal mode exhibited an east-west trend (Fig. 4.7b). Positive POC vales in time series of the second temporal mode were observed for 1999 and 2001-2004, and negative values for 1997-1998 and 2000 (Fig. 4.7e). The power spectrum provides that a strong peak was at a period of 22 months, and small peaks at periods of 6, 8, and 11 months (Fig. 4.8b).

The third temporal mode of POC is about 3% of the total variance (Fig. 4.6a). The spatial pattern of the third temporal mode shows both positive and negative variance near the Mississippi River Delta (Fig. 4.7c). Positive values were observed on the west pass of the Mississippi Delta and negative value in the east pass of the Mississippi Delta (Figs. 4.7c and 4.7f). The power spectrum shows that time series of the third temporal mode had a strong peak at 7 and 8 months and weak inter-annual cycles (15 and 22 months, Fig. 4.8c).

The first spatial mode of POC has a dominant annual component and a weak semi-annual period (99% of total variance), with a maximum in Jun-July and a minimum in October-November (Figs. 4.8d and 4.9). It was the only statistically significant mode. The second and third spatial modes of POC explain about 0.1% of the total variance (Fig. 4.6a).

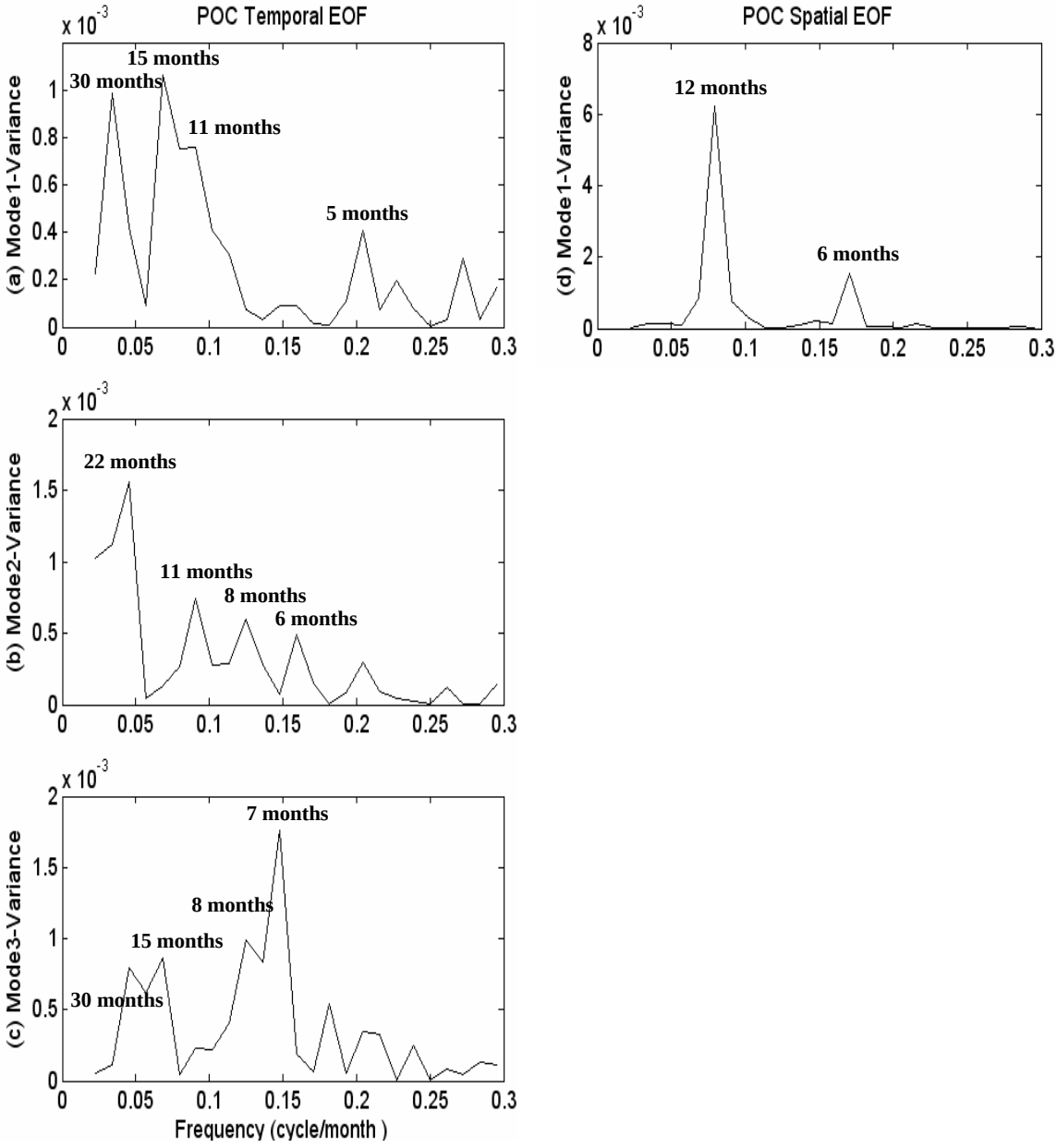

Fig. 4.8. Power spectra of time series in POC temporal and spatial modes of Figs. 4.7 and 4.9.

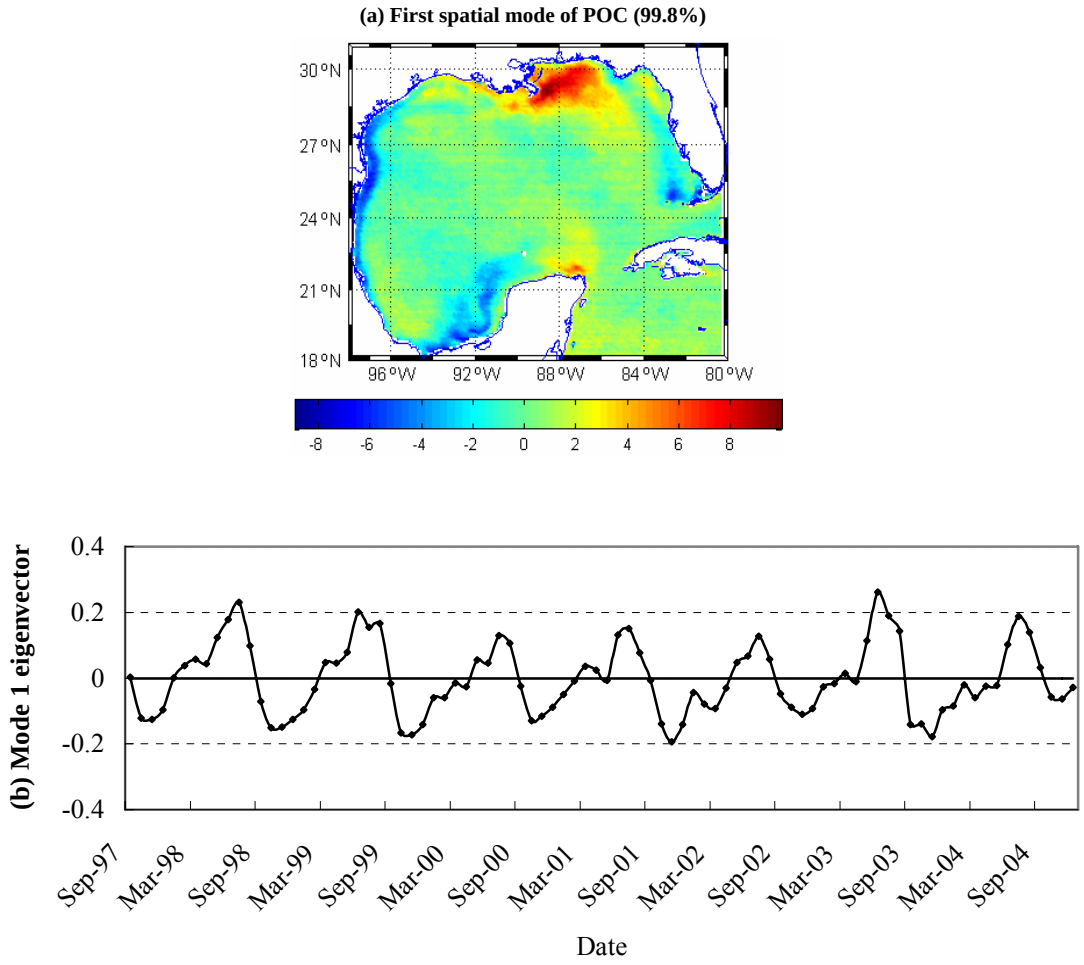

Fig. 4.9. First spatial mode of POC for EOF pattern (a) and its time series (b) in the Gulf of Mexico.

Fig. 4.6b shows the SST eigenvalues for the temporal and spatial variances. The first temporal mode of SST accounts for 86% of the sea surface temperature variability. The spatial pattern of the first temporal mode shows strong positive values along the warm water of the Loop Current. Negative values of SST are related to the relatively cold water inshore in the northern Gulf of Mexico and western Florida. This spatial pattern represents the interactions between warm and cold water in inshore of the northern Gulf of Mexico (Fig. 4.10a). Positive SST values in the time series of the first temporal mode were observed for 1997-1998 and 2001 and negative values for both 1999 and 2002 years. Values fluctuated in 2000 and 2003-2004 (Fig. 4.10d). The first temporal mode had non-seasonal components at 18 and 30 months and seasonal components at 6 and 11 months (Fig. 4.11a).

Although the second and third temporal modes of SST account for only 7% and 2% of the total variance (Fig. 4.6b), they appeared to modulate the seasonal cycle seen as the first mode in a meaningful manner.

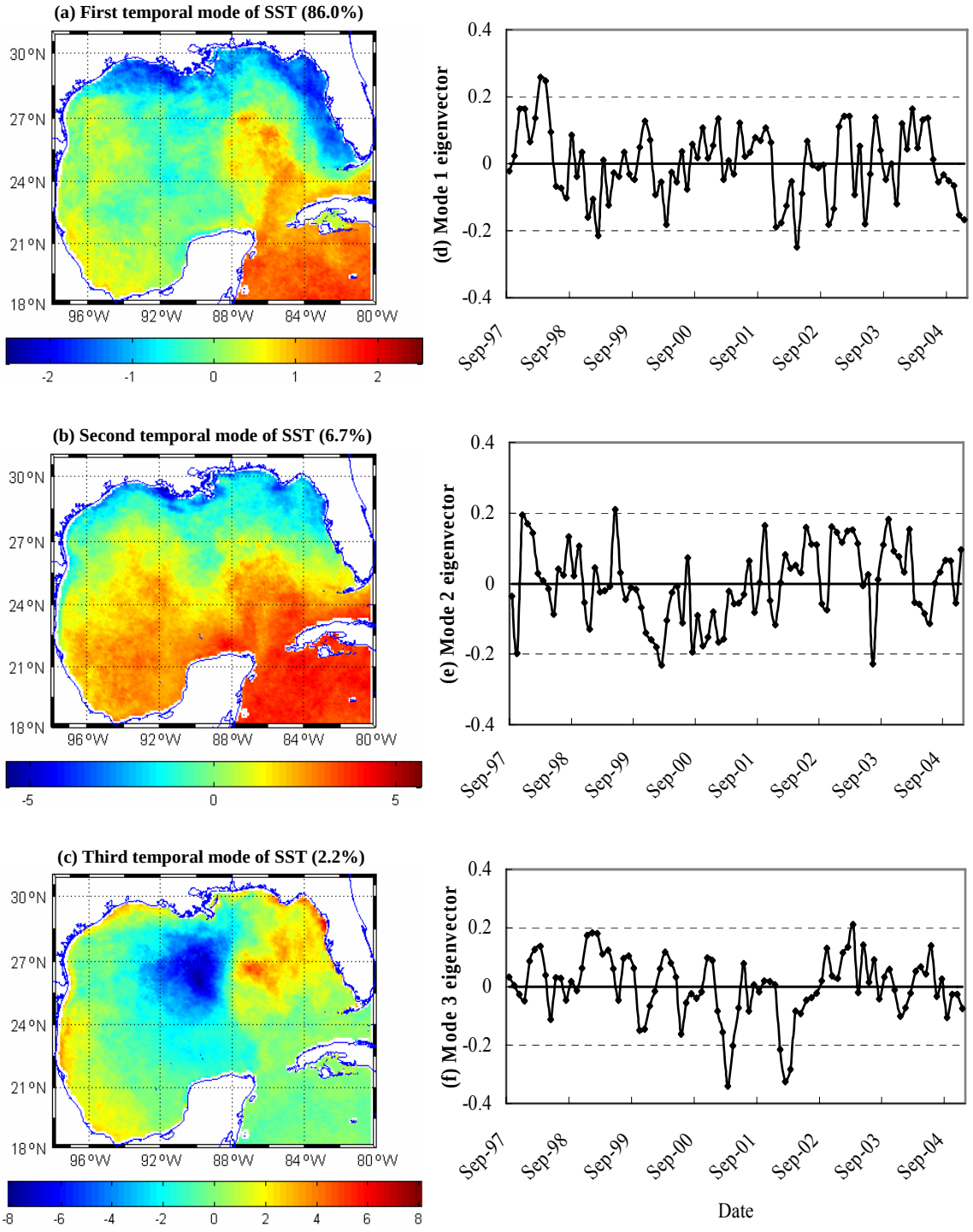

Fig. 4.10. Temporal modes of SST for EOF patterns (left) and their time series (right) in the Gulf of Mexico.

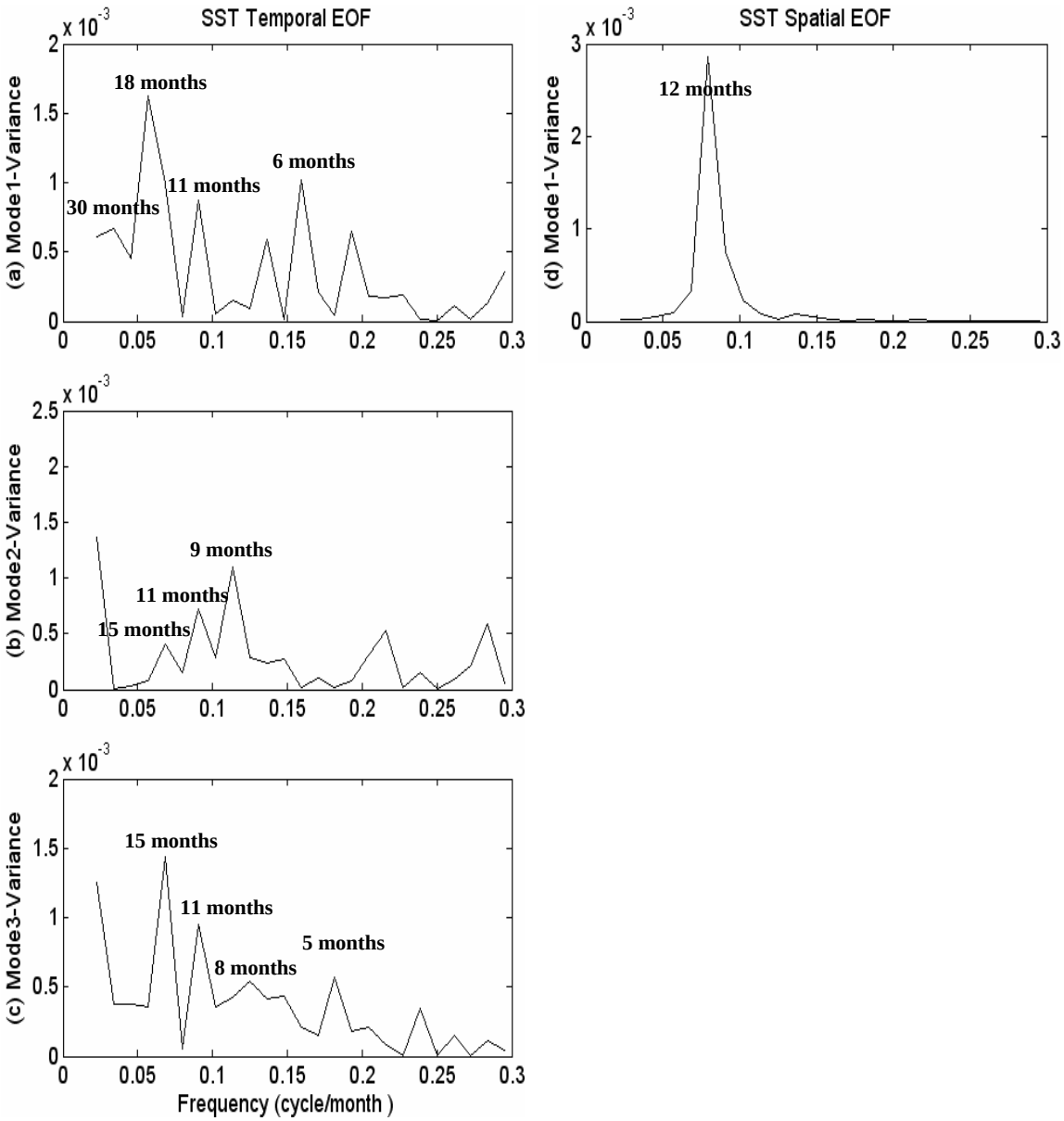

Fig. 4.11. Power spectra of time series in SST temporal and spatial modes of Figs. 4.10 and 4.12.

The second temporal mode of SST also shows the north-south temperature gradient (Fig. 4.10b). The spatial pattern in the third temporal mode of SST shows the east-west temperature gradient (Fig. 4.10c). Positive SST values in time series of the third temporal mode were generally observed on February-March and the negative values on May-June (Fig. 4.10f). Negative values in the second and third temporal mode of SST were in 2000-2001 (Figs. 4.10e and 4.10f). However, the second temporal mode of SST had various peaks at 9, 11, and 15 months (Fig. 4.11b). The third temporal mode of SST had various peaks at 5, 8, 11, and 15 months (Fig. 4.11c).

The first spatial mode of SST accounts for 99 % of total variance (Fig. 4.6b). The spatial pattern of the first spatial mode was similar to that of the first temporal mode (Figs. 4.10a and 4.12a). Time series shows a dominant annual component (12 months) with a maximum in January-February and a minimum in July-August (Figs. 4.11d and 4.12b). The second and third spatial modes explain about 0.1% of total variance (Fig. 4.6b), but time series are presented by harmonic seasonal cycles.

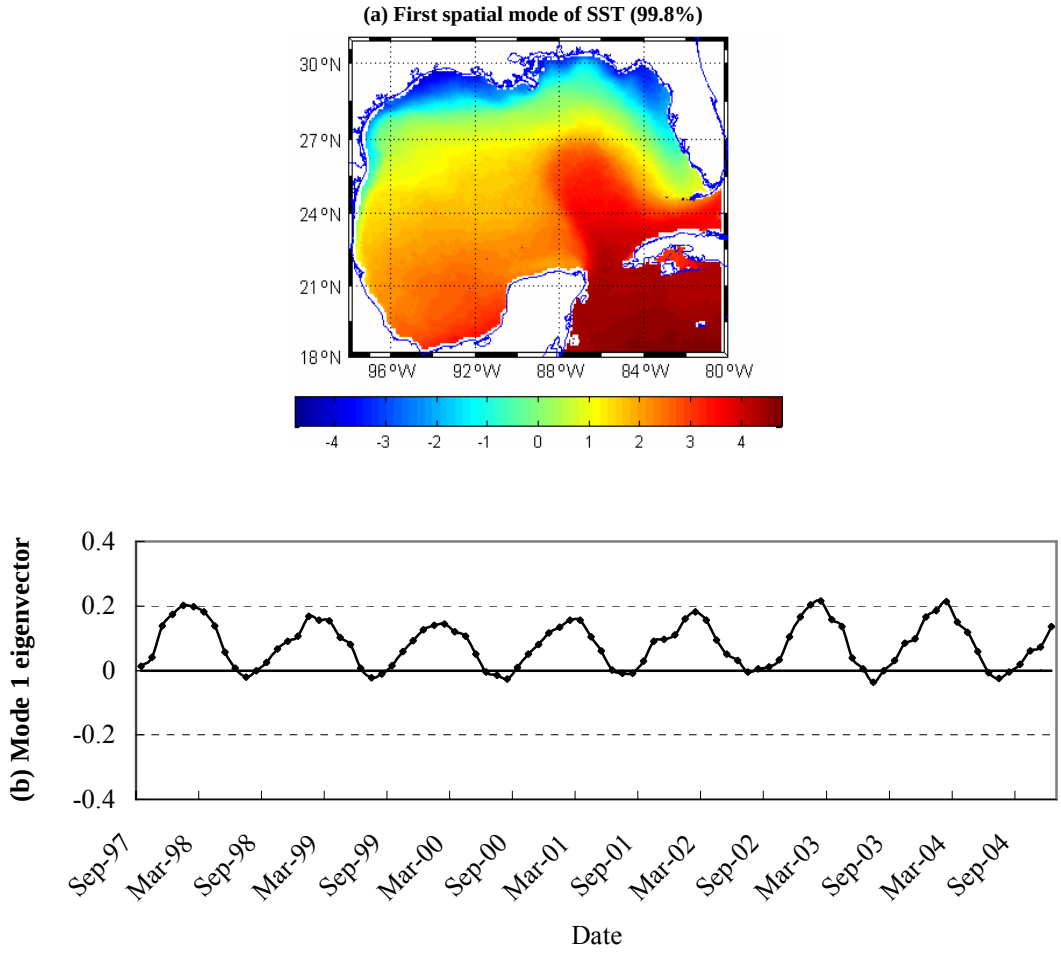

Fig. 4.12. First spatial mode of SST image for EOF pattern (a) and its time series (b) in the Gulf of Mexico.

In SSHA EOF analysis, we only explain the temporal modes, because results of the temporal and spatial EOF analysis had a similar eigenvalue and eigenvector in the historical SSHA data. The first and second temporal modes were dominant. If the first three modes are summed, they account for 88% of the total variance (Fig. 4.6c).

The first temporal mode of SSHA accounts for 57% of total variance (Fig. 4.6c). The spatial pattern of the first temporal mode shows that positive values were linked to the Loop Current, and negative values to its associated eddies (Fig. 4.13a). Positive values in time series of the first temporal mode were in 1997-1998 and 2002 and negative values in 1999-2001 and 2003 (Fig. 4.13d). Power spectrum reveals that time series of the first mode had strong non-seasonal peaks at 15 and 22 months and small peaks at 7 and 11 months (Fig. 4.14a).

The second temporal mode of SSHA explains 22% of the total variance (Fig. 4.6c). The spatial pattern of the second temporal mode presents the spatial structure of eddies and strong spatial variability in the offshore region (Fig. 4.13b). The numerical model results of Choi et al. (1995) using EOF analysis (from 1998 to 1995) suggested that the second EOF mode of SSH was associated with eddy shading events, and quasi-periodic shedding of Loop Current eddies was an important dynamic process in the Gulf of Mexico (Kantha and Clayson, 2000). However, negative SSHA value in the time series of the second mode occurred in 2000. The values fluctuated in the most of time series (Fig. 4.13e). The power spectrum shows that time series of the second temporal mode had two non-seasonal peaks at 22 and 15 months and small peaks at 9 and 7 months (Fig. 4.14b).

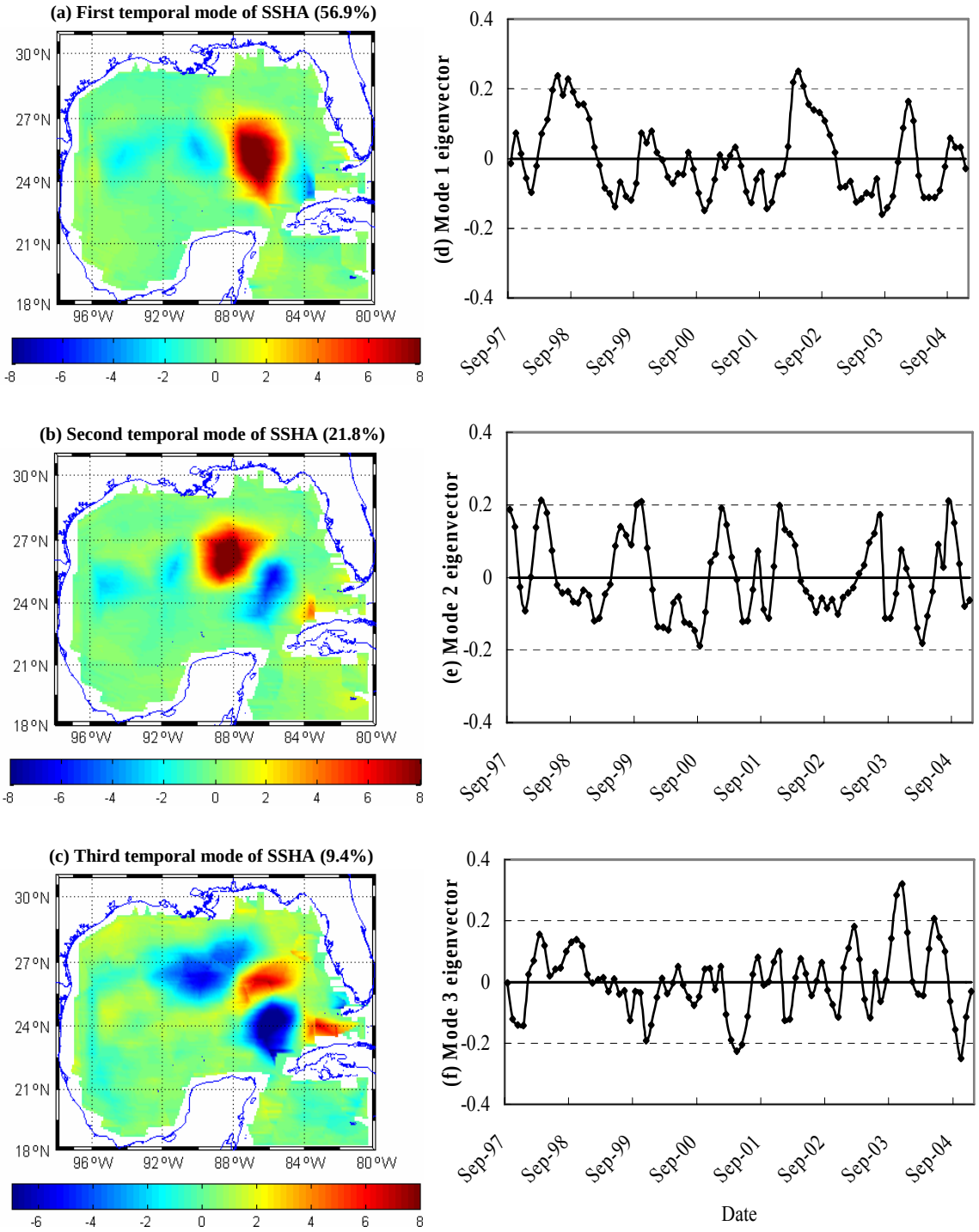

Fig. 4.13. Temporal modes of SSHA for EOF patterns (left) and their time series (right) in the Gulf of Mexico.

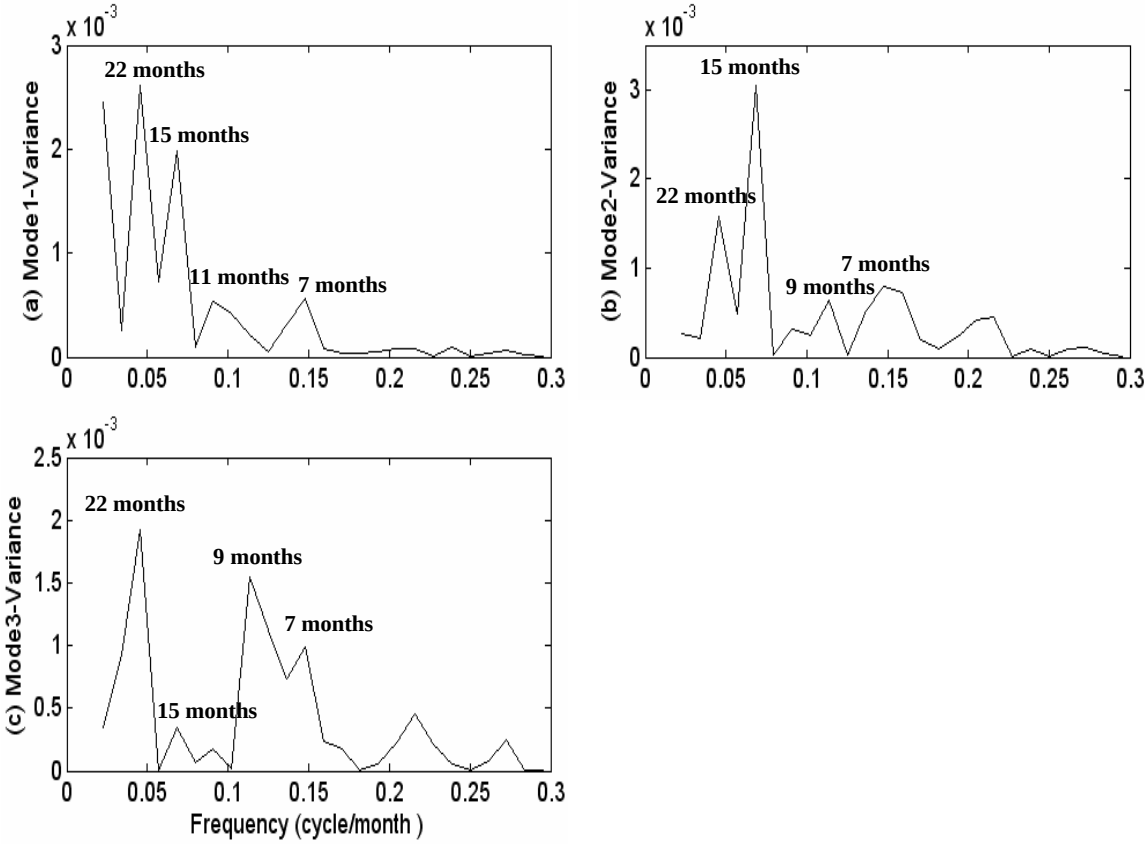

Fig. 4.14. Power spectra of time series in SSHA temporal modes of Fig. 4.13.

The third temporal mode of SSHA accounts for 9% of the total variance (Fig. 4.6c). The spatial patterns of the third temporal mode were related to the large circulation system offshore such as the structures of the Loop Current and anticyclonic/cyclonic eddies (Fig. 4.13c).

Most anticyclonic eddies tend to move west-ward and dissipate along the Gulf's western boundary, and cyclonic eddies move along the eastern boundary off the western Florida shelf, toward the south. Before reaching the Straits of Florida, cyclonic eddies either dissipate or move westward across the Loop Current as narrow tongues (Vukovich and Maul, 1985).

Positive SSHA values in time series of the third mode occurred in 1998 and negative values in 1999-2001. The values fluctuated in the rest of time series (Fig. 4.13f). The power spectrum shows that time series of the third temporal mode had two dominant peaks at 22 and 9 months (Fig. 4.14c).

The first temporal mode of SSW represents 81% of the total variance (Fig. 4.6d). The spatial pattern of the first temporal mode showed that the dominant wind was to the southwest. Positive values were observed in the central section of the study area and negative values in the western Gulf of Mexico (Fig. 4.15a). Time series in the first temporal mode of SSW fluctuated during 7 years (Fig. 4.15d). The power spectrum shows that semi-annual components (6 and 7 months) were dominant, and an inter-annual signal was on 22 months (Fig. 4.16a).

The second temporal mode of SSW accounts for 12% of the total variance (Fig. 4.6d). The spatial variation of this mode showed the appearance of extremely anticyclonic winds in the central Gulf of Mexico (Fig. 4.15b). The power spectrum shows that the dominant peaks were observed at 5 and 10 months, and an inter-annual peak at 22 months (Fig. 4.16b).

The third temporal mode of SSW accounts for 4% of the total variance (Fig. 4.6d). Winds in the spatial pattern of the third temporal mode showed negative amplitudes in the northern part of the study area and positive values in the southern part (Fig. 4.15c). In the power spectrum, the dominant peak was at 9 months, and a small peak occurred at 30 months (Fig. 4.16c).

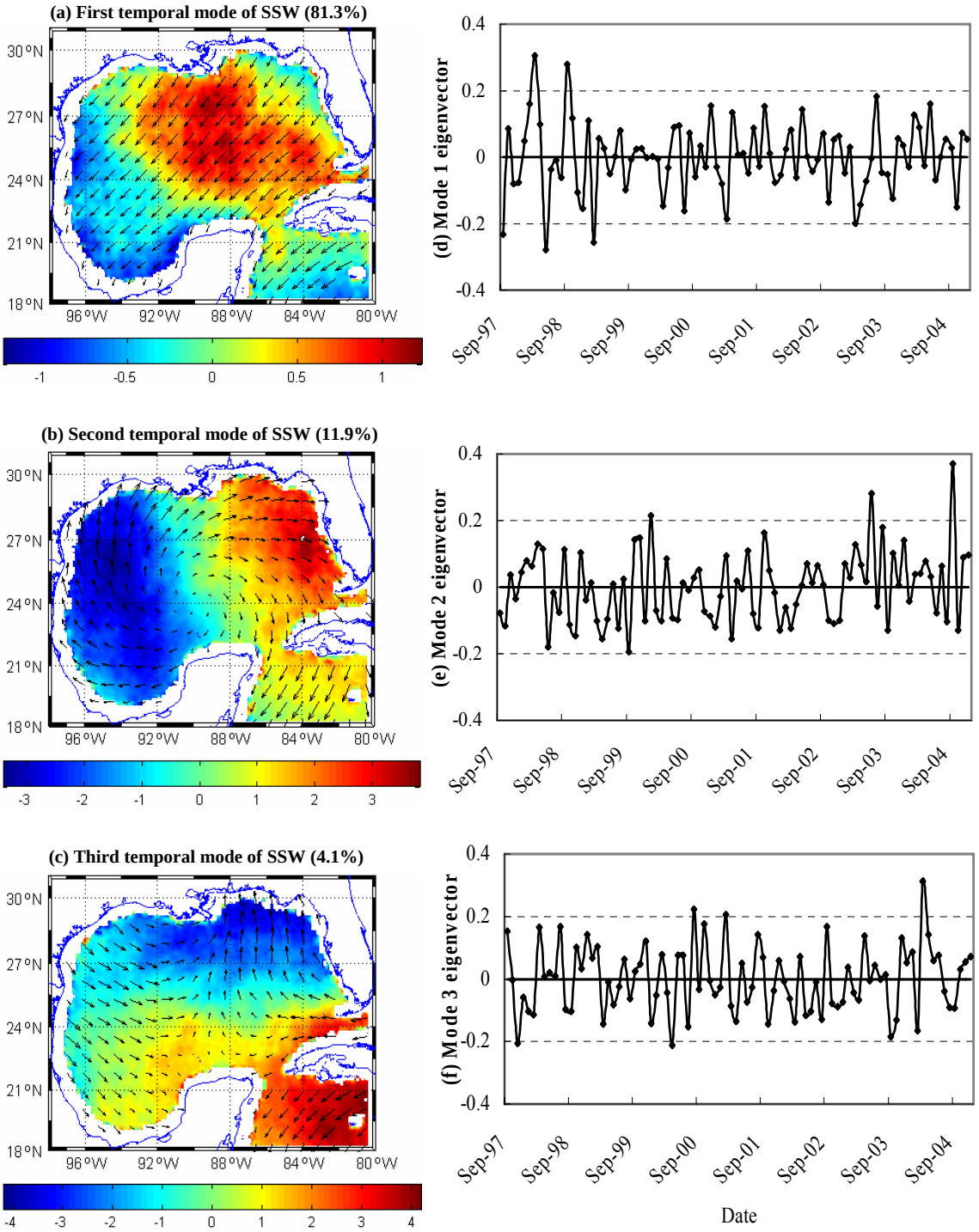

Fig. 4.15. Temporal modes of SSW for EOF patterns (left) and their time series (right) in the Gulf of Mexico.

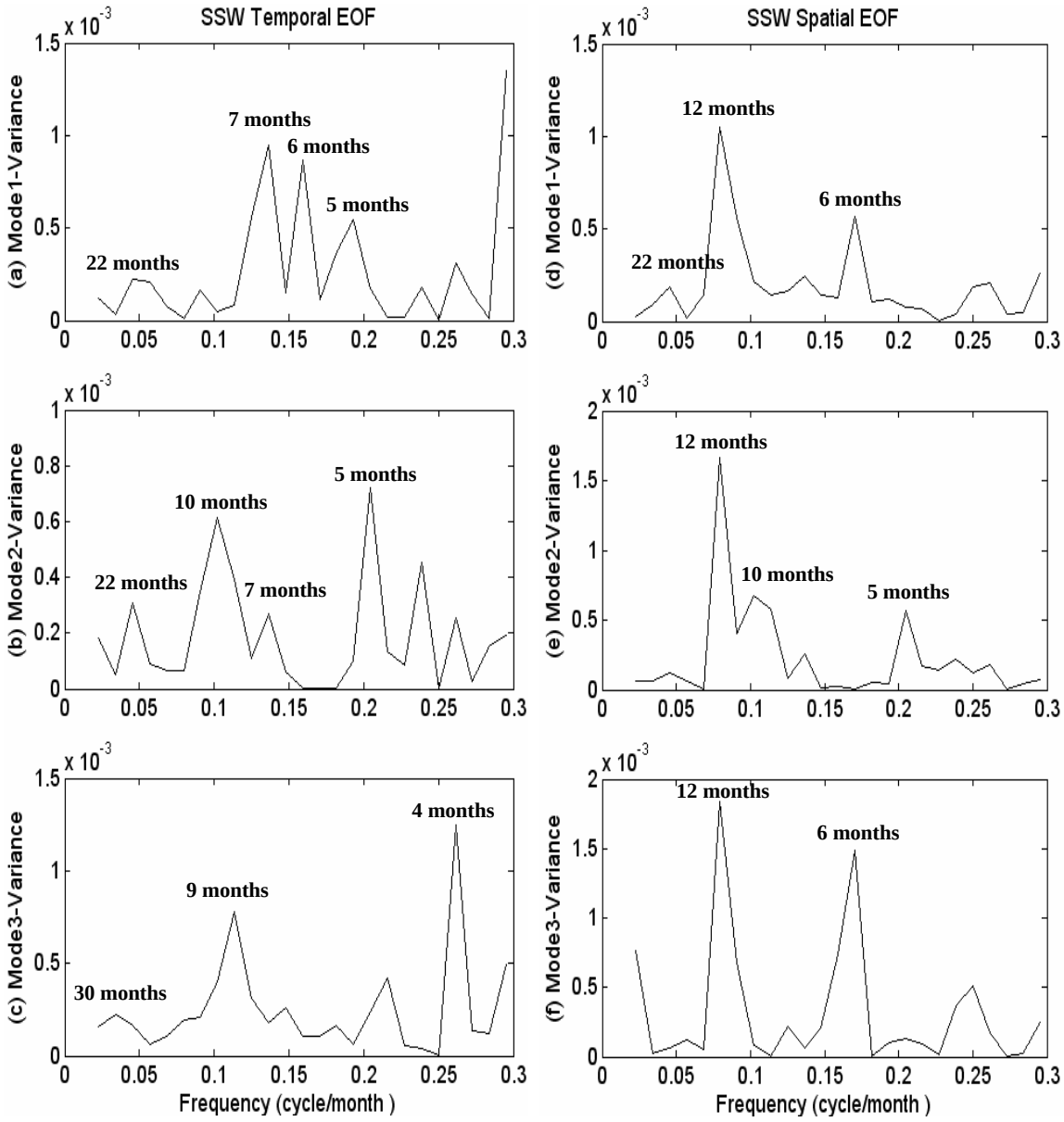

Fig. 4.16. Power spectra of time series in SSW temporal and spatial modes of Figs. 4.15 and 4.17.

The first spatial mode of SSW accounts for 73% of the total variance (Fig. 4.6d). Winds in the spatial pattern of the first spatial mode were west-northwest in the northern Gulf of Mexico. The time series in the first spatial mode of SSW had annual components with maximum peaks in September-October and minimum peaks during June-July (Fig. 4.17a). In the power spectrum, the time-series had annual and semi-annual components (6 and 12 months) and a longer period at peak 22 months (Fig. 4.16d).

The second spatial mode of SSW accounts for 15% of the total variance (Figs. 4.6d and 4.17b). The time series had a strong annual component at 12 months and a weak peak at 5 and 10 months (Fig. 4.16e).

The third spatial mode of SSW accounts for 7% of the total variance (Fig. 4.6b). The negative spatial pattern of the second spatial mode was observed in the western section of study area with west-southwestward winds (Fig. 4.17c). Time series in the third spatial mode of SSW had annual components with maximum peaks in July-August and minimum peaks in March-May (Fig. 4.17f). In the power spectrum, annual and semi-annual components were dominant at frequencies of 6 and 12 months (Fig. 4.16f).

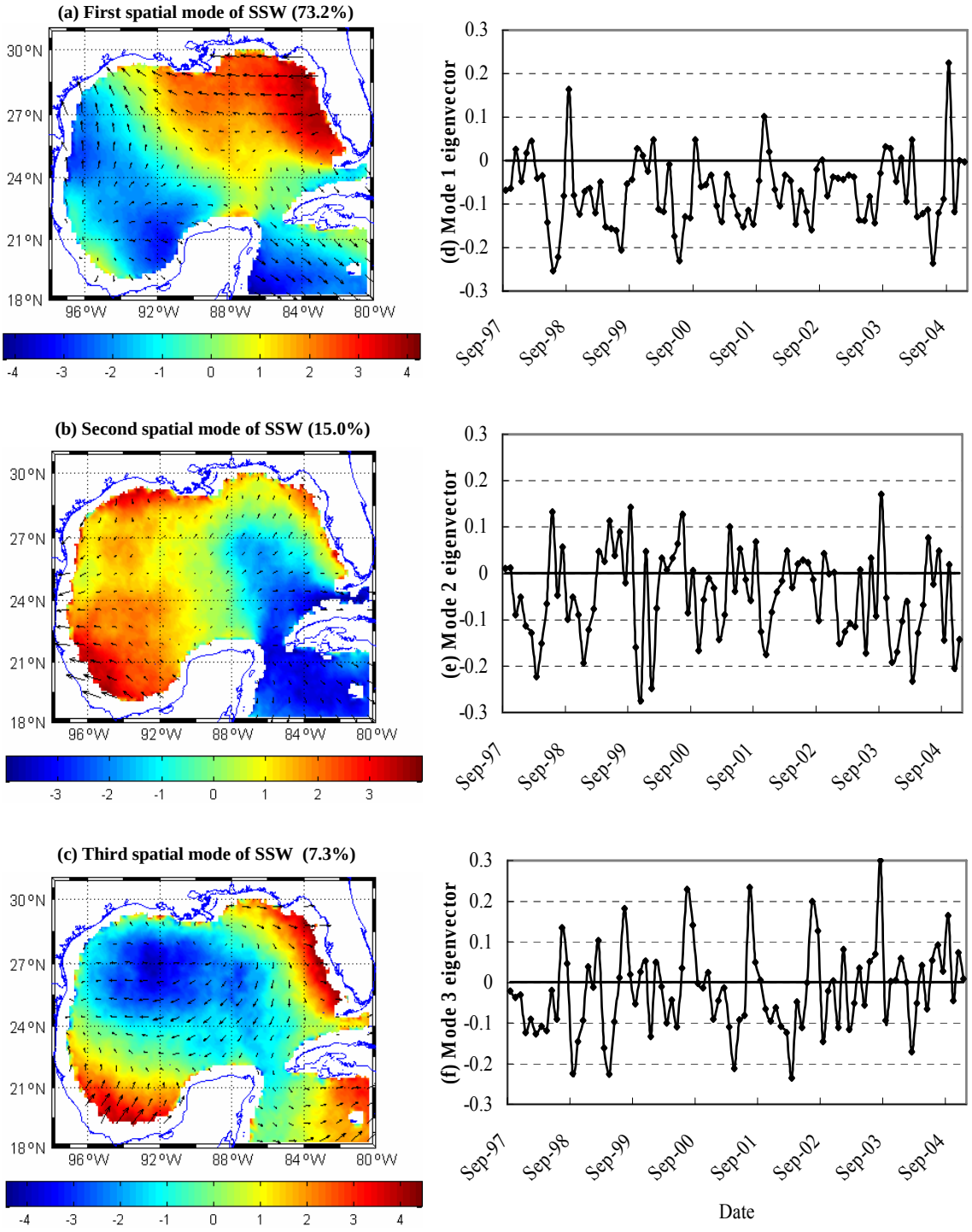

Fig. 4.17. Spatial modes of SSW for EOF patterns (left) and their time series (right) in the Gulf of Mexico.

In PR EOF analysis, we only explain the temporal modes, because results of the temporal and spatial EOF analysis had a similar eigenvalue and eigenvector in the historical PR data. The first temporal mode of PR accounts for 64% of the total variance (Fig. 4.6e). Positive PR values in the spatial pattern of the first temporal mode were observed in the northern Gulf of Mexico. Negative values were found across the southern Gulf of Mexico (Fig. 4.18a). Positive amplitudes in the time series of the first temporal mode occurred in 1998 and 2002-2003 and slightly negative values persisted during 1999-2001. During 1998 and 2002, positive peaks in the time series of the first mode were in February-March and September, and negative peaks in June. During the rest of the time series, positive peaks were observed in the spring season, and a negative peak in September (Fig. 4.18d). The power spectrum in the time series of the first temporal mode presents various peaks at 4, 5, 6, 8, and 10 months and small peak at 15 months (Fig. 4.19a).

The second and third temporal modes of PR provide approximately 5% and 3% of the total variance (Fig. 4.6e). Positive PR values in the spatial pattern of the second temporal mode were found east of the central part of the study area (Fig. 4.18b). Slightly negative values in time series were observed during 2000-2001 (Fig. 4.18e). The power spectrum reveals that dominant peaks were at 5, 6, 8, and 11 months (Fig. 4.19b). Positive values in time series of the third temporal mode were observed west of Florida (Fig. 4.18c). The power spectrum shows strong peaks at 5 and 9 months and inter-annual cycles at 18 and 30 months (Fig. 4.19c).

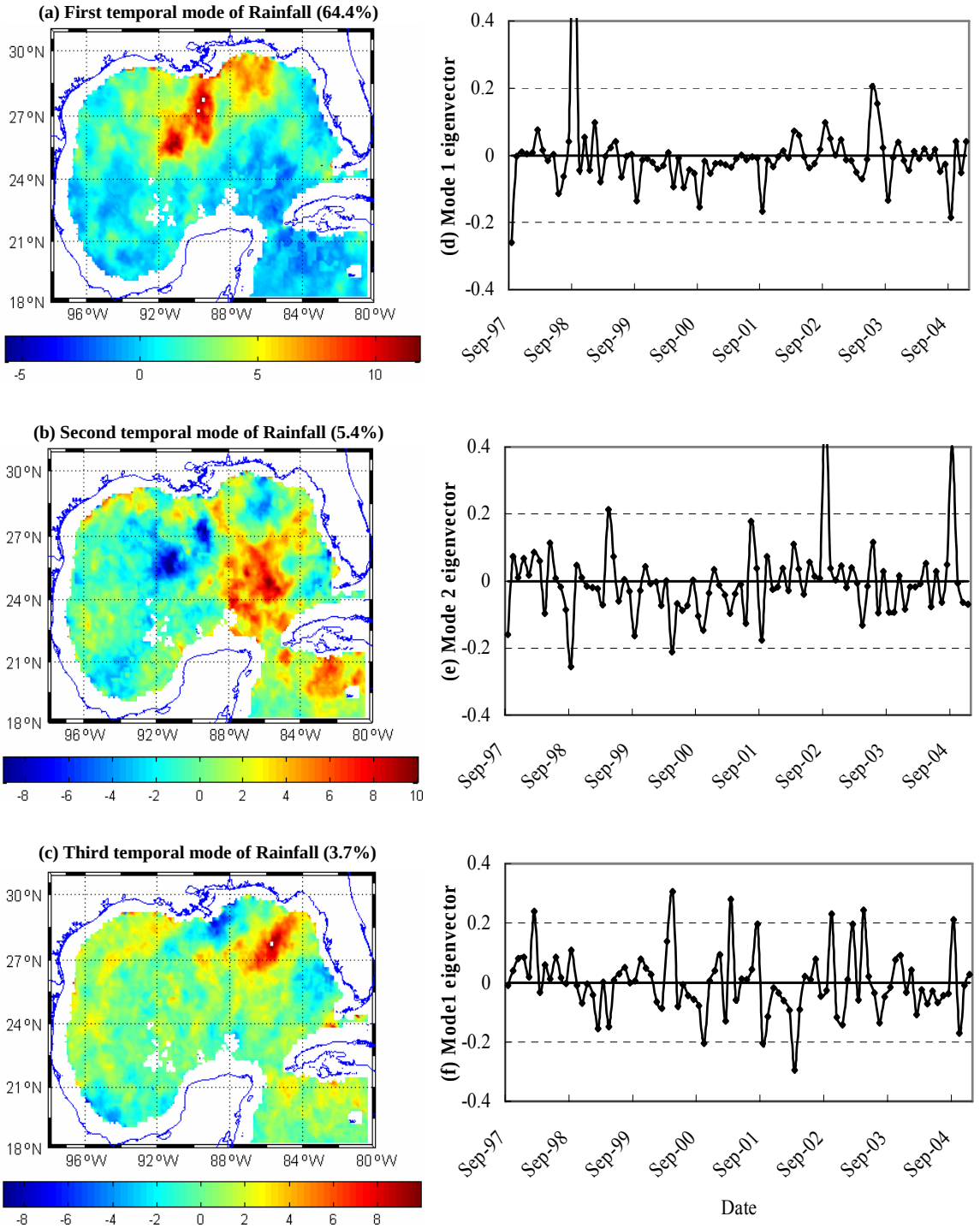

Fig. 4.18. Temporal modes of PR for EOF patterns (left) and their time series (right) in the Gulf of Mexico.

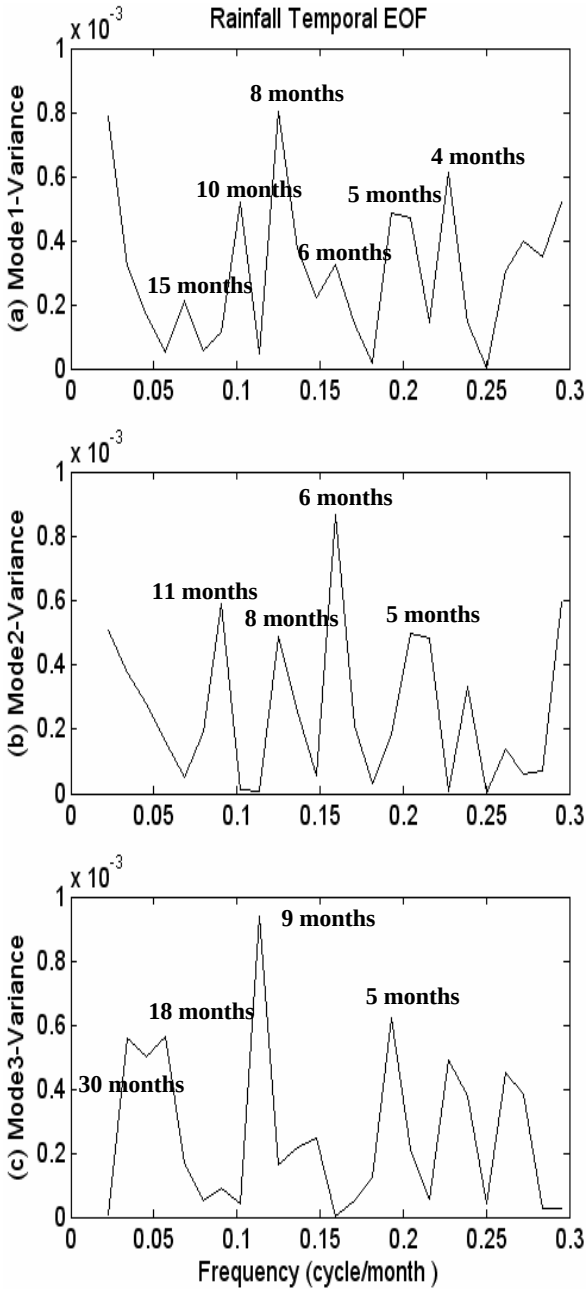

Fig. 4.19. Power spectra of time series in PR temporal modes of Fig. 4.18.

4.3.3. A Coupled Relationship of Satellite Data Sets Using CEOF

The simplest variation to EOF analysis is CEOF, developed to investigate the covariability (or joint variability) of two or more fields at a time. In CEOF analysis, the data matrix is constructed with vectors of two or more variables concatenated after one another. The correlation coefficient between the two PCs of modes provides a measure of how strongly fields are related to one another through modes (Barnett and Preisendorfer, 1987; Wallace et al., 1992; Frankignoul et al., 1996; Venegas et al., 1997).

For this study, the CEOF analysis was tested to determine relationships between POC and satellite data (SST, SSHA, SSW, and PR). All variability had significant relationships between both fields (Fig. 4.20).

The first three modes of POC and SST CEOF are dominant, which accounts for approximately 48%, 20%, and 10% of the total variance (Fig. 4.20a). The first mode showed a significant relationship between POC and SST and the highest correlation of any of the satellite data coupled correlations (SST, SSHA, SSW, and PR).

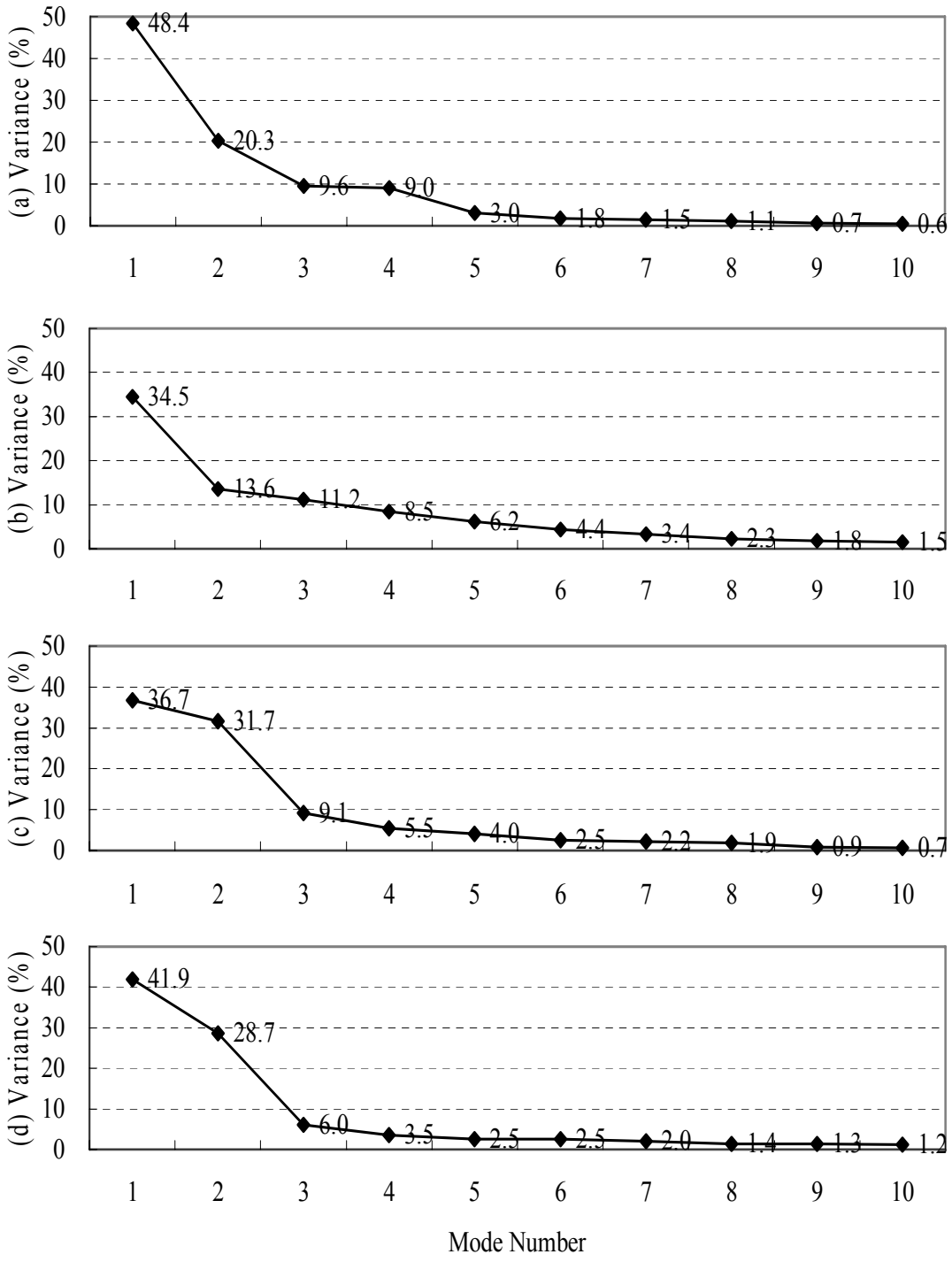

Fig. 4.20. CEOF eigenvalues between (a) POC and SST, (b) POC and SSHA, (c) POC and SSW, and (d) POC and PR for temporal variance.

There were two differences in the spatial CEOF patterns of POC and SST (Fig. 4.21). First, significant POC variations were observed along the shallow water (Case II water). Second, moderate POC variations were linked to offshore (Case I water). In SST fields, spatial amplitudes were related to the strength of the cold and warm water. Remnant cold water was observed close inshore (Figs. 4.21d and 4.21f). Warm water was associated with the Loop Current and eddies found offshore (Figs. 4.21d, 4.21e, and 4.21f). Positive POC values in the spatial pattern were negatively correlated with SST values. When positive POC values were observed along the shelf, SST values were negative (Figs. 4.21a, 4.21c, 4.21d and 4.21f). When the Loop current and Loop Current eddies were well developed (positive values), POC was neutral or decreased (negative values, Figs. 4.21c and 4.21f). When the Loop Current and eddies were not observed in SST, POC was increased (positive values, Figs. 4.21b and 4.21e).

In the time series, positive eigenvectors in the first mode of POC and SST CEOF were observed in 1997-1998 and 2001, and negative values in 1999-2000 and 2002. Values fluctuated about year in 2003-2004 (Fig. 4.22a). Positive eigenvectors in the second mode of POC and SST CEOF were found in 1997-1999. The rest of time series values were fluctuated. During 1998-2003, positive peaks occurred in March. During 2004, a large negative peak occurred in March (Fig. 4.22b). Two large positive and one negative peak occurred in the third mode of POC and SST CEOF (Fig. 4.22c).

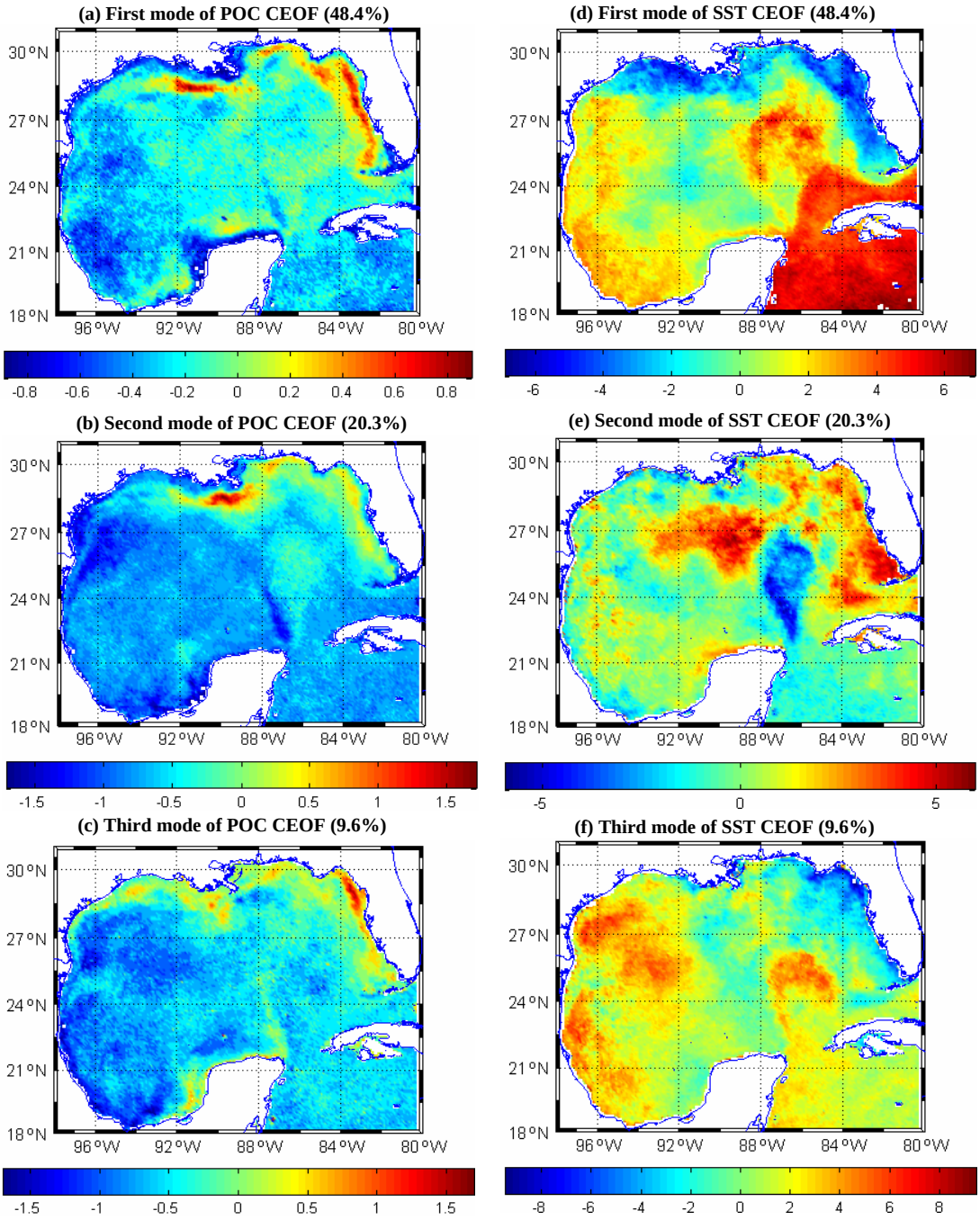

Fig. 4.21. Spatial patterns of POC and SST CEOF analysis in the Gulf of Mexico.

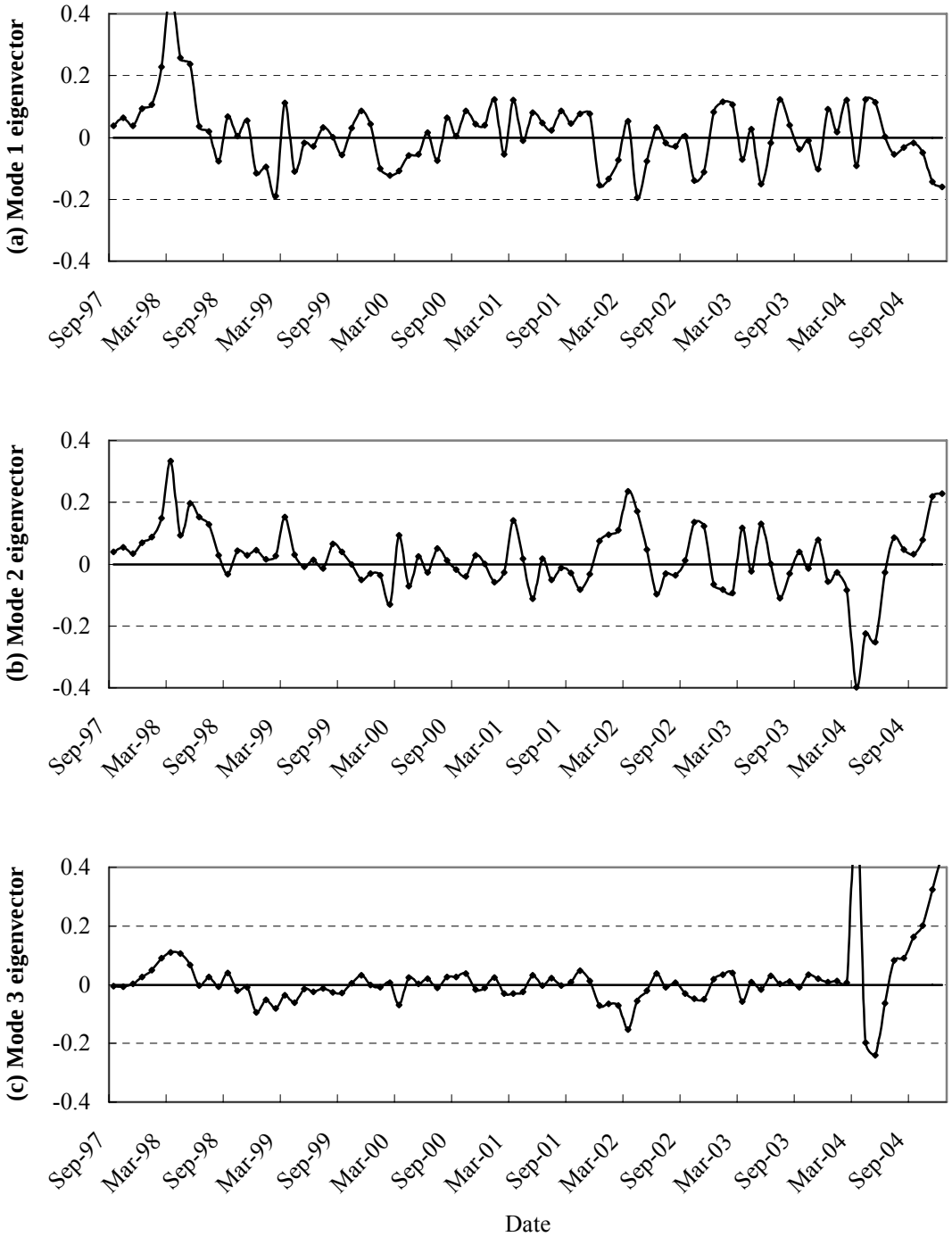

Fig. 4.22. Time series of POC and SST CEOF modes in Fig. 4.21.

In general, higher POC concentrations were primarily in shallow waters. Satellite data using altimeter and scatterometer sensors (SSHA, SSW, and PR) have high noise levels in coastal waters so they are less accurate in those regions. Therefore, historical SSHA, SSW, and PR data provide images offshore, not close to the coastline.

The first three modes of POC and SSHA CEOF accounted for 35%, 14%, and 11% of the total variance (Fig. 4.20b). When these three modes were summed, they accounted for approximately 60% of the total variance. The spatial pattern in POC and SSHA CEOF shows significant features offshore. When SSHA was negative, POC was positive. When SSHA was positive, POC was negative. Negative and positive values of SSHA in the spatial pattern were related to the Loop Current and eddies. POC in the open ocean seemed to be dependent on large-scale circulation (Fig. 4.23).

In time series, positive values in the first mode of POC and SSHA CEOF were observed during 1997-1998 and 2002, and negative values for 1999-2001 and 2003 (Fig. 4.24a). Values in the second mode of POC and SSHA CEOF fluctuated throughout the 7 years (Fig. 4.24b). Strong positive values in the third mode of POC and SSHA CEOF occurred in 1998 and the largest negative value in 2004. Most of the time series data fluctuated about year (Fig. 4.24c).

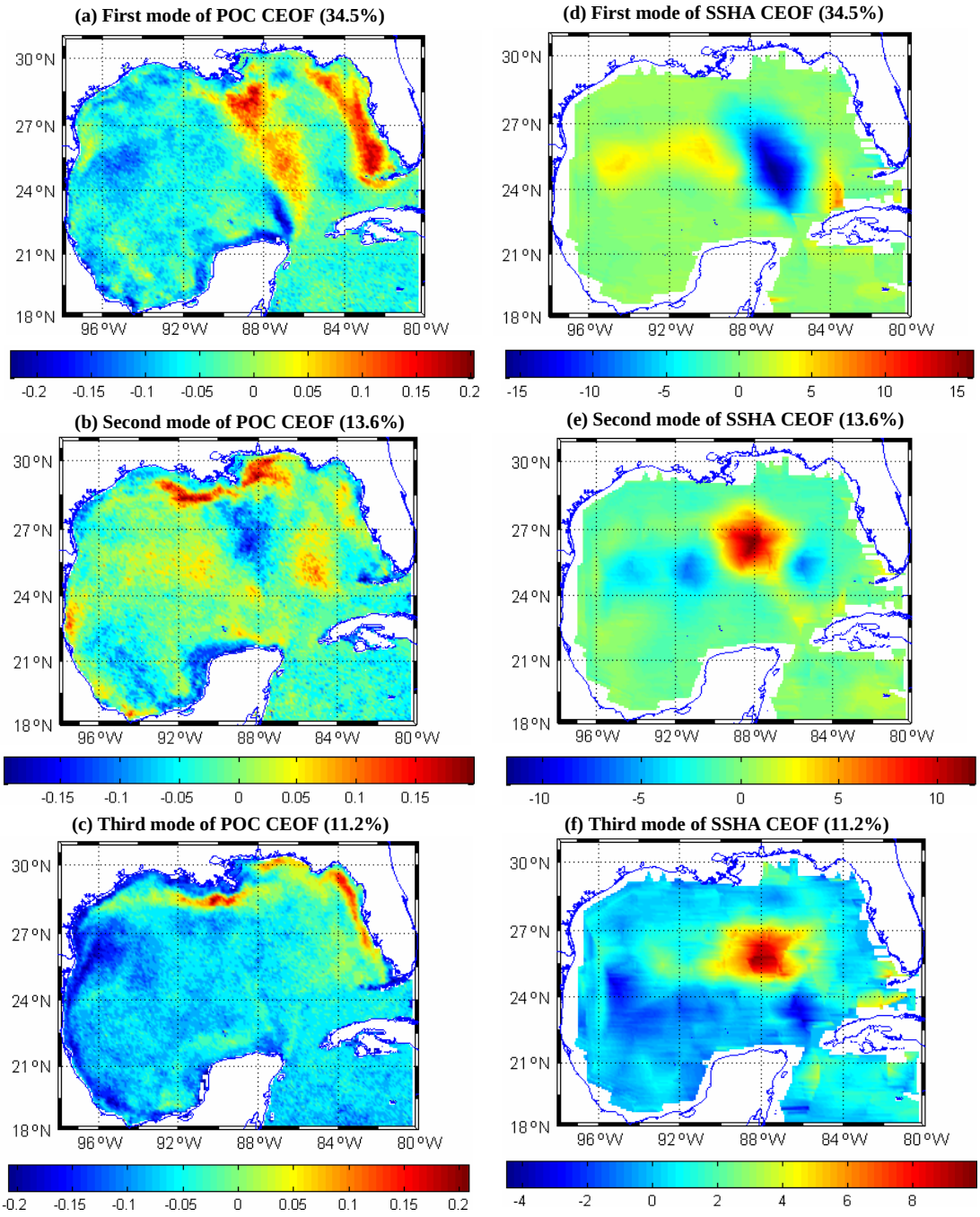

Fig. 4.23. Spatial patterns of POC and SSHA CEOF analysis in the Gulf of Mexico.

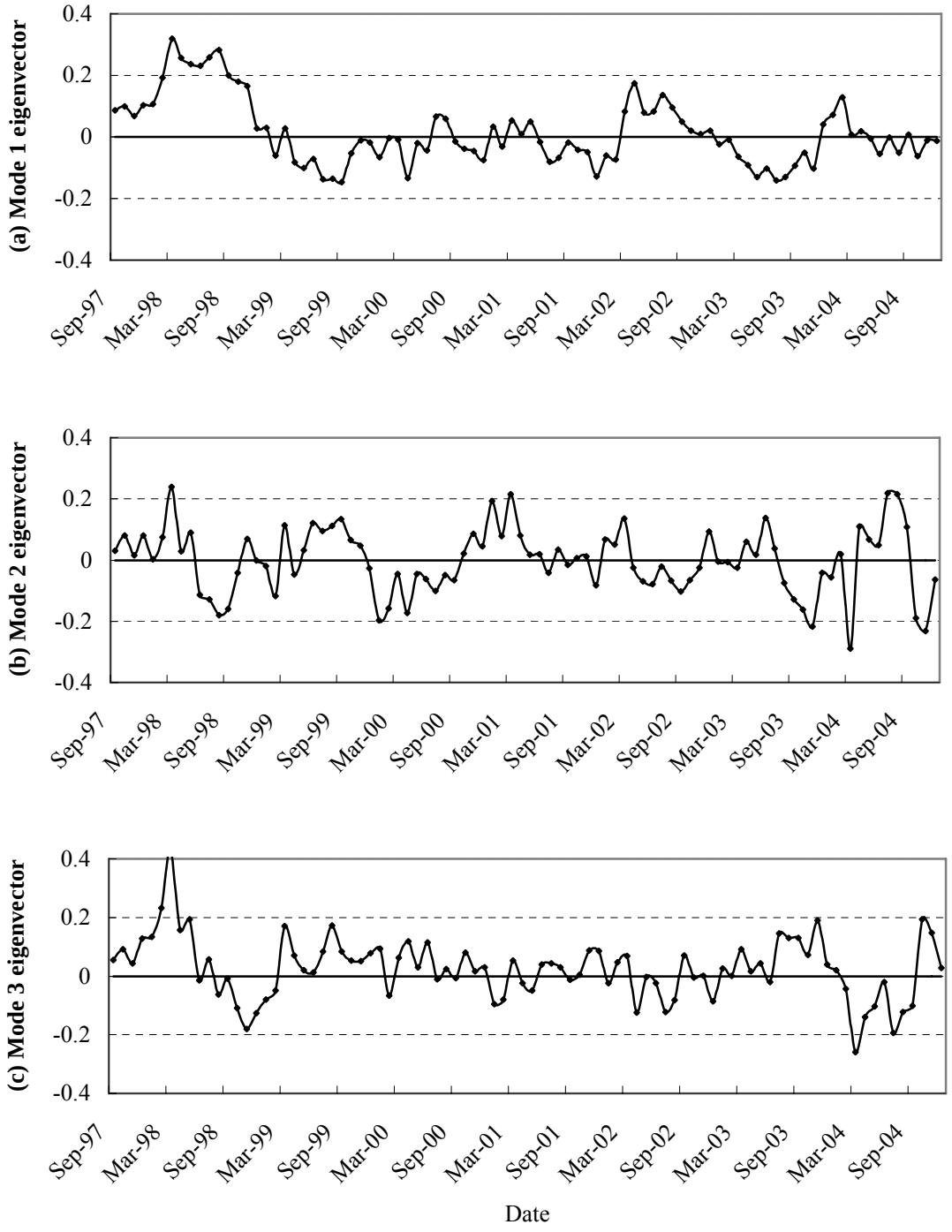

Fig. 4.24. Time series of POC and SSHA CEOF modes in Fig. 4.23.

The first three modes of POC and SSW CEOF account for 37%, 32%, and 9% of the total variance. When these three modes were summed, they accounted for approximately 78% of the total variance (Fig. 4.20c). In the spatial distribution of the first mode, positive POC values were observed on the eastern Gulf of Mexico with positive southwest winds and negative POC values on the western Gulf of Mexico (Figs. 4.25a and 4.25d). In the spatial pattern of the second and third modes, dominant southeast winds were observed in the Gulf of Mexico, but their amplitudes were changed with space. Positive and negative POC values to the second mode were constrained to the inner shelf, and positive POC values in the third mode were observed on the inner shelf as well as offshore (Fig. 4.25). Although time-series patterns in the first three modes of POC and SSW CEOF fluctuated, dominant positive values were observed in 1997-1998 (Fig. 4.26).

However, these results explained little of the physical process connecting POC and winds, especially offshore. In general, the coastal circulation was driven by wind stress (Winant et al., 1987), but the open-ocean circulation in the Gulf of Mexico was affected by the Loop Current and eddies (Hofmann and Worley, 1986; Smith, 1986; Hamilton et al., 2002; Frolov et al., 2004).

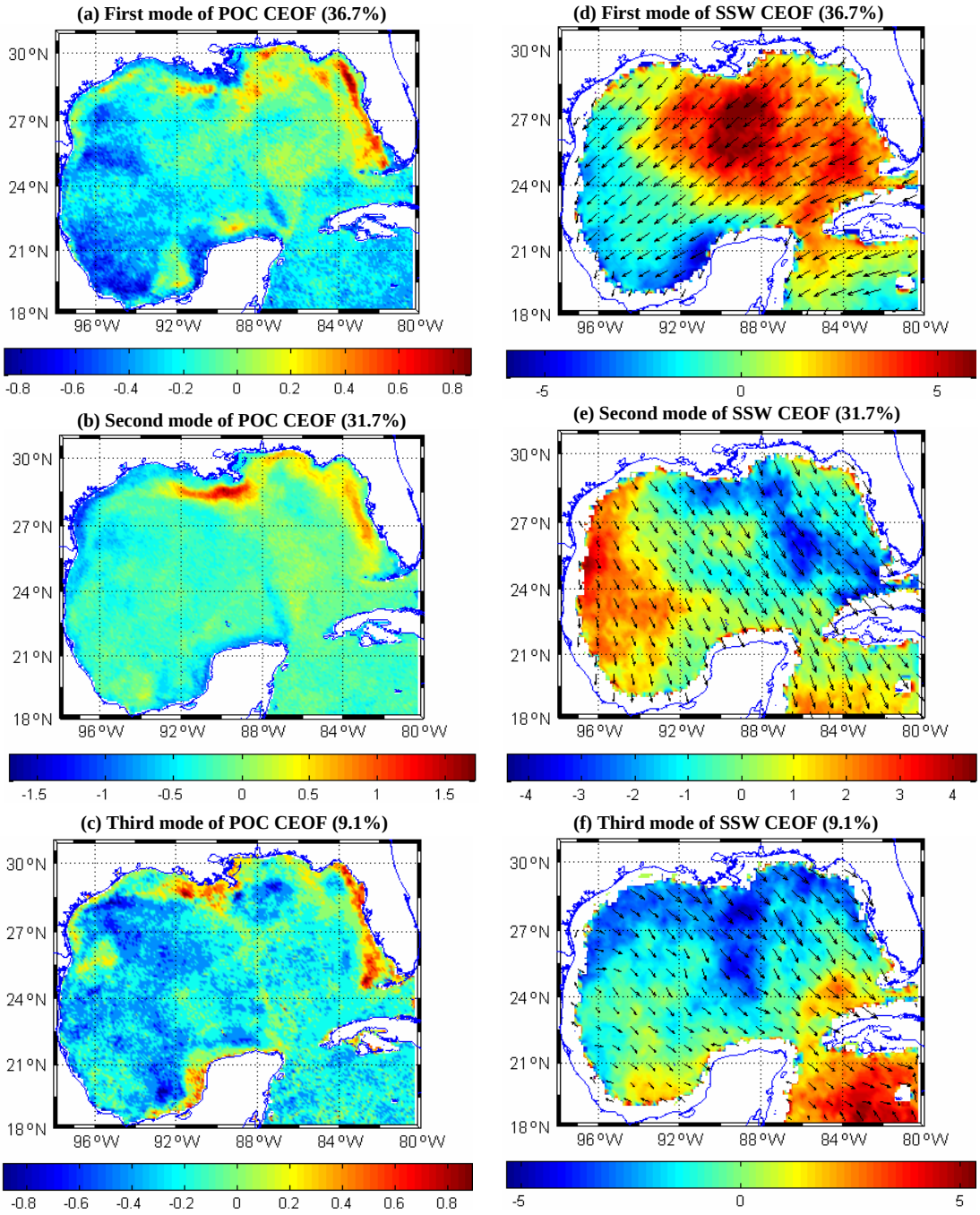

Fig. 4.25. S Spatial patterns of POC and SSW CEOF analysis in the Gulf of Mexico.

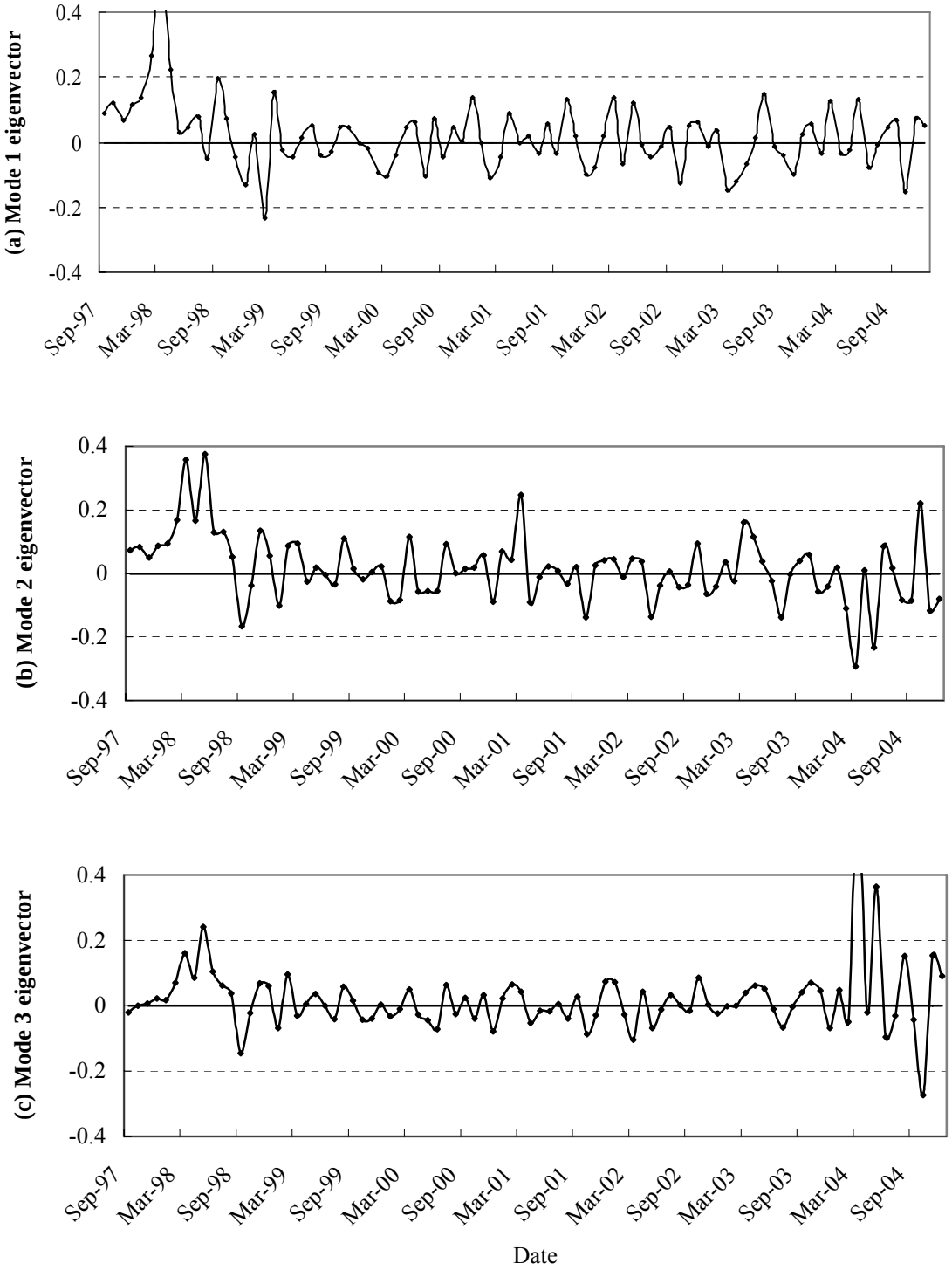

Fig. 4.26. Time series of POC and SSW CEOF modes in Fig. 4.25.

The first three modes of POC and PR CEOF account for 42%, 29%, and 6% of the total variance (Fig. 4.27). When the three modes were summed for correlation, they accounted for approximately 77% of the total variance (Fig. 4.20d).

Positive PR values in the spatial pattern of the first and second modes were well correlated with positive POC values in the northern Gulf of Mexico (Figs. 4.27a, 4.27b, 4.27d, and 4.27e). Negative POC and PR values in the spatial pattern of the first and third modes were found on the southwestern Gulf of Mexico (Figs 4.27a, 27c, 27d and 27f).

During 1997-1998, higher rainfalls were observed at time series of the first three modes (Fig. 4.28). The higher rainfalls were directly/indirectly related to output of the major rivers and influenced POC concentrations in the study area. The times-series pattern of the first mode was similar to the anomaly of river discharge in the northeastern Gulf of Mexico (Figs. 2.6 and 4.28a).

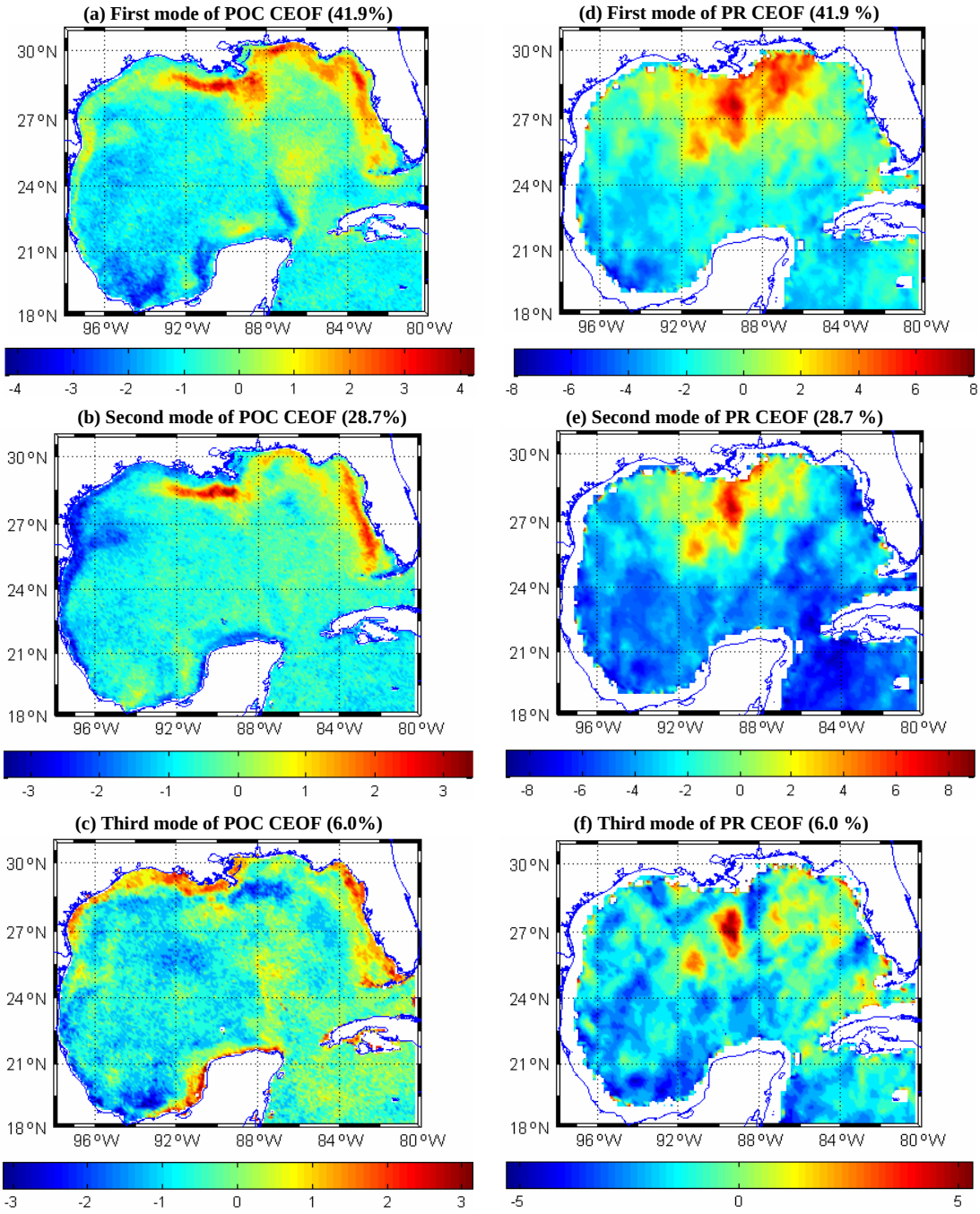

Fig. 4.27. Spatial patterns of POC and rainfall CEOF analysis in the Gulf of Mexico.

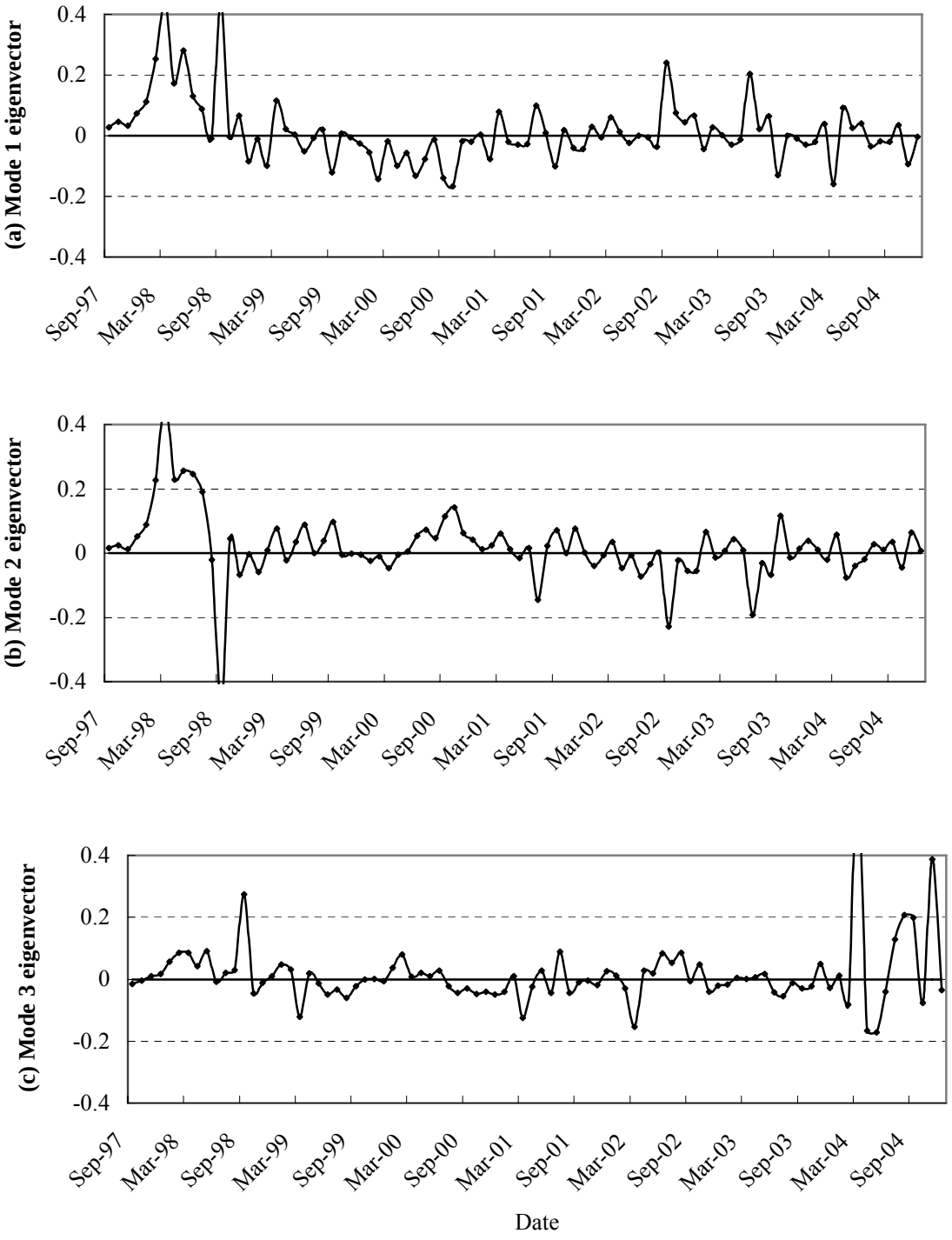

Fig. 4.28. Time series of POC and rainfall CEOF modes in Fig. 4.27.

4.4. Discussions

EOF analysis is a statistical method used to decompose a multi-variant data set into its principal components. Using this method, the bulk of the variance of a data set can be described by a few orthogonal modes, so that the major properties of the data set can be more easily understood (Preisendorfer, 1988; Unal and Ghil, 1995; Emery and Thomson, 1997; Fujii and Kamachi, 2003; Thomas et al., 2003; Son, 2005).

While EOF analysis is applicable to the time-dependent spatial fields of a single variable, coupled EOF analysis is a means of decomposing the time dependent spatial fields of two variables so that the two resulting spatial patterns have the maximum possible temporal correlation for any particular mode. This approach is useful for studying the temporal variability of two separate but related oceanographic fields (Frankignoul et al., 1996; Peng and Fyfe, 1996; Venegas et al., 1997; Fujii and Kamachi, 2003).

In this study, single and coupled EOF analysis were used to investigate the temporal and spatial variations of POC and to determine the physical processes that affect the temporal and spatial distribution of POC in the Gulf of Mexico. The temporal and spatial POC variations based on the EOF analysis suggested three general patterns in the Gulf of Mexico. First, higher POC variations were observed along the coastal regions. Second, higher POC variations were related to the direction of the river discharge, especially near the Mississippi and Alabama Rivers. Third, high POC variations were linked to the mesoscale circulation offshore.

First, POC values were elevated in shallow water along the western and eastern Gulf of Mexico (Fig. 4.7a). Maximum and minimum values of POC in time series of the first temporal mode were observed in the spring/summer and fall/winter seasons (Fig. 4.7d). In chapter two, we suggested that spatial patterns of higher surface POC concentrations were associated with the input of fresh water, stratification of the water column, and regional circulation patterns in the northern Gulf of Mexico. During the late spring and summer seasons, stratification of the water column and the buoyancy forcing of fresh water increased. The warm, fresh water easily spread out across the surface. This pattern diminished from fall to early spring. Although river discharge increased during the spring, strong wind speed caused increasing vertical mixing, reducing stratification, and higher PM and POC concentrations were constrained to the shelf rather than spreading laterally.

Anomalies of monthly major river discharges did not match precisely the POC amplitudes in time series of the first temporal mode, but the trend was similar to the time series of river discharge (Figs. 2.6 and 4.7d). Positive values of river discharge and POC were observed for 1998 and 2003-2004 and negative anomalies for 1997 and 1999-2002. During periods of 1998 and 2003-2004, higher POC concentrations were observed along the northern Gulf shelf and lower POC concentrations along the southwest Gulf shelf. During periods of 1999-2002, higher POC concentrations were found along the southwestern Gulf shelf and relatively lower POC estimates along the northern Gulf shelf (Figs. 2.6, 4.7a, and 4.7d). However, both signals were related to seasonal and inter-annual components. In the power spectrum analysis, the inter-annual cycle (30

months) of the river discharge in Florida corresponded well with the peak in the first temporal mode of POC (Figs. 4.8a and 4.29). Dominant peaks along Mississippi and Alabama showed inter-annual cycles, such as 18 and 22 months (Fig. 4.29).

The spatial pattern in the second temporal mode of POC showed the east-west variation of POC concentration. During the summer season in 1999 and 2001-2004, higher POC estimates were observed on the eastern and northeastern Gulf shelf. During the rest of the times series, higher POC estimates occurred off of southern Florida, off shelf east of the Mississippi Delta, and west of Yucatan (Fig. 4.7b). This pattern was affected slightly by long-term variations (22 months) (Figs. 4.7e and 4.8b).

However, the spatial SST patterns in the first and second temporal and spatial modes revealed important climatic variability on seasonal and inter-annual timescale (Figs. 4.10, 4.11, and 4.12). Large-scale interactions between cold and warm water mainly occurred along the northern Gulf Shelf. Higher POC concentrations were followed by cold water during the spring, which produced the nutrient-rich inshore waters (Figs. 4.10a and 4.10b). The time series of the first and second temporal mode of SST were well correlated with the first temporal mode of POC (Figs. 4.7 and 4.10).

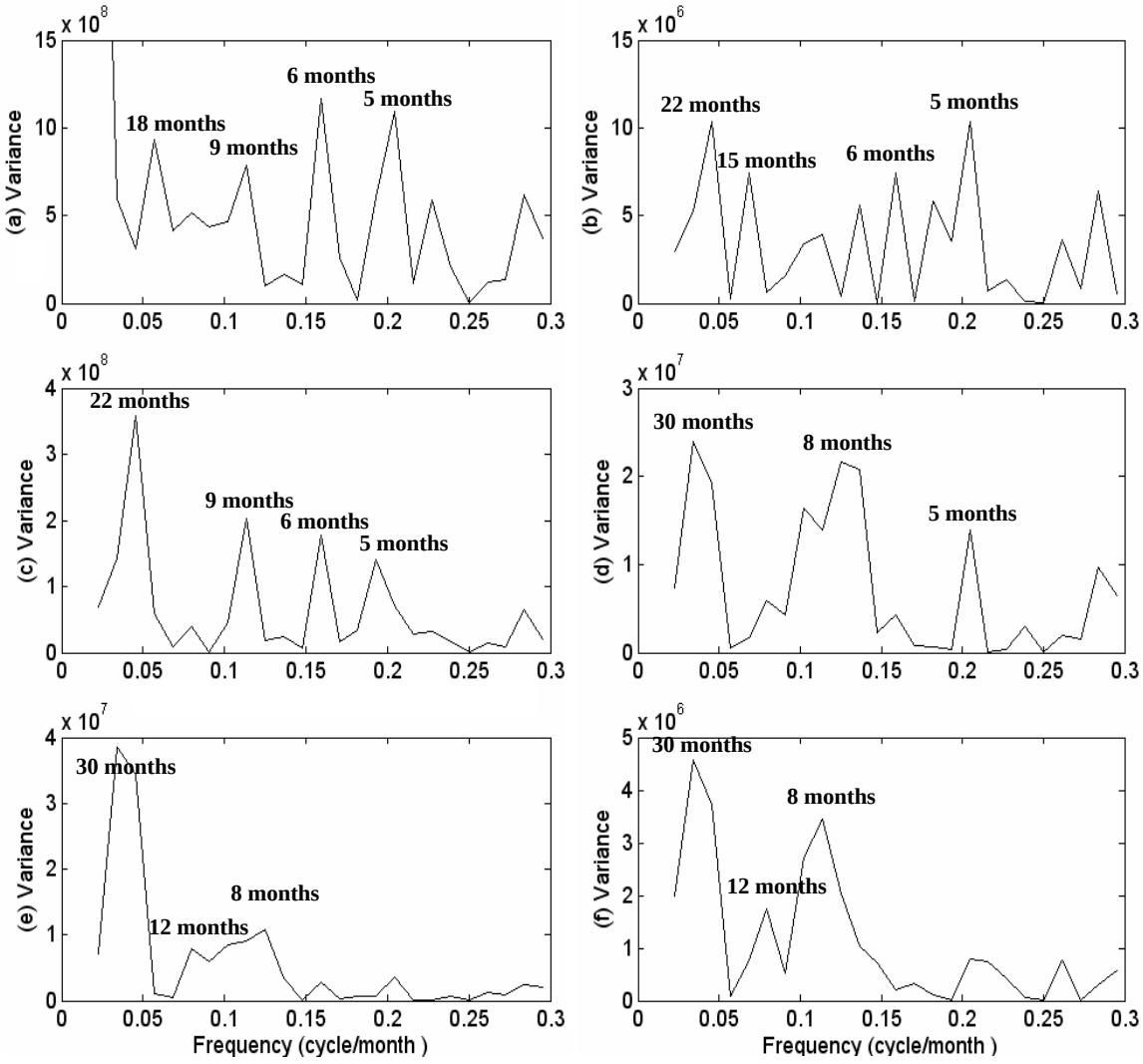

Fig. 4.29. Power spectra of time series in river discharge in Fig. 2.6. (a) the Mississippi River; (b) the Mississippi Area; (c) the Alabama Area; (d) the west Florida; (e) the middle Florida; (f) the east Florida.

Second, the variation of POC concentrations showed dispersion of the east-west trend near the Mississippi and Alabama region. In the third temporal mode of POC, the positive and negative amplitudes showed inverse signals in the east and west passes of the Mississippi Delta (Fig. 4.7c). Dispersion of fresh waters in the west passes of the Mississippi Delta was controlled by wind stress (Walker, 1996). Dispersion of fresh waters in the east passes of the Delta was affected not only by wind stress but also by buoyancy forcing and the general circulation system (Walker, 1996; Morey et al., 2003). During summer, the warm, fresh water was easily spread across surface water and was affected by mesoscale eddies and the Loop Current (Gilbes et al., 1996; Sahl et al., 1997). Time series and spatial patterns in the third temporal mode of POC were similar to the temporal mode of SST (Figs. 4.7c, 4.7f, 4.10c, and 4.10f). During 2001 and 2002, minimum peaks in the time series of POC and SST occurred in the spring seasons, but during the rest of the time series maximum peaks of POC and SST occurred in the spring seasons (Figs. 4.7f and 4.10f). Winds changed temporally and spatially (Figs. 4.15 and 4.17), but the time-series analysis indicated seasonal and inter-annual variability (Fig. 4.16). The results of a numerical model by Morey et al. (2003) showed pathways of the river discharge of the major rivers in the northern Gulf of Mexico. Their results also suggested that the local wind stress caused the export of the fresh water toward the east in the late spring and summer seasons. However, the annual cycle of POC concentration in the inshore was affected by fresh water, and the dispersion of high concentration water was influenced by the annual cycle of the local wind stress (Morey et al., 2003; Ohlmann and Niiler, 2005).

Third, a limited dispersion of POC was generally associated with the Loop Current and Loop Current Eddies. Wind stress contributed to the shelf circulation on the Gulf of Mexico, but the Loop Current and eddies were the dominant mechanism over the open ocean (Hamilton et al., 1999, 2002; Sturges and Leben, 2000; Frolov et al., 2004). Morey et al. (2003) inferred that fresh water was transported offshore by the mesoscale eddies. Cyclonic circulation causes upwelling, but anticyclonic circulation causes downwelling. Large anticyclonic eddies aperiodically pinch off from the Loop Current at intervals from 3 to 17 months (Sturges and Leben, 2000) and move westward. This circulation pattern can be observed in SST and SSHA images. Positive values in time series of SST and SSHA were observed for 1997-1998 and negative values for both 1999-2000 and 2002 years (Figs. 4.10d and 4.13d). The amplitude in the time series of SST and SSHA represented seasonal and interannual components (Figs. 4. 11 and 4.14).

Each EOF pattern and time series was useful for describing POC distributions and temporal variations. It was not enough to determine the relationship between POC and physical processes using single value EOF analysis. In order to investigate the covariability of two fields at a time, cross correlation analysis was necessary between POC and SST, POC and SSHA, POC and SSW, POC and PR, after removing the temporal mean value. Correlation coefficients between POC and SST and POC and SSHA yielded significant negative relationships.

Along the shelf of the northeastern Gulf of Mexico, positive values of POC concentrations and negative values of SST in spatial patterns of the first mode had maximum peaks in the early spring (Figs. 4.21a, 4.21d, and 4.22a). The flow of cold

continental air over the water is increasing vertical mixing, generating surface cooling, and reducing stratification. In Fig. 2.7c, during the spring season vertical profiles of temperature and salinity show that the water column was weakly stratified with cold and less salty water. However, most major rivers are concentrated in the northern Gulf of Mexico and higher river discharges occur during the spring (Fig. 2.5). Time series patterns in the first mode of POC and SST CEOF were similar to the time-series pattern of river discharge. This correlation was demonstrated by the first mode of coupled POC and SST and accounted for approximately 48% of the total variance.

The spatial pattern in POC and SSHA CEOF showed the relationship between POC concentrations and the Loop Current/eddies. Negative SSHA values were associated with positive POC values. Positive SSHA values were related to negative POC values (Fig. 4.23). However, the first and second modes of POC and SSHA CEOF show interesting spatial patterns, which POC distribution can be affected by anticyclonic and cyclonic flows.

Strictly speaking, SST and SSHA do not present directly the physical factors for controlling POC estimates, but these spatial patterns show circulation patterns offshore. In the first three modes of POC and SST/SSHA CEOF, SST and SSHA patterns offshore are related to the Loop Current and eddies. Development of anticyclonic circulation tended to diminish POC concentrations and underdevelopment of anticyclonic circulation tended to increase POC concentrations. These relationships point to important physical processes in the study area.

Anticyclonic flows (warm-core ring) are made by separation from the main stream. Cyclonic flows (cold-core ring) originate as perturbations along the northern edge of the Loop Current. However, cyclonic circulation causes upwelling that provides higher nutrients from bottom water and sometimes traps the fresh water in the northern Gulf margin.

Spatial correlation of POC and SSW was largely defined in two directions. Southwest-ward winds were dominant in mode 1, southeast-ward winds in modes 2 and 3. Positive values in the first mode were observed in the central Gulf of Mexico and southwest-ward winds helped water and PM move seaward. Second and third modes had a weak influence on dispersion high-concentration POC waters (Fig. 4.25).

Spatial correlation of POC and rainfall was positive along the northern Gulf of Mexico, especially near the Mississippi Delta (Fig. 4.27). Higher rainfall increased river discharge to the northern Gulf waters, which transported more particles and nutrients to shallow water during 1997-1998.

To better understand what happened from September 1997 to December 2004, time series of EOF analysis of monthly satellite images (POC estimates, SST, SSHA, SSW, PR, and river discharge) defined the seasonal and non-seasonal components. Most time series of spatial variance consisted of semi-annual and annual peaks at 6 and 12 months. The amplitude of the non-seasonal time-series in EOF modes was higher than normal during 1997-1998 and 2003-2004 and lower during 1999-2001. In 2002, the anomaly changed from negative to positive values. The non-seasonal peaks of POC had periods of 15, 22, and 30 months, and first mode showed a strong peak at 30 months (Fig.

4.8a). The non-seasonal components of SST modes were the periods of 15, 18, and 30 months and the first mode showed a moderate peak at 30 months (Fig. 4.11a). The non-seasonal component of SSHA EOF modes showed strong peaks at 15 and 22 months (Fig. 4.14). The non-seasonal components of SSW modes showed weak peaks at 22 and 30 months (Fig. 4.16a). The non-seasonal components of PR modes were the periods of 15, 18, and 30 months (Fig. 4.19). The power spectrum of river discharge showed strong peaks at 18, 22, and 30 months (Fig. 4.29).

However, the non-seasonal time-series indicated that POC concentration was strongly affected by the enhancement of large-scale processes. The low frequency signal in POC and physical forcing function was similar to El Niño/Southern Oscillation (ENSO) events (Fig. 4.30), which is the most important coupled ocean-atmosphere phenomena to cause global climate variability on interannual time scales (Wolter and Timlin, 1998). El Niño events occurred during 1997-1998 and 2002-2004, and La Niña conditions existed during 1999-2001. During El Niño events, the eastern Gulf of Mexico was wetter than normal (Thurman and Trujillo, 2002, Fig. 4.31). Time series of PR and river discharge from these data showed relatively positive amplitudes in the eastern Gulf Coast also. Higher runoff is consistent with positive POC amplitude along the shelf, because of high terrestrial/nutrient input. The western Gulf of Mexico was influenced by low rainfall (Thurman and Trujillo, 2002, Fig. 4.31). Decreased fresh water was related to negative POC EOF amplitude along the coast, and was also related to low nutrient input.

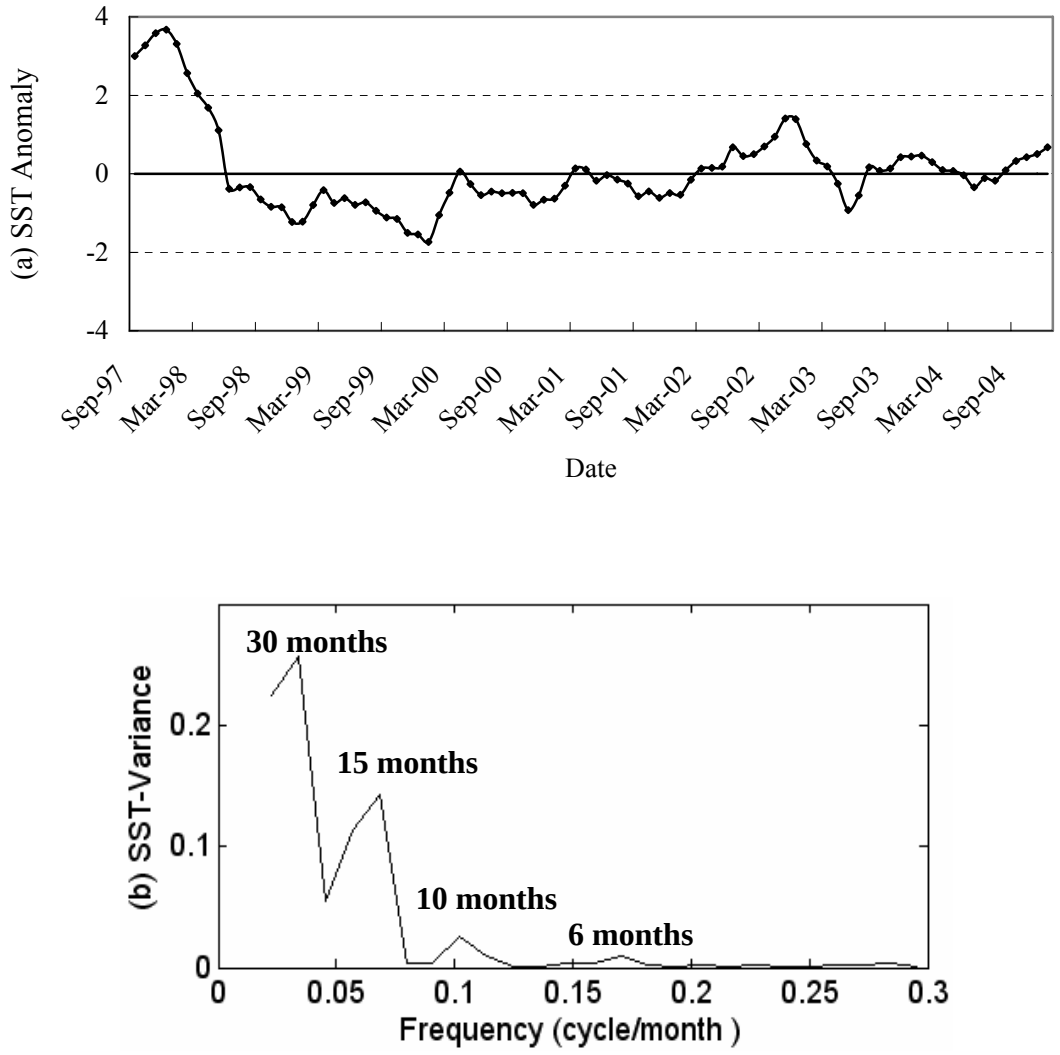

Fig. 4.30. (a) Sea surface temperature anomaly (SSTA) averaged over [5S,5N] and [150W,90W] during September 1997 and December 2004 (the eastern equatorial Pacific) - an index that measures the strength of an ENSO event. (b) Power spectra of time series in SSTA of Fig. 4.30a.

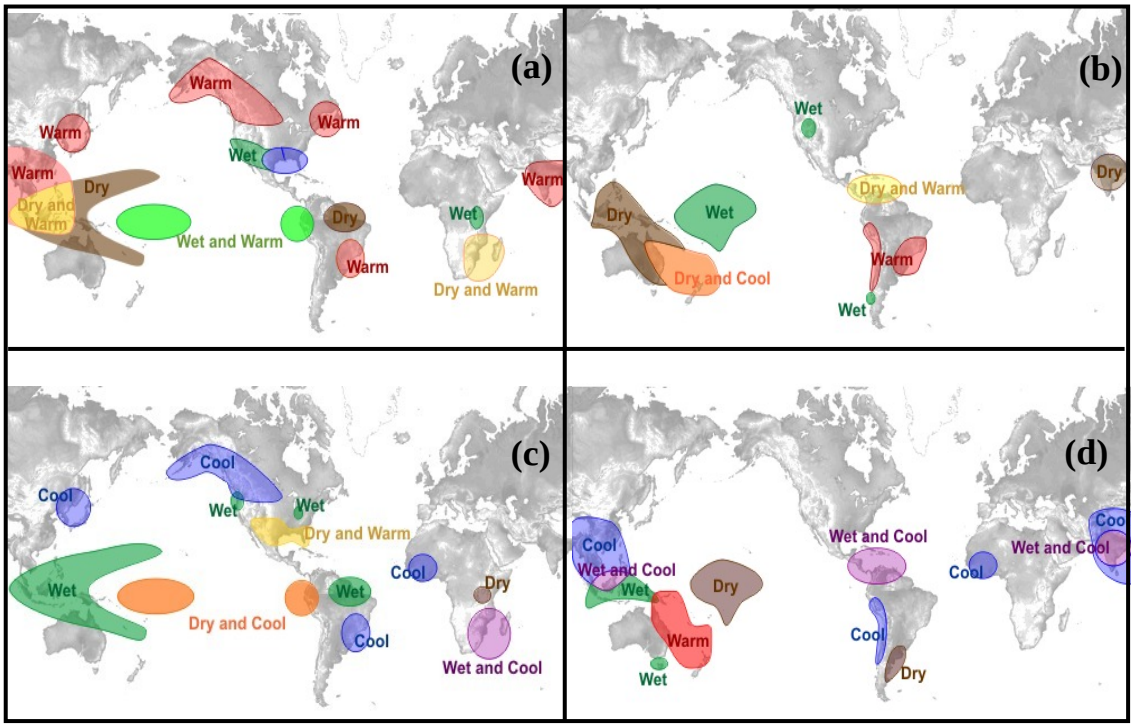

Fig. 4.31. The effects of El Niño/Southern Oscillation on the world's weather. (a) El Niño effect during December through February, (b) El Niño effect during June through August, (c) La Niña effect during December through February, and (d) La Niña during June through August (http://www.srh.weather.gov/srh/jetstream/tropics/enso_effects.htm : retrieved on November 10, 2005).

However, the forces likely to govern climate variability are air-sea heat exchange and wind stress forcing expressed as upper-ocean temperature anomalies on interannual timescales (Cayan, 1992; Miller et al., 1994; Frankignoul et al., 1996). Some studies proposed positive feedbacks between the atmospheric circulation and SST (Deser and Blackmon, 1993; Latif and Barnett, 1994). In this study, large-scale changes of SST suggest a coupled atmospheric-ocean circulation, and time series in the first three modes of SST reveal interannual variations in the Gulf of Mexico (Fig. 4.10). Moreover, variability between SST and SSH are temporally and spatially correlated with large-scale fluctuations (Figs. 4.10 and 4.13). The spatial patterns of SST and SSHA offshore showed mesoscale circulation patterns in the Gulf of Mexico such as the anticyclonic Loop Current and its associated anticyclonic and cyclonic eddies. Although the Loop Current and eddies periodically evolve and detach from the Loop Current, the influence of these eddies varied interannually in the Gulf of Mexico. Temporal and spatial surface POC concentrations may be strongly affected by interannually varying oceanic circulation.

However, POC variability correlated with non-seasonal components could be explained by one or more combined physical factors such as SST, SSHA, SSW, and input of fresh water. To better understand these correlations, it is necessary to study large scale processes, such as coupled ocean-atmosphere forcing in the Gulf of Mexico. If this information was more complete, we could more clearly explain the relationship between POC variability and physical processes.

4.5. Conclusions

In this study, using satellite estimates of POC, SST, SSHA, SSW, and PR, temporal and spatial relationships between biological and physical processes, and their response to different oceanographic forcing were investigated. Analysis of a nearly seven-year time series (September 1997 – December 2004) of satellite data throughout the Gulf of Mexico revealed seasonal and inter-annual cycles. Cycle amplitudes of POC were enhanced on the shelf and diminished offshore (Fig. 4.1). The mean field of SST showed a north-south gradient, approximately perpendicular to the coast (Fig. 4.2). The long-term mean of dynamic height had lower values inshore and higher values offshore (Fig. 4.3). Monthly SSW was varied temporally and spatially. Higher winds occurred during winter and lower winds during summer (Fig. 4.4). Higher monthly PR occurred in January-April (Fig. 4.5).

The study of POC variations using EOF analysis revealed a significant relationship between POC and single and coupled modes of SST, SSHA, SSW, and PR (Figs. 4.6 and 4.20).

Higher POC concentrations occurred in the eastern Gulf coast during summer, but in the western Gulf coast during spring. Higher POC values inshore were concentrated on the northern Gulf of Mexico (Fig. 4.7). It appeared to be influenced by river discharge and wind-driven shelf circulation. The dispersion of higher POC concentrations offshore was impacted by the strength of the Loop Current and eddies that were seen in the SST and SSHA spatial patterns (Figs. 4.10 and 4.13).

CEOF analysis between POC concentration and other physical factors (SST, SSHA, SSW, and PR) revealed that the non-seasonal component (18 and 30 months) accounted for a significant portion of the variance between parameters. For example, the first mode of POC and SST accounted for 48% of the total variance, and POC was inversely correlated with SST. This spatial pattern illustrated the east-west trend of POC concentration inshore and a limited dispersion of POC standing stock offshore (Fig. 4.21). The first mode of POC and SSHA CEOF accounted for 35% of the total variance, and POC concentration was inversely correlated with SSHA. This spatial pattern showed the relationship between POC variation and mesoscale circulation in the study area. Anticyclonic Loop Current and eddies appeared to cause lower POC concentrations, but cyclonic circulation appeared to enhance POC concentrations (Fig. 4.22). The first mode of POC and SSW accounted for 37% of the total variance (Fig. 4.23). This spatial pattern showed a positive relationship between POC concentration and wind, but these results explained little of the physical connection between POC concentration and wind, especially offshore. The first mode of POC and PR accounted for 42% of the total variance. Higher rainfall was related to larger POC concentrations in the northeastern Gulf coast (Fig. 4.24).

Power spectra of eigenvectors from POC concentrations and other physical factors revealed periods of 15, 18, 22, and 30 months. Positive values of eigenvectors occurred during 1997-1998 and 2003-2004, and negative values occurred during 1999-2001. These two periods (997-1998 and 2003-2004) were ENSO events. During ENSO events, higher POC concentration was related to high runoff and high PM/nutrient water

in the eastern Gulf of Mexico, but conditions were opposite in the western Gulf of Mexico (Figs. 4.31a and 4.31b). During 1999-2001, negative POC eigenvectors were related to normal or low river discharge, low PM/nutrient water in the eastern Gulf of Mexico (Figs. 4.31c and 4.31d).

These inter-annual differences of POC concentrations over the study period were affected by one or more physical factors related to ocean-atmospheric forcing.

CHAPTER V

CONCLUSIONS

In situ POC measurements from the NEGOM study were used to map temporal and spatial variation in the Northern Gulf of Mexico and to develop algorithms to estimate POC concentrations based on satellite data. There were nine NEGOM cruises from 1997 to 2000, and each cruise collected POC samples at 60 sites from various water types; coastal to open ocean.

The pattern of inner shelf POC concentration was correlated with mean wind stress parallel to the coast, which produced the local current system. The Loop Current and eddies dominated offshore circulation. The mean field of SST shows a north-south gradient, approximately perpendicular to the coast.

The spatial pattern of POC concentration was related to one or more factors such as river runoff, stratification of the water column, the energetic Loop Current/eddies, and buoyancy forcing.

In order to estimate POC concentration, we carried out empirical and model-based approaches with remote sensing data. In developing an empirical algorithm, the blue-to-green ratio approach using multi-spectral bands was more sensitive to non-linear conditions than using a single spectral radiance. In developing a model-based algorithm, POC estimates were derived from a relationship between *in situ* POC concentrations and the weighting factors of PCA. This approach was encouraging for POC estimates for a narrow spectral range based on remote sensing data.

In order to understand the physical processes that influence spatial and temporal POC distribution, satellite observations of several physical parameters were correlated. Analysis of 88 months (September 1997 – December 2004) of satellite data covering the Gulf of Mexico revealed both seasonal and inter-annual cycles.

Inter-annual differences of POC concentration were related to ENSO cycles. During the El Niño events (1997-1998 and 2002-2004), the higher POC concentrations existed and were related to high runoffs in the eastern Gulf of Mexico, but the opposite conditions in the western Gulf of Mexico. During La Niña conditions (1999-2001), low POC concentration was related to normal or low river discharge, and low PM/nutrient waters in the eastern Gulf of Mexico, but the opposite conditions in the western Gulf of Mexico.

REFERENCES

Atkinson, P.M., Tatnall, A.R.L., 1997. Introduction neural network in remote sensing. International Journal of Remote Sensing 18(4), 699-709.

Barnett, T.P., Preisendorfer, R.W., 1987. Origins and levels of monthly and seasonal forecast skill for United States surface air temperatures determined by canonical correlation analysis. Monthly Weather Review 115, 1825-1850.

Behrenfeld, M.J., Boss, E., 2003. The beam attenuation to chlorophyll ratio: an optical index of phytoplankton physiology in the surface ocean? Deep-Sea Research I 50, 1537-1549.

Behrenfeld, M.J., Boss, E., Siegel, D., Shea, D.M., 2005. Carbon-based ocean productivity and phytoplankton physiology from space. Global Biogeochemical Cycles 19, GB1006 (doi:10.1029/2004GBoo2299).

Berelson, W.M., 2001. The flux of particulate organic carbon into the ocean interior: a comparison of four U.S. JGOFS regional studies. Oceanography 13(4), 59-67.

Berglund, B.L., 1989. The distribution of particulate matter in the equatorial and subtropical South Atlantic Ocean: evidence for sources, transport and sinks of particles. M.S. thesis, Texas A&M University, College Station.

Bhargava, D.S., Mariam, D.W., 1990. Spectral reflectance relationships to turbidity generated by different clay materials. Photogrammetric Engineering and Remote Sensing 56, 225-229.

Bishop, J.K.B., 1999. Transmissometer measurement of POC. Deep-Sea Research I 46(2), 353-369.

Bishop, J.K.B., Calvert, S.E., Soon, M.Y.S., 1999. Spatial and temporal variability of POC in the northeast Subarctic Pacific. Deep-Sea Research II 46, 2699-2733.

Blaha, J., Sturges, W., 1981. Evidence for wind-forced circulation in the Gulf of Mexico. Journal of Marine Research 39, 711-734.

Boss, E., Twardowski, M.S., Herring, S., 2001. Shape of the particulate beam attenuation spectrum and its inversion to obtain the shape of the particulate size distribution. Applied Optics 40, 4885-4893.

Bretherton, C.S., Smith, C., Wallace, J.M., 1992. An intercomparison of methods for finding coupled patterns in climate data. Journal of Climatology 5, 541-560.

Brooks, D.A., Legeckis, R.V., 1982. A ship and satellite view of hydrographic features in the western Gulf of Mexico. Journal of Geophysical Research 87, 4195-4206.

Bukata, R.P., Jerome, J.H., Bruton, J.E., Jain, S.C., Zwick H.H., 1981. Optical water quality model of Lake Ontario. 1: determination of the optical cross sections of organic and inorganic particulates in Lake Ontario. Applied Optics 20(9), 1696-1703.

Carder, K.L., Chen, F.R., Lee, Z.P., Hawes, S.K., Kamykowski, D., 1999. Semianalytic moderate resolution imaging spectrometer algorithms for chlorophyll a and absorption with bio-optical domains on nitrate-depletion temperatures. Journal of Geophysical Research 104(3), 5403-5421.

Carr, M.E., Friedrichs, M.A.M., Schmeltz, M., Aita, M.N., Antoine, D., Arrigo, K.R., Asanuma, I., Aumont, O., Barber, R., Behrenfeld, M., Bidigare, R., Buitenhuis, E.T., Campbell, J., Coitti, A., Dierssen, H., Dowell, M., Dunne, J., Esaias, W., Gentili, B., Gregg, W., Groom, S., Hoepffner, N., Ishizaka, J., Kameda, T., LeQuere, C., Lohrenz, S., Marra, J., Melin, F., Moore, J.K., Morel, A., Reddy, T.E., Ryan, J., Scardi, M., Smyth, T., Turpie, K., Tilstone, G., Waters, K., Yamanaka, Y., 2006. A comparison of global estimate of marine primary production from ocean color. Deep-Sea Research II, in press.

Cayan, D.R., 1992. Latent and sensible heat flux anomalies over the northern oceans; driving the sea surface temperature. Journal of Physical Oceanography 22, 859-881.

Cho, B.C., Azam, F., 1990. Biogeochemical significance of bacterial biomass in the ocean's euphotic zone. Marine Ecology Progress Series 63, 253-259.

Cho, K.W., Reid, R.O., Nowlin, W.D., 1998. Objectively mapped stream function fields on the Texas-Louisiana shelf based on 32 months of moored current meter data. Journal of Geophysical Research 103, 10377-10390.

Choi, J.K., Kantha, L.H., Leben, R.R., 1995. A nowcast/forecast experiment using TOPEX/Poseidon and ERS-1 altimetric data assimilation into a three-dimensional circulation model of the Gulf of Mexico. In: Poster Presentation at the IUGG XXI General Assembly, July 1995, Boulder, CO.

Chung, S.P., Gardner, W.D., Richardson, M.J., Walsh, I.D., Landry, M.R., 1996. Beam attenuation by microorganisms: spatial and temporal variations in small particles along 140°W during 1992 JGOFS-EqPac transects. Deep-Sea Research II 43, 1205-1226.

Chung, S.P., Gardner, W.D., Landry, M.R., Richardson, M.J., Walsh, I.D., 1998. Beam attenuation by microorganisms and detrital particles in the equatorial Pacific. Journal of Geophysical Research-Ocean 103, 12669-12681.

Claustre, H., Morel, A., Babin, M., Cailliau, C., Marie, D., Marty, J.-C., Tailliez, D., Vaulot, D., 1999. Variability in particle attenuation and chlorophyll fluorescence in the Tropical Pacific: scales, patterns, and biogeochemical implications. Journal of Geophysical Research-Ocean 104 (C2), 3401-3422.

Cochrane, J.D., Kelly, F.J., 1986. Low frequency circulation on the Texas-Louisianan continental shelf. Journal of Geophysical Research – Oceans 91, 10645-10659.

Cragg, J., Mitchum, C., Sturges, W., 1982. Wind induced sea-surface slopes on the West Florida Shelf. Journal of Physical Oceanography 13, 2201-2212.

Depetris, P.J., 1996. Riverine transfer of particulate matter to ocean system. In: Particle Flux in the Ocean. John Wiley & Sons, Ltd., Chichester, New York, p. 53-69.

Deser, C., Blackmon, M.L., 1993. Surface climate variations over the North Atlantic Ocean during winter: 1900-1989. Journal of Climate 6, 1743-1753.

DiMarco, S.F., Reid, R.O., 1998. Characterization of the principal tidal current constituents on the Texas-Louisiana shelf. Journal of Geophysical Research 103, 3093-3109.

Doerffer, R., Fischer, J., 1994. Concentrations of chlorophyll, suspended matter, and gelbstoff in case II waters derived from satellite coastal zone color scanner data with inverse modeling methods. Journal of Geophysical Research 99, 7457-7466.

Doney, S.C., Ducklow, H., 2006. A decade of synthesis and modeling in the U.S. Joint Global Ocean Flux Study. Deep-Sea Research II, in press.

Dudek, A.V., Cunningham, A., McKee, D., 2003. Regional validation of SeaDAS algorithms and remote sensing of a complex frontal structure in the southern Irish Sea. Proceedings of Remote Sensing of the Ocean and Sea Ice 2003 5233, 69-76.

DuRand, M.D., Olson, R.J., Chisholm, S.W., 2001. Phytoplankton population dynamics at the Bermuda Atlantic time-series station in the Sargasso Sea. Deep-Sea Research II 48, 1983-2003.

Emery, W.J., Thomson, R.E., 1997. Data Analysis Methods in Physical Oceanography. Pergamon, Oxford, 643pp.

Eppley, R.W., Chavez, F.P., Barber, R.T., 1992. Standing stocks of particulate carbon and nitrogen in the equatorial Pacific at 150°W. Journal of Geophysical Research 97, 655-661.

Fischer, J., 1985. On the information content of multispectral radiance measurements over an ocean. International Journal of Remote Sensing 6(5), 773-786.

Fischer, J., Doerffer, R., Grassl, H., 1986. Factor analysis of multispectal radiance over coastal and open ocean water based on radiative transfer calculations. Applied Optics 25(3), 448-456.

Frankignoul, C., Bonjean, F., Reverdin, G., 1996. Interannual variability of surface currents in the tropical Pacific during 1987-1993. Journal of Geophysical Research 101(C2), 3629-3647.

Frolov, S.A., Sutyrin, G.G., Rowe, G.D., Rothstein, L.M., 2004, Loop Current eddy interaction with the western boundary in the Gulf of Mexico. Journal of Physical Oceanography 34, 2223-2237.

Fujii, Y., Kamachi, M., 2003. Three-dimensional analysis of temperature and salinity in the equatorial Pacific using a variational method with vertical coupled temperature-salinity empirical orthogonal function modes. Journal of Geophysical Research 108(C9), 3297 (doi:10.1029/2002JC001745).

Gardner, W.D., Richardson, M.J., Walsh, I.D., Berglund, B.L., 1990. *In-situ* optical sensing of particles for determination of oceanic processes: what satellite can't see, but transmissometers can. Oceanography 3, 11-17.

Gardner, W.D., Walsh, I.D., Richardson, M.J., 1993. Biophysical forcing of particle production and distribution during a spring bloom in the North Atlantic. Deep-Sea Research II 40, 171-195.

Gardner, W.D., Chung, S.P., Richardson, M.J., Walsh, I.D., 1995. The oceanic mixed-layer pump. Deep-Sea Research II 42, 757-775.

Gardner, W.D., Gundersen, J.S., Richardson, M.J., Walsh, I.D., 1999. The role of diel variations in mixed-layer depth on the distribution, variation, and export of carbon and chlorophyll in the Arabian Sea. Deep-Sea Research II 46, 1833-1858.

Gardner, W.D., Richardson, M.J., Smith, W.O., 2000. Seasonal patterns of water column particulate organic carbon and fluxes in the Ross Sea, Antarctica. Deep-Sea Research II 47, 3423-3449.

Gardner, W.D., Blakey, J.C., Walsh, I.D., Richardson, M.J., Pegau, S., Zaneveld, J.R.V., Roesler, C., Gregg, M.C., MacKinnon, J.A., Sosik, H.M., Williams III, A.J., 2001. Optics, particles, stratification and storms on the New England continental shelf. Journal of Geophysical Research 106, 9473-9497.

Gardner, W.D., Richardson, M.J., Carlson, C.A., Hansell, D., Mishonov, A.V., 2003. Determining true particulate organic carbon: bottle, pumps and methodologies. Deep-Sea Research II 50, 655-674.

Gardner, W.D., Mishonov, A.V., Richardson, M.J., 2006. Global POC concentrations from in-situ and satellite data. Deep-Sea Research II, in press.

Garver, S.A., Siegel, D.A., 1997. Inherent optical property inversion of ocean color spectra and its biogeochemical interpretation: 1. time series from the Sargasso Sea. Journal of Geophysical Research 102(C8), 18607-18625.

Gilbes, F., Thomas, C., Walsh, J.J., Muller-Karger, F.E., 1996. An episodic chlorophyll plume on the West Florida Shelf. Continental Shelf Research 16, 1201-1224.

Gordon, H.R., Morel, A., 1983. Remote Assessment of Ocean Color for Interpretation of Satellite Visible Imagery. Springer, New York, 114pp.

Gordon, H.R., Wang, M., 1994. Retrieval of water-leaving radiance and aerosol optical thickness over the oceans with SeaWiFS: a preliminary algorithm. Applied Optics 33, 443-452.

Gower, J.F.R, Lin, S., Borstad, G.A., 1984. The information content optical spectral ranges for remote chlorophyll estimation in coastal waters. International Journal of Remote Sensing 5(2), 349-364.

Gower, J.F.R., Doerffer, R., Borstad, G.A., 1999. Interpretation of the 685nm peak in water-leaving radiance spectra in terms of fluorescence, adsorption and scattering, and its observation by MERIS. International Journal of Remote Sensing 20, 1771-1786.

Gross, L., Thiria, S., Frouin, R., Mitchell, B.G., 2000. Artificial neural network for modeling the transfer function between marine reflectance and phytoplankton pigment concentration. Journal of Geophysical Research 105(C2), 3483-3495.

Gundersen, J.S., Gardner, W.D., Richardson, M.J., Walsh, I.D., 1998. Effects of monsoons on the seasonal and spatial distribution of POC and chlorophyll in the Arabian Sea. Deep-Sea Research II 45, 2103-2132.

Gundersen, K., Orcutt, K.M., Purdie, D.A., Michaels, A.F., Knap, A.H., 2001. Particulate organic carbon mass distribution at the Bermuda Atlantic Time-series Study (BATS) site. Deep-Sea Research II 48, 1697-1718.

Hamilton, P., Fargion, G.S., Biggs, D.C., 1999. Loop Current eddy paths in the western Gulf of Mexico. Journal of Physical Oceanography 29, 1180-1207.

Hamilton, P., Berger, T.J., Johnson, W., 2002. On the structure and motions of cyclones in the northern Gulf of Mexico. Journal of Geophysical Research-Oceans 107, 3208-3226.

Han, L., Rundquist, D.C., 1994. Comparison of NIR/RED ration and first derivative of reflectance in estimating algal-chlorophyll concentration: a case study in a turbid reservoir. Remote Sensing of Environment 62, 253-261.

Hofmann, E.E., Worley, S.J., 1986. An investigation of the circulation of the Gulf of Mexico. Journal of Geophysical Research-Oceans 91, 14221-14236.

Hoge, F.E., Wright, C.W., Lyon, P.E., Swift, R.N., Yungel, J.K., 1999. Satellite retrieval of inherent optical properties by inversion of an oceanic radiance model: a preliminary algorithm. Applied Optics 38(3), 495-504.

Hu, C., Carder, K.L., Muller-Karger, F.E., 2000. Atmospheric correction of SeaWiFS imagery over turbid coastal waters: a practical method. Remote Sensing of Environment 74, 195-206.

Hu, C., 2002. Satellite image track "Black Water" event off Florida coast. EOS 83, 281 & 285.

IOCCG, 1999. Status and Plans for Satellite Ocean-Colour Missions: Considerations for Complementary Missions. IOCCG, Dartmouth, Nova Scotia, Canada, 43pp.

IOCCG, 2000. Remote Sensing of Ocean Colour in Coastal, and Other Optically-Complex, Waters. IOCCG, Dartmouth, Nova Scotia, Canada, 140pp.

Kantha, L.H., Clayson, C.A., 2000. Numerical Models of Ocean and Oceanic Processes. Academic Press, New York, 940pp.

Keiner, L.E., Yan, X.H., 1998. A neural network model for estimating sea surface chlorophyll and sediments from thematic mapper imagery. Remote Sensing of Environment 66, 153-165.

Keiner, L.E., Brown, C.W., 1999. Estimating oceanic chlorophyll concentrations with neural network. International Journal of Remote Sensing 20(1), 189-194.

Kennicutt, M.C.II, Schroeder, W.W., Brooks, J.M., 1995. Temporal and spatial variations in sediment characteristics on the Mississippi-Alabama continental shelf. Continental Shelf Research 15, 1-18.

Kishino, M., Tanaka, A., Oishi, T., Doerffer, R., Schiller, H., 2000. Temporal and spatial variability of chlorophyll a, suspended solids and yellow substance in the Yellow Sea and East China Sea using ocean color sensor. Hyperspectral Remote Sensing of the Ocean 4154, 179-187.

Kitchen, J.C., Zaneveld, J.R.V., Pak, H., 1982. Effect of particle size distribution and chlorophyll content on beam attenuation spectra. Applied Optics 21, 3913-3918.

Krawczyk, H., Neumann, A., Hetscher, M., 1999. Mathematical and physical background of principal component inversion. Proceedings of Third International Workshop on MOS-IRS and Ocean Colour, 83-92.

Latif, M., Barnett, T.P., 1994. Causes of decadal climate variability over the North Pacific and North America. Science 206, 643-637.

Lee, M.A., Yeah, C.D., Cheng, C.H., Chan, J.W., Lee, K.T., 2003. Empirical orthogonal function analysis of AVHRR sea surface temperature patterns in Taiwan Strait. Journal of Marine Science and Technology 11(1), 1-7.

Lee, Z.P., Carder, K.L., Peacock, T.G., Davis, C.O., Mueller, J.L., 1996. Method to derive ocean absorption coefficients from remote-sensing reflectance. Applied Optics 35, 453-462

Lee, Z.P., Carder, K.L., Mobley, C.D., Steward, R.G., Patch, J. S., 1999. Hyperspectral remote sensing for shallow waters: 2. deriving bottom depths and water properties by optimization. Applied Optics 38, 3831-3843.

Lee, Z.P., Carder, K.L., 2002. Effect of spectral band numbers on the retrieval of water column and bottom properties from ocean color data. Applied Optics 41(12), 2191-2201.

Lee, Z.P., Carder, K.L., Arnone, R.A., 2002. Deriving inherent optical properties from water color: a multiband quasi-analytical algorithm for optically deep water. Applied Optics 41(27), 5755-5772.

Lodhi, M.A., Rundquist, D.C., Han, L., Juzila, M.S., 1997. The potential for remote sensing of loess soils suspended in surface waters. Journal of the American Water Resources Association 33(1), 111-127.

Lohrenz, S.E., Dagg, M.J., Whitledge, T.E., 1990. Enhanced primary production at the plume-oceanic interface of the Mississippi River. Continental Shelf Research 10, 639-664.

Loisel, H., Morel, A., 1998. Light scattering and chlorophyll concentration in case 1 water: a reexamination. Limnology and Oceanography 43, 847-858.

Loisel, H., Boss, E., Stramski, D., Oubelkheir, K., Deschamps, P.-Y., 2001. Seasonal variability of the backscattering coefficient in the Mediterranean Sea based on Satellite SeaWiFS imagery. Geophysical Research Letters 28, 4203-4206.

Maritorena, S., Siegel, D.A., Peterson, A.R., 2002. Optimization of a semianalytical ocean color model for global-scale application. Applied Optics 41(15), 2705-2714.

McClain, C.R., Evans, R.H., Darzi, M., 1995. SeaWiFS Quality Control Masks and Flags: Initial Algorithms and Implementation Strategy. NASA Technical Memorandum 104566, Greenbelt, Maryland, 45pp

Merrell, R.L., Morrison, J.M., 1981. The current regime of the western Gulf of Mexico as observed in April 1978. Journal of Geophysical Research 86, 4181-4185.

Miller, A.J., Cayan, D.R., Barnett, T.P., Graham, N.E., Oberhuber, J.M., 1994. Interdecadal variability of the Pacific Ocean: model response to observed heat flux and wind stress anomalies. Climate Dynamics 9, 287-302.

Mishonov, A.V., Gardner, W.D., Richardson, M.J., 2000. Prospects for using historical transmissometer data in large-scale assessment of POC. EOS 80(49), 122.

Mishonov, A.V., Gardner, W.D., Richardson, M.J., 2003. Remote sensing and surface POC concentration in the South Atlantic. Deep-Sea Research II 50, 2997-3015.

Mitchum, G.T., Sturges, W., 1982. Wind-driven currents on the West Florida Shelf. Journal of Physical Oceanography 12, 1310-1317.

Molinari, R.L., Mayer, D.A., 1982. Current meter observations on the continental slope at two sites in the eastern Gulf of Mexico. Journal of Physical Oceanography 12, 1480-1492.

Morel, A., Prieur, L., 1977. Analysis of variations in ocean color. Limnology and Oceanography 22, 709-722.

Morel, A., Ahn, Y.-H., 1991. Optics of heterotrophic nano-flagellates and ciliates: a tentative assessment of their scattering role in oceanic waters compared to those of bacterial and algal cells. Journal of Marine Research 48, 1-26.

Morey, S.L., Martin, P.J., O'Brien, J.J., Wallcraft, A.A., Zavala-Hidalgo, J., 2003. Export pathways for river discharged fresh water in the northern Gulf of Mexico. Journal of Geophysical Research 108(C10), 3303 (doi:10.1029/20002JC001674).

Morrison, J., Gaurin, S., Codispoti, L.A., Takahashi, T., Millero, F.J., Gardner, W.D., Richardson, M.J., 2001. Seasonal evolution of the hydrographic properties during the Antarctic Circumpolar current at 170°W during 1997-1998. Deep-Sea Research II 48, 3943-3972.

Mueller, J.L., 1976. Ocean color spectra measured off the Oregon coast: characteristic vectors. Applied Optics 15(2), 394-402.

Neumann A., Krawczyk, H., Walzel, T., 1995. A complex approach to quantitative interpretation of spectral high resolution imagery. Proceedings of the Third Thematic Conference on Remote Sensing for Marine and Coastal Environments, II-641 & II-652.

Oey, L.-Y., 1995. Eddy and wind-forced shelf circulation. Journal of Geophysical Research – Oceans 100, 8621-8637.

Ohlmann, J.C., Niiler, P.P., 2005. Circulation over the continental shelf in the northern Gulf of Mexico. Progress in Oceanography 64, 45-81.

O'Reilly, J.E., Maritorena S., Mitchell, G., Siegel, M.A., Carder, K.L., Garver, S.A., Kahru, M., McClain, C.R., 1998. Ocean color chlorophyll algorithms for SeaWiFS Journal of Geophysical Research 103(11), 24937-24953.

Osvaldo, U., Sathyendranath, S., Platt, T., 1994. Effect of the particle-size distribution on the backscattering ratio in seawater. Applied Optics 33(30), 7070-7077.

Paden, C.A., Abbott, M.R., and Winant, C.D., 1991. Tidal and atmospheric forcing of the upper ocean in the Gulf of California, 1: sea surface temperature variability. Journal of Geophysical Research-Ocean 96(C10), 18337-18359.

Peng, S., Fyfe, J., 1996. The coupled patterns between sea level pressure and sea surface temperature in the midlatitude North Atlantic. Journal of Climate 9, 1824-1839.

Preisendorfer, R.W., 1988. Principal Component Analysis in Meteorology and Oceanography. Elsevier, Amsterdam, 452pp.

Prospero, J.M., 1996. The atmospheric transport of particles to the ocean. In: Particle Flux to the Ocean. John Wiley & Sons, Ltd., Chichester, New York, p. 19-52.

Rabalais, N.N., Turner, R.E., Justic, D., Dortch, Q., Wiseman, W.J., Sen Gupta, B.K., 1996. Nutrient Changes in the Mississippi River and system responses on the adjacent continental shelf. Estuaries 19, 386-407.

Redalje, D.G., Lohrenz, S.E., Fahnenstiel, G.L., 1994. The relationship between primary production and the vertical export of particulate organic carbon matter in a river-impacted coastal system. Estuaries 17, 829-838.

Rhodes, R.C., Wallcraft, A.J., Thompson, J.D., 1985. Navy-corrected Geostrophic Wind Set for the Gulf of Mexico. NORDA Technical Note Vol. 310, 103pp.

Richardson, M.J., Gardner, W., Mishonov, A.V., Son, Y.B., 2003. Particle organic carbon in the North-east Gulf of Mexico: developing algorithm between bio-optical data and satellite ocean color products. Oceanography 16(2), 57.

Robinson, I.S., 2004. Measuring the Oceans from Space: The Principles and Methods of Satellite Oceanography. Springer, New York, 669pp.

Roesler, C.S., Perry, M.J., 1995. *In situ* phytoplankton absorption, fluorescence emission, and particulate backscattering spectra determined from reflectance. Journal of Geophysical Research 100, 13279-13294.

Roesler, C.S., Boss, E., 2003. Spectral beam attenuation coefficient retrieved from ocean color inversion. Geophysical Research Letters 30(9), (10.1029/2002GL016185).

Romanou, A., Chassignet, E.P., 2004. Gulf of Mexico circulation within a high-resolution numerical simulation of the North Atlantic Ocean. Journal of Geophysical Research-Oceans 109, 1003-1028.

Sahl, L.E., Wiesenburg, D.A., Merrell, W.J., 1997. Interactions of mesoscale features with Texas shelf and slope waters. Continental Shelf Research 17, 117-136.

Sathyendranath, S., Prieur, L., Morel, A., 1989. A three-component model of ocean colour and its application to remote sensing of phytoplankton pigments in coastal water. International Journal of Remote Sensing 10(8), 1373-1394.

Sathyendranath, S., Hoge, F.E., Platt, T., Swift, R.N., 1994. Detection of phytoplankton pigments from ocean colour: improved algorithms. Applied Optics 33, 1081-1089.

Schiller, H., Doerffer, R., 1999. Neural network for emulation of an inverse model-operational derivation of case II water properties from MERIS data. International Journal of Remote Sensing 20(9), 1735-1746.

Schroeder, W.W., Dinnel, S.P., Wiseman, Jr.W.J., Merrell, Jr.W.J., 1987. Circulation pattern inferred from the movement of detached buoys in the eastern Gulf of Mexico. Continental Shelf Research 7, 883-894.

Shen, C., Liew, S.C., Kwoh, L.K., 2001. SeaWiFs observation of chlorophyll distribution in regional seas. In: The 22nd Asian Conference on Remote Sensing, Singapore, 5-9 November 2001.

Smith, D.C.IV, 1986. A numerical study of Loop Current eddy interaction with topography in the western Gulf of Mexico. Journal of Oceanography 30, 1814-1819.

Son, Y.B., Richardson, M.J., Gardner, W.D., Mishonov, A.V., 2004. Measuring particulate organic carbon in surface water of the Gulf of Mexico from space. In: Poster Presentation at the Next Steps in the Gulf of Mexico, July 2004, College Station, TX.

Son, Y.B., 2005. Particulate Organic Caron (POC) Algorithms based on spectral remote sensing data and its temporal and spatial variability in the Gulf of Mexico. In: Poster Presentation at the Research Student Week, March 2005, College Station, TX.

Stramska, M., Stramski, D., Hapter, R., Kaczmarek, S., Ston, J., 2003. Bio-optical relationship and ocean color algorithms for the north polar region of the Atlantic. Journal of Geophysical Research-Ocean 108 (C5), 3143.

Stramski, D., Kiefer, D., 1991. Light scattering by microorganisms in the open ocean. Progress in Oceanography 28, 343-383.

Stramski, D., Reynolds, R.A., Kahru, M., Mitchell, B.G., 1999. Estimation of particulate organic carbon in the ocean from satellite remote sensing. Science 285, 239-242.

Strub, P. T., James, C., 2000. Altimeter-derived variability of surface velocity in the California current system. 2. seasonal circulation and eddy statistics. Deep-Sea Research II 47, 831-870.

Sturges, W., Leben, R., 2000. Frequency of ring separation from the Loop Current in the Gulf of Mexico. Journal of Physical Oceanography 30, 1814-1819.

Tanaka, A., Kishino, M., Oishi, T., Doerffer, R., Schiller, H., 2000. Application of neural network method to case II water. Proceedings of Remote Sensing of the Ocean and Sea Ice 2000 4172, 144-152.

Thomas, A.C., Townsend, D.W., Weatherbee, R., 2003. Satellite-measured phytoplankton variability in the Gulf of Maine. Continental Shelf Research 23, 971-989.

Thurman, H.V., Trujillo, A.P., 2002. Essentials of Oceanography. Prentice Hall, New Jersey, 524pp.

Twomey, S., 1977. Introduction to the Mathematics of Inversion in Remote Sensing and Indirect Measurements. Elsevier Scientific Publishing Company, New York, 243pp.

Ulloha, O., Sathyendranath, S., Platt, T., 1994. Effect of the particle-size distribution on the backscattering ratio in seawater. Applied Optics 33, 7070-7077.

Unal, Y.S., Ghil, M., 1995. Interannual and interdecadal oscillation patterns in sea level. Climate Dynamics 11, 255-278.

von Storch, H., Zwiers, F., 1999. Statistical Analysis in Climate Research. Cambridge University Press, Cambridge, 484pp.

Vastano, A.C., Barron Jr., C.N., Shear, E.W., 1995. Satellite observations of the Texas current. Continental Shelf Research 15, 729-754.

Venegas, S.A., Mysak, L.A., Straub, D.N., 1997. Atmosphere-ocean coupled variability in the South Atlantic. Journal of Climatology 10(11), 2904-2920.

Vukovich, F.M., Maul, G.A., 1985. Cyclonic Eddies in the eastern Gulf of Mexico. Journal of Physical Oceanography 15, 105-117.

Vukovich, F.M., 1995. An updated evaluation of the Loop Current's eddy-shedding frequency. Journal of Geophysical Research – Oceans 91, 2645-2660.

Walker, N.D., Rouse, L.J., Rouge, B., Fargion, G.S., Biggs, D.C., 1994. The great flood of summer 1993: Mississippi River discharge studied. EOS 75, 409-415.

Walker, N.D., 1996. Satellite assessment of Mississippi River plume variability: causes and predictability. Remote Sensing of Environment 58, 21-35.

Wallace, J.M., Smith, C., Bretherton, C.S., 1992. Singular value decomposition of wintertime sea surface temperature and 500-mb height anomalies. Journal of Climatology 5, 561-576.

Walsh, I.D., Chung, S.P., Richardson, M.J., Gardner, W.D., 1995. The diel cycle in the integrated particle load in the equatorial Pacific: a comparison with primary production. Deep-Sea Research II 42, 465-477.

Wang, W., Nowlin, W.D., Reid, R.O., 1998. Analyzed surface meteorological fields over northwestern Gulf of Mexico for 1992-94: mean, seasonal, and monthly patterns. Monthly Weather Review 126, 2864-2883.

Winant, C.D., Beardsley, R.C., Davis, R.E., 1987. Moored wind, temperature, and current observations made during Coastal Ocean Dynamics Experiment 1 and 2 over the northern California continental shelf and upper slope. Journal of Geophysical Research – Oceans 92, 1569-1604.

Wolter, K., Timlin, M.S., 1998. Measuring the strength of ENSO - how does 1997/98 rank? Weather 53, 315-324.

Wood, M.M., 1993. Particulate matter in the South Atlantic Ocean. M.S. thesis, Texas A&M University, College Station.

Yang, H., Weisberg, R.H., 1999. Response of the west Florida shelf circulation to climatological wind stress forcing. Journal of Geophysical Research 104(C3), 5301-5320.

Yoder, J.A., Schollaert, S.E., O'Reilly, J.E., 2002. Climatological phytoplankton chlorophyll and sea surface temperature patterns in continental shelf and slope waters off the northeast U.S. coast. Limnology and Oceanography 47(3), 672-682.

VITA

Young Baek Son was born in Pusan, Korea on November 29, 1970. He earned his B.S. degree in earth sciences from Pusan National University in Pusan, Korea in February 1993. He received his M.S. degree from the Department of Oceanography at Pusan National University in February of 1997. He served in the military as a Navy intelligence officer at Jin-Hae from August 1997 to July 2000. He worked for Korea Ocean Research and Development Institute (KORDI) as a research scientist in 1996 and from 2000 to 2001. He received his Ph.D. degree from the Department of Oceanography at Texas A&M University in May 2006.

Young Baek and his wife, Yoon Hyang Kang, and two sons, SeokHan and ShangHwan, live in Maryland, where Young Baek will works at NOAA. He may be reached via email at *sonyb@ocean.tamu.edu* or U.S. mail c/o Department of Oceanography, Texas A&M University, 77843-3146.